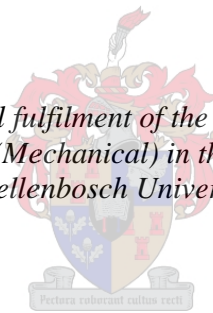


# **Development of an Open Volumetric Air Receiver for a Rock Bed Thermal Energy Storage System**

by

Jacobus Coenraad Nel

*Thesis presented in partial fulfilment of the requirements for the degree  
of Master of Engineering (Mechanical) in the Faculty of Engineering at  
Stellenbosch University*



Supervisor: Prof Frank Dinter  
Co-supervisor: Prof Theodor W. von Backström

December 2017

# Declaration

By submitting this thesis electronically, I declare that the entirety of the work contained therein is my own, original work, that I am the sole author thereof (save to the extent explicitly otherwise stated), that reproduction and publication thereof by Stellenbosch University will not infringe any third party rights and that I have not previously in its entirety or in part submitted it for obtaining any qualification.

Date: December 2017

Copyright © 2017 Stellenbosch University  
All rights reserved

# Abstract

## Development of an Open Volumetric Air Receiver for a Rock Bed Thermal Energy Storage System

JC Nel

*Department of Mechanical and Mechatronic Engineering,  
Stellenbosch University,  
Private Bag XI, Matieland 7602, South Africa*

Thesis: MEng (Mech)  
December 2017

Concentrating solar power technology combined with a thermal energy storage system offers a sustainable and dispatchable energy technology which can produce electricity on demand. However, the high costs and advanced technology requirements associated with these systems need to be addressed in order to make them more cost effective and viable for local implementation. In this study an open volumetric air receiver was developed as a suitable solution to overcome the mentioned limitations. This technology has an inherently simple design with the benefit of using air as HTF that is abundantly available and has no environmental impact.

The ultimate goal of this work is to use the open volumetric air receiver to charge a rock bed thermal energy storage system. In this project the first steps were taken through developing an absorber concept for this use. The concept was aimed towards a simple and cost effective design, which satisfies local manufacturing capabilities and material availability. The charging requirements for the rock bed allowed for the use of a metallic absorber, since the maximum charging air temperature is 600 °C. A stack of stainless steel wire mesh screens with a gradually decreasing porosity through its depth was identified as a cost-effective and simple absorber concept. The stack of wire mesh screens was placed inside a modular stainless steel cup to form a scalable absorber module.

A numerical model was developed to investigate the heat and radiation transfer inside the porous absorber. The model assumed local thermal non-equilibrium

between the screen and the air temperatures and approximated the radiation as a volumetric heat source. The use of low porosity wire mesh screens in the front of the absorber, followed by a finer screen deeper in its volume reduced the thermal losses and allowed better penetration of the incident flux, as well as enhanced the heat transfer through the absorber. The air mass flow rate proved to have a significant influence on the outlet air temperature. A lower flow rate increased the outlet air temperature, but also caused an increase in thermal loss due to the higher front temperature and lower heat transfer coefficient, and hence lowered the thermal efficiency of the absorber.

The absorber prototype and a small scale central receiver test tower was designed, manufactured and installed on an available  $1 \text{ kW}_{\text{th}}$  medium flux concentrator to experimentally test and validate the concept. Different configurations of mesh screens were tested at different air mass flow rates. The best mesh configuration produced hot outlet air at  $405 \text{ }^{\circ}\text{C}$  to  $488 \text{ }^{\circ}\text{C}$  at thermal efficiencies of  $87 \%$  to  $58 \%$  in an average incident flux level of  $55.3 \text{ kW/m}^2$ . The results produced by the model were in very good agreement with the experimental results at higher flow rates and adequately predicted its trend. At lower flow rates, however, the model overestimated the thermal performance. Finally this project proved that the wire mesh screen absorber concept with a gradually decreasing porosity is a suitable solution for the use in an open volumetric air receiver to charge a rock bed thermal energy storage system.

# Uittreksel

## Ontwikkeling van 'n Oop Volumetriese Lugontvanger vir 'n Rotsbed Termiese Energie Stoorstelsel

JC Nel

*Departement Meganiese en Megatroniese Ingenieurswese,  
Universiteit van Stellenbosch,  
Privaatsak XI, Matieland 7602, Suid Afrika*

Tesis: MEng (Meg)  
Desember 2017

Gekonsentreerde sonkragtegnologie gekombineer met 'n termiese-energie stoorstelsel bied 'n volhoubare en versendbare energietegnologie wat elektrisiteit op aanvraag kan lewer. Die hoë koste en gevorderde tegnologie-vereistes wat met hierdie stelsels verband hou, moet egter aangespreek word om hul meer koste-effektief en lewensvatbaar te maak vir plaaslike implementering. In hierdie studie was 'n oop volumetriese lugontvanger ontwikkel as 'n geskikte oplossing om die genoemde beperkings te oorkom. Hierdie tegnologie het 'n inherente eenvoudige ontwerp, met die voordeel om lug te gebruik as hitte-oordragvloeistof wat oorvloedig beskikbaar is en geen omgewingsimpak het nie.

Die uiteindelijke doelwit van hierdie werk is om die oop volumetriese lugontvanger te gebruik om 'n rotsbed termiese energie stoorstelsel te laai. In hierdie projek was die eerste stappe geneem om 'n konsep vir 'n absorbeerder te ontwikkel vir hierdie gebruik. Die konsep was gemik op 'n eenvoudige en koste-effektiewe ontwerp wat voldoen aan plaaslike vervaardigingsvermoëns en materiaal beskikbaarheid. Die laaivereistes vir die rotsbed laat die gebruik van 'n metaalabsorbeerder toe, aangesien die maksimum lugtemperatuur 600 °C is. 'n Stapel vlekvrystaal gaas skerms met 'n geleidelik dalende porositeit deur die diepte was geïdentifiseer as 'n koste-effektiewe en eenvoudige absorbeerder konsep, en is geplaas in 'n modulêre vlekvrystaal koppie wat 'n skaalbare absorbeerder module vorm.

'n Numeriese model was ontwikkel om die hitte en bestraling oordrag binne die poreuse absorbeerder te ondersoek. Die model het lokale termiese nie-ewewig

tussen die skerm en die lugtemperatuur aangeneem en die straling benader as 'n volumetriese hittebron. Die gebruik van lae porositeit gaas skerms in die voorkant van die absorbeerder, gevolg deur 'n fyner skerm dieper in die volume verminder die termiese verliese en laat beter penetrasie van die gekonsentreerde straling toe, sowel as die hitteoordrag deur die absorbeerder. Die lugmassa se snelheid het 'n beduidende invloed op die uitlaatlugtemperatuur. 'n Laer vloeitempo het die uitlaatlugtemperatuur verhoog, maar het ook 'n toename in termiese verlies as gevolg van die hoër voortemperatuur asook verswakte hitte oordrag koëffisiënt veroorsaak, en sodoende die termiese doeltreffendheid van die absorbeerder verlaag.

Die prototipe van die absorbeerder, en 'n kleinskaalse sentrale ontvanger toetstoring, was ontwerp, vervaardig en geïnstalleer op 'n beskikbare 1 kW konsentrator om die konsep eksperimenteel te toets en te valideer. Verskillende konfigurasies van maasskerms is by verskillende vloeitempo's getoets. Die beste gaas konfigurasie het warm uitlaat lug by 405 °C tot 488 °C met 'n termiese doeltreffendheid van 87 % tot 58 % gelewer, met 'n gemiddelde voorvalvloeivlak van 55.3 kW/m<sup>2</sup>. Die resultate wat deur die model geproduseer is, was in baie goeie ooreenstemming met die eksperimentele resultate by hoër vloeitempo's en het die tendens voldoende voorspel. Dit het egter die termiese doeltreffendheid oorskat by laer vloeitempo's. Uiteindelik het hierdie projek bewys dat die draad gaas skerms absorbeerder konsep met 'n geleidelik dalende porositeit 'n geskikte oplossing is vir die gebruik in 'n oop volumetriese lugontvanger om 'n rotsbed termiese energie stoorstelsel te laai.

# Acknowledgements

I would like to express my genuine appreciation to the people and organizations that helped me to successfully complete this project. Without their contribution, moral support, and financial aid it would not have been possible.

- Prof Frank Dinter and Prof Theo von Backström for their exceptional guidance and input throughout the project. It was a real privilege to work with such passionate and experienced mentors.
- STERG and all of its members who made the past two years an unforgettable experience. This project and document would not have been of the standard it is without their input and help.
- My family for understanding and for their continuous support and motivation. Vasbyt, aanhou, bybly, Boesmanland. Also a special thank you to Ruzaan Marais for her invaluable role in supporting me.
- The workshop of the Mechanical Engineering Department for the excellent and professional work they did in manufacturing the components.
- CRSES for the financial aid which made it possible for me to do my masters.

# Table of Contents

Declaration.....	i
Abstract.....	ii
Uittreksel.....	iv
Acknowledgements.....	vi
Table of Contents.....	vii
List of Figures.....	xii
List of Tables.....	xv
Nomenclature.....	xvii
1. Introduction.....	1
1.1. Background to Research Problem.....	1
1.1.1. Concentrating Solar Power Technology.....	1
1.1.2. Central Receiver Systems.....	3
1.1.3. Thermal Energy Storage.....	5
1.2. Research Problem Statement.....	5
1.3. Research Objectives.....	6
1.4. Methodology and Scope.....	7
1.5. Brief Chapter Overview.....	9
2. Literature Review.....	10
2.1. Introduction.....	10
2.2. Open Volumetric Air Receiver Technology.....	11
2.2.1. Working Principle.....	11
2.2.2. Air as Heat Transfer Fluid.....	12
2.2.3. Absorber Material.....	13



2.2.4.	Design Considerations and Challenges.....	16
2.3.	Reference Open Volumetric Receiver Projects.....	17
2.3.1.	Phoebus-TSA.....	18
2.3.2.	HiTRec.....	18
2.4.	Rock Bed Thermal Energy Storage System.....	19
2.5.	Conclusion.....	20
3.	Absorber Concept.....	21
3.1.	Introduction.....	21
3.2.	Receiver Requirements.....	21
3.3.	Design Objectives.....	22
3.4.	Synthesis of Solutions.....	23
3.5.	Gradual Porosity Wire Mesh Absorber.....	25
3.5.1.	Concept Layout.....	25
3.5.2.	Wire Mesh Screen Absorber.....	25
3.5.3.	Modular Absorber Cup.....	27
3.6.	Wire Mesh Geometrical Properties.....	28
3.7.	Conclusion.....	30
4.	Numerical Heat Transfer Model.....	31
4.1.	Introduction.....	31
4.2.	Literature Review.....	31
4.3.	Thermal Model.....	34
4.3.1.	Governing Equations.....	34
4.3.2.	Volumetric Heat Transfer Coefficient.....	35
4.3.3.	Property Models.....	36
4.4.	Radiative Model.....	36
4.4.1.	Governing Equation.....	37
4.4.2.	Incident Flux.....	37
4.4.3.	Radiative Properties.....	38
4.5.	Boundary Conditions.....	39

4.5.1. Front Boundary .....	39
4.5.2. Back Boundary .....	40
4.6. Absorber Performance .....	40
4.7. Numerical Procedure.....	40
4.8. Modeling Results and Discussion .....	43
4.8.1. Incident Flux Distribution.....	43
4.8.2. Steady State Performance .....	44
4.9. Conclusion.....	47
5. Experimental Apparatus and Procedure .....	48
5.1. Introduction.....	48
5.2. Test Setup.....	49
5.2.1. Small Scale Test Tower .....	49
5.2.2. Medium Flux Concentrator.....	51
5.3. Thermal Evaluation.....	52
5.3.1. Temperature .....	52
5.3.2. Air Mass Flow Rate .....	53
5.3.3. Incident Flux .....	54
5.3.4. Weather .....	54
5.4. Experimental Procedure .....	54
5.4.1. Variables .....	54
5.4.2. Quasi-steady State.....	55
5.4.3. Operating Procedure .....	56
5.5. Calibration and Uncertainty .....	56
5.6. Conclusion.....	59
6. Results and Discussion .....	60
6.1. Introduction.....	60
6.2. Experimental Results .....	60
6.2.1. Temperature and Flow Rate Measurements .....	60
6.2.2. Thermal Performance .....	63

6.2.3. Combined Results .....	65
6.3. Model Validation and Comparison .....	68
6.4. Observations during Testing .....	70
6.4.1. Wire Screen Oxidization .....	71
6.4.2. Absorber Conductivity .....	71
6.4.3. Environmental Influences .....	72
6.5. Conclusion .....	73
7. Conclusion .....	74
7.1. Discussion of Results .....	74
7.2. Future Work and Recommendations .....	76
7.3. Conclusion .....	77
Appendices .....	79
A. Thermophysical Properties of Air .....	80
A.1. Air Property Figures .....	80
B. Incident Flux Calculation .....	82
B.1. Introduction .....	82
B.2. Methodology .....	82
B.3. Equipment .....	83
B.3.1. Flux Sensors .....	83
B.3.2. Thermal Camera .....	84
B.4. Peak Concentration Ratio .....	84
B.5. Variance .....	88
B.6. Overall Setup Performance .....	89
B.7. Validation .....	90
C. Test Tower .....	91
C.1. Thermocouple Layout .....	91
C.2. Tower Assembly Drawing .....	92
D. Flow Meter Calibration .....	93
D.1. Introduction .....	93

D.2. Equipment .....	93
D.2.1. Venturi Flow Meter .....	93
D.2.2. Pressure Transducer .....	94
D.3. Venturi Calibration.....	95
E. Sample Calculations .....	98
E.1. Sample Calculations.....	98
List of References .....	102

# List of Figures

Figure 1.1: Two most dominant CSP technologies .....	2
Figure 1.2: Direct normal irradiation for South Africa.....	3
Figure 2.1: Flow diagram of a typical OVAR CRS plant.....	10
Figure 2.2: Heat transfer principle in tubular and volumetric receivers.....	12
Figure 2.3: Ceramic (SiSiC) absorber module and close-up .....	14
Figure 2.4: Metallic absorbers .....	15
Figure 2.5: Optimized metallic absorbers.....	16
Figure 2.6: Hexagonal cups filled with knit wire in the Phoebus-TSA receiver ...	18
Figure 2.7: HiTRec concept.....	19
Figure 2.8: Rock bed TES test facility.....	19
Figure 2.9: Qualitative temperature distribution in the rock bed TES.....	20
Figure 3.1: Example of a wire mesh screen in (a) and knit wire in (b) .....	23
Figure 3.2: Annotated cross-sectional view showing the layout and air flow of the absorber concept .....	25
Figure 3.3: Single sheet of each different wire mesh screen used.....	26
Figure 3.4: Mesh configuration mounted on perforated back plate as absorber....	27
Figure 3.5: Modular cup design without (a) and with (b) the wire mesh absorber installed.....	28
Figure 4.1: Schematic diagram of the absorber .....	33
Figure 4.2: Discretized absorber model with annotations .....	41
Figure 4.3: Flowchart for the calculation procedure of the numerical model .....	42
Figure 4.4: Flux distribution over the absorber aperture .....	43
Figure 4.5: Temperature distribution of the solid and the fluid through the absorber at two different flow rates .....	44

Figure 4.6: Model performance plot for the (5/5/5) absorber at four different AMFs .....	45
Figure 4.7: Efficiency and thermal losses from the front of the absorber plotted against the outlet air temperature from the numerical model .....	46
Figure 5.1: Small scale test tower .....	49
Figure 5.2: Receiver housing .....	50
Figure 5.3: Sample of the rocks used in the rock bed heat exchanger .....	51
Figure 5.4. Medium flux concentrator with the tower installed for testing .....	51
Figure 5.5: Thermocouple layout in and around the absorber and cup .....	52
Figure 5.6: DNI and ambient air temperature variation over a test period .....	59
Figure 6.1: Temperature measurements for the (6/4/2) absorber at five different AMFs .....	61
Figure 6.2: Temperature distribution through the (6/4/2) absorber and outlet air temperature at four different AMFs .....	62
Figure 6.3: Experimental performance plot for the (6/4/2) absorber at four different AMFs .....	64
Figure 6.4: Thermal image of the absorber and Gaussian flux distribution .....	65
Figure 6.5: Combined experimental performance plot of different absorber configurations tested at different AMFs .....	65
Figure 6.6: Experimental measured efficiency and outlet temperature at different AMFs for the different absorber configurations .....	67
Figure 6.7: Comparison of the performance of the (6/4/2) absorber between the numerical model results and experimental measurements .....	68
Figure 6.8: Performance of the experimental and model results with the wire mesh screen absorber tested at PSA .....	70
Figure 6.9: Samples of new screens compared to oxidized screens .....	71
Figure 6.10: New absorber showing clear burn mark at focal spot .....	71
Figure 6.11: Experimental temperature plot of the (6/10/10) absorber showing the effect of a dip in DNI due to a small cloud passing over .....	72
Figure A.1: Specific heat capacity of air over a temperature range .....	80
Figure A.2: Density of air over a temperature range .....	81
Figure A.3: Thermal conductivity of air over a temperature range .....	81

Figure A.4: Dynamic viscosity of air over a temperature range.....	81
Figure B.1: Solar field layout of the medium flux concentrator showing the two sides as well as aiming mirror and tower locations .....	84
Figure B.2: Partly covered solar field during flux measurement of the LHS of the field.....	85
Figure B.3: Measured peak flux on the absorber as more columns of mirrors are opened.....	85
Figure B.4: Peak concentration ratio against the number of mirrors open on the RHS.....	87
Figure B.5: Peak concentration ratio against the number of mirrors open on the LHS.....	87
Figure B.6: Image from the thermal camera showing the temperature distribution over the absorber aperture, with an inspection line added.....	88
Figure B.7: Temperature distribution over the absorber aperture at the inspection line, and calculated Gaussian distribution function .....	89
Figure C.1: Thermocouple locations throughout the test tower and absorber.....	91
Figure D.1: Manometer pressure drop against the pressure transducer voltage output .....	94
Figure D.2: Discharge coefficient for the venturi flow meter over the inlet Reynolds number .....	96

# List of Tables

Table 1.1: Various central receiver technology types.....	4
Table 2.1: Merits and demerits of non-pressurized air as HTF .....	13
Table 3.1: Rock bed TES charging conditions .....	22
Table 3.2: Concentrating capabilities of the medium flux concentrator.....	22
Table 3.3: Wire mesh screen properties tested at PSA .....	24
Table 3.4: Wire mesh geometrical properties for the absorber concept .....	30
Table 4.1: Reference parameters for simulation.....	43
Table 4.2: Different AMFs, mass fluxes and calculated Reynolds numbers for the simulation.....	44
Table 5.1: Controlled and uncontrolled variables of the experimental setup .....	54
Table 5.2: Different AMFs used for experimentally testing the absorber at .....	55
Table 5.3: Incident flux and power on the absorber at different DNI values .....	55
Table 6.1: Measured and calculated results for the (6/4/2) absorber at the quasi-steady state condition of each AMF .....	63
Table 6.2: Experimental performance summary and operating conditions of the different absorber configurations tested .....	66
Table B.1: Specifications for the Vatell TG1000-0 with AMP-15 flux sensor .....	83
Table B.2: Specifications for the Hukseflux SBG01-010 flux sensor .....	84
Table B.3: Specifications for the Fluke Ti400.....	84
Table B.4: Flux measurements and peak concentration ratios calculated for the RHS of the field .....	86
Table B.5: Comparison between the total incident power and average concentration ratio .....	90
Table D.1: Dimensions of the venturi flow meter .....	93



Table D.2: Specifications for the Endress+Hauser Deltabar PMD230 pressure transducer.....	94
Table D.3: Ambient conditions in which calibration took place .....	95
Table D.4: Measured and calculated data for the venturi calibration.....	96
Table E.1: Measured and calculated results for the (6/4/2) absorber at the quasi-steady state condition of the first AMF .....	98
Table E.2: Weather data for the first quasi-steady state condition of the (6/4/2) absorber.....	99

# Nomenclature

## Constants

$$R_{\text{air}} = 287.058 \text{ J}/(\text{kg}\cdot\text{K})$$

$$\sigma = 5.67 \times 10^{-8} \text{ W}/(\text{m}^2\cdot\text{K}^4)$$

## Variables

$A$	Area. . . . .	[ m <sup>2</sup> ]
$a$	Absorption coefficient. . . . .	[-]
$C$	Multiplication factor. . . . .	[-]
$c$	Concentration ratio. . . . .	[-]
$cf$	Compactness factor. . . . .	[-]
$c_p$	Specific heat capacity at constant pressure. . . . .	[ J/(kg·K) ]
$DNI$	Direct normal irradiance. . . . .	[ W/m <sup>2</sup> ]
$d$	Diameter. . . . .	[ m ]
$E$	Volumetric heat source. . . . .	[ W/m <sup>3</sup> ]
$H_{\text{ap}}$	Height (mesh aperture) . . . . .	[ m ]
$h$	Enthalpy. . . . .	[ kJ/kg ]
$h_v$	Volumetric heat transfer coefficient. . . . .	[ W/(m <sup>3</sup> ·K) ]
$I$	Concentrated solar flux. . . . .	[ W/m <sup>2</sup> ]
$i$	Node number. . . . .	[-]
$K$	Extinction coefficient. . . . .	[ m <sup>-1</sup> ]
$k$	Thermal conductivity. . . . .	[ W/(m·K) ]
$L$	Length. . . . .	[ m ]
$M$	Mesh number. . . . .	[ m <sup>-1</sup> ]

$\dot{M}$	Mass flux. . . . .	[ kg/(m <sup>2</sup> ·s) ]
$\dot{m}$	Mass flow rate. . . . .	[ kg/s ]
$Nr$	Number/amount. . . . .	[-]
$Nu$	Nusselt number. . . . .	[-]
$oar$	Open area ratio. . . . .	[-]
$\Delta p$	Differential pressure. . . . .	[ Pa ]
$PoA$	Power on Aperture. . . . .	[ W ]
$Pr$	Prantdl number. . . . .	[-]
$\dot{Q}_{out}$	Thermal power in outlet air. . . . .	[ W ]
$Re$	Reynolds number. . . . .	[-]
$T$	Temperature. . . . .	[ °C ]
$t$	Time. . . . .	[ s ]
$U$	Uncertainty. . . . .	[ % ]
$u$	Superficial velocity. . . . .	[ m/s ]
$\dot{V}$	Volumetric flow rate. . . . .	[ m <sup>3</sup> /s ]
$v$	Velocity. . . . .	[ m/s ]
$Z$	Absorber depth. . . . .	[ m ]
$\alpha_{sf}$	Specific surface area. . . . .	[ m <sup>-1</sup> ]
$\beta$	Venturi inlet to throat diameter ratio. . . . .	[-]
$\sigma_s$	Scattering coefficient. . . . .	[-]
$x, y, z$	Coordinates. . . . .	[ m ]
$\alpha$	Absorptivity. . . . .	[-]
$\varepsilon$	Emissivity. . . . .	[-]
$\eta$	Efficiency. . . . .	[-]
$\mu$	Dynamic viscosity. . . . .	[ kg/(m·s) ]
$\nu$	Kinematic viscosity. . . . .	[ m <sup>2</sup> /s ]
$\rho$	Density. . . . .	[ kg/m <sup>3</sup> ]
$\sigma$	Variance. . . . .	[ m <sup>-1</sup> ]
$\varphi$	Volumetric porosity. . . . .	[-]

**Subscripts**

o	initial/front/incident
a	aperture
abs	absorber
atm	atmosphere
avg	average
conv	convection
cond	conduction
e	effective
f	fluid
h	hydraulic
i	node number
in	inlet condition
l	local
max	maximum
mirr	mirrors
n	system boundary
out	outlet condition
peak	peak condition
rad	radiation
refl	reflection
s	solid
th	thermal
thr	throat
v	volumetric
$\dot{\quad}$ (dot)	quantity per unit time

**Abbreviations**

AMF	Air mass flow rate
AISI	American Iron and Steel Institute
CCD	Charge coupled device

CFD	Computational fluid dynamics
CRS	Central receiver system
CSP	Concentrating solar power
DISA	Flow meter calibration unit
DLR	German Aerospace Center
DNI	Direct normal irradiance
EBSM	Electron beam selective melting
HEM	Homogenous equivalent model
HiTRec	High temperature receiver
HTF	Heat transfer fluid
IEA	International Energy Agency
IRENA	International Renewable Energy Agency
LCOE	Levelized cost of electricity
LHS	Left hand side
LPG	Liquefied petroleum gas
LTE	Local thermal equilibrium
LTNE	Local thermal non-equilibrium
OVAR	Open volumetric air receiver
PHOEBUS	Technology Program Solar Air Receiver
PSA	Plataforma Solar de Almeria
PT	Parabolic trough
REIPPPP	Renewable Energy Independent Power Producer Procurement Program
RHS	Right hand side
RSS	Root-sum-square
RTE	Radiative transport equation
STERG	Solar Thermal Energy Research Group
TES	Thermal energy storage

# Chapter 1

## Introduction

### 1.1. Background to Research Problem

The energy production and consumption sector accounts for around two-thirds of global greenhouse gas emissions through the burning of fossil fuels, according to a joint report by the International Energy Agency (IEA) and the International Renewable Energy Agency (IRENA) (2017). In order to limit the global mean temperature rise to below 2 °C as stated in the Paris Climate Agreement, an extensive energy transition is required. This requires that low-carbon sources such as renewable energies increase from around 15 % of the primary energy sector in 2015, to 65 % in 2050 (IEA, 2017).

Renewable power generation technologies have already made rapid progress in installed capacity all over the world over the past few years. Since 2011 these technologies have made up more than half of the total new power generation capacity added globally, and in 2015 a record 148 GW of renewable power was added (IRENA, 2016).

Concentrating solar power (CSP) is considered a key contributor in the mix of renewable energy technologies. This technology has experienced an increase in momentum in the recent couple of years, especially in countries with high solar resources such as Morocco, United Arab Emirates, Chile and South Africa (IRENA, 2016). CSP had a global capacity of 4941 MW<sub>e</sub> in operation, with another 4162 MW<sub>e</sub> in planning by March 2016 (CSP Today, 2016).

#### 1.1.1. Concentrating Solar Power Technology

CSP technology uses concentrated solar radiation to heat up a heat transfer fluid (HTF), which is then used to power conventional power cycles. A typical CSP plant consists of four subsystems; the solar collector field, the receiver, the

thermal storage and the power conversion system. CSP technologies are commonly subdivided according to how the solar collectors concentrate the energy. The two leading technologies are parabolic troughs (PT) and central receiver systems (CRS), as illustrated in Figure 1.1. In a PT the solar radiation is focused along a collector tube running along the focal line of the trough, while a CRS have a field of heliostats (mirrors) that focuses the solar radiation on a central receiver on top of a tower.

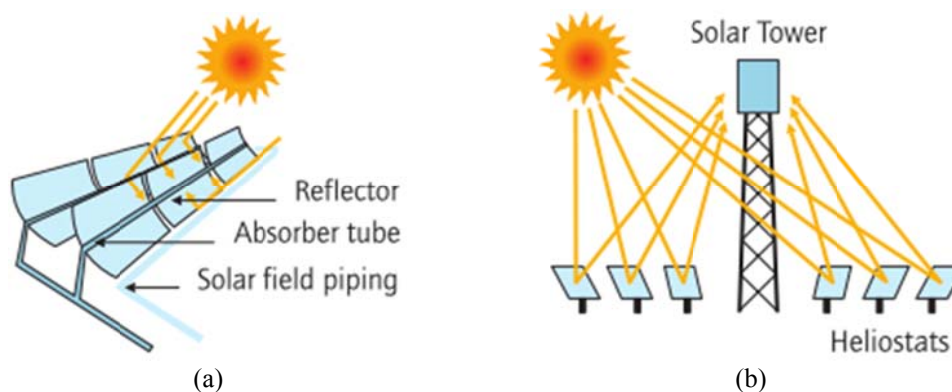


**Figure 1.1:** Two most dominant CSP technologies: (a) parabolic trough, (b) central receiver system (IEA, 2010)

The main advantage of CSP is the ability to incorporate a thermal energy storage (TES) system that enables the plant to operate flexibly and provide dispatchable energy. This ability cannot be matched by other renewable energy sources and implies an important role for CSP as a balancing power generation source in the mix of renewables. CSP also has various alternative applications such as industrial heating, cooling and desalination (Sager *et al.*, 2015).

CSP technology has been implemented in several countries over the world to produce electricity at utility scale. There is however still the need to reduce CSP electricity costs to make the technology more competitive with traditional fossil-fuel fired systems, since the expensive costs associated with this technology restrain the increased use and implementation thereof. The short 'proof time', absence of an established supply chain for the main components as well as a lack of government incentives and policies to support the technology all hinder the implementation of CSP in a country (Tobergte & Curtis, 2014). The advantage however is that there is no fuel cost over the rest of the plant's lifetime and when using this technology there are of course substantial savings in carbon emissions.

South Africa is endowed with excellent solar resources with more than 2500 hours of sunshine per year, at an average direct normal irradiation (DNI) of between  $4.5 \text{ kWh/m}^2$  and  $6.5 \text{ kWh/m}^2$  per day (Department of Energy, 2015). The province of the Northern Cape is the area that receives the highest DNI values, as illustrated in Figure 1.2. This area has therefore received considerable attention from CSP investors and developers in recent years.

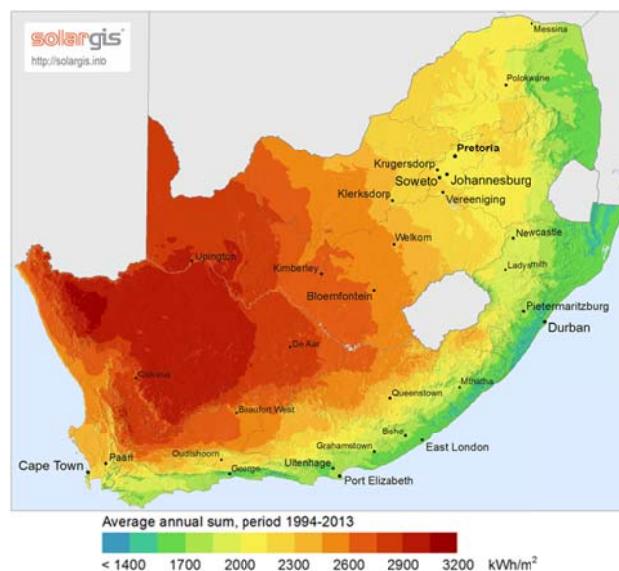


**Figure 1.2:** Direct normal irradiation for South Africa (DNI Solar Map © 2015 GeoModel Solar)

CSP is being developed in South Africa under the Renewable Energy Independent Power Producer Procurement Program (REIPPPP). Currently seven CSP projects are either in operation or under construction, of which five are PTs and two CRS plants and respectively named Bokpoort, Ilanga I, Kathu Solar Park, KaXu Solar One, Xina Solar One, Khi Solar One and Redstone Solar Thermal Power Plant<sup>1</sup>.

### 1.1.2. Central Receiver Systems

A CRS has a field of heliostats surrounding the tower, as shown in Figure 1.1 (b). Each heliostat has a dual axis tracking system. In combination this creates a 3-D concentrating system with a point focus. Therefore, this technology has the ability to achieve very high concentration ratios ranging from 200 to 1000 suns on the receiver, allowing higher HTF outlet temperatures compared to those achieved by PT systems. This enables the plant to achieve higher plant efficiencies and

<sup>1</sup> Yet to obtain financial closure and therefore not under construction (September 2017)



generate more electricity, thereby reducing the levelized cost of electricity (LCOE) (Lubkoll, 2017). The CRS technology is anticipated to deliver large cost breakthroughs in terms of design changes in the solar field as well as increased receiver efficiencies (Sager *et al.*, 2015). These characteristics will allow CRS to surpass PTs as the most cost competitive CSP technology by 2025 (IRENA, 2016).

There are different CRS classification criteria based on the receiver layout, HTF and the absorber material. The various CRS technologies and their different types, HTF and temperature ranges are shown in Table 1.1. The receiver provides thermal energy which can be used to drive a power cycle. The outlet temperature of the HTF typically dictates whether a Rankine or a Brayton cycle is used.

**Table 1.1:** Various central receiver technology types with their HTFs and operating temperatures (adapted from (Buck, 2016))

Technology	Type	HTF	Operating Temperature, °C
Volumetric receiver	Open volumetric receiver	Ambient air	< 800
	Closed volumetric receiver	Compressed air (4 to 10 bar)	< 1000
Tubular receiver		Ambient air	< 800
		Water/steam	< 600
		Molten salt (solar salt)	min 280, max 565
		Liquid metals	< 890
Direct absorbing receiver	Falling particle receiver	Particles	< 1000
Ceramic plate receiver	Flat receiver	Compressed air (4 to 10 bar)	< 1000

Open volumetric receivers have a simple and reliable design, but have lower thermal efficiencies due to the poor heat transfer characteristics of air. The use of pressurized air on the other hand requires an expensive and fragile quartz glass window. Tubular receivers allow the use of a wide range of HTFs, and state of the art receivers use molten salt. The maximum allowable flux intensities and thermal gradients over these receivers are however a drawback. The direct absorbing and ceramic plate receivers are new concepts in development, aimed to address some of the drawbacks of the other receiver types.

### 1.1.3. Thermal Energy Storage

A TES systems store excess heat collected by the solar field during times of high solar radiation. This stored thermal energy is then used when the solar resource is insufficient to produce the required heat input to the power conversion cycle. A TES is a major attribute of CSP plants since it increases the capacity factor of the plant and more importantly, allows dispatchable electricity generation (Zhang *et al.*, 2013).

A TES system most commonly stores sensible heat and can be implemented in either a direct or indirect way. In a direct system, the HTF heated in the receiver is directly stored in the TES. Examples are steam, oils and molten salt storages. Indirect storage is where the HTF circulates through the TES where a solid material absorbs and stores the heat from the HTF (Zhang *et al.*, 2013). Examples are packed bed storage systems. More advanced TES systems look at using latent heat storage, where a phase change material is used to store the energy. This technology type is however still far from cost effective at a commercial scale.

The costs of TES systems are high mainly due to the use of advanced storage materials and the volume required. The insulation required to keep the storage from losing the heat also significantly contributes to the overall costs.

## 1.2. Research Problem Statement

South Africa has exceptional solar resources providing an excellent platform for the use and implementation of solar energy as a renewable energy source. It is clear that CSP technology combined with TES offers a sustainable and dispatchable energy technology which may be competitive with traditional fossil fuel fired power plants. However, although the CRS has been commercially demonstrated, it is as yet far from mature from a cost perspective (Sawin *et al.*, 2016). The advanced technology and material requirements for these systems need to be addressed to make it more viable for local implementation.

Extensive work and research have been done at the Solar Thermal Energy research Group (STERG) at Stellenbosch University on developing cost-effective sensible heat storage in a packed bed of rock, with air as the HTF (Allen, 2014; Laubscher *et al.*, 2017). The rock bed is charged with ambient air that is heated to between 550 °C to 600 °C, and then blown into the bottom of the bed. The concept has been proved experimentally and is being installed and tested on a medium scale (400 kW<sub>th</sub>) at the test facility of Stellenbosch University. Currently

the rock bed TES makes use of a gas burner to supply the heat input to charge the TES for testing purposes. However, this system is to be retrofitted with a solar powered heat input. The charging conditions of the rock bed TES therefore provide clear requirements and boundary conditions that should be fulfilled.

A CRS with an open volumetric air receiver (OVAR) can produce the required heat input to charge the rock bed thermal storage. This type of receiver has an inherently simple design with the benefit of using a HTF that is freely and abundantly available and with no environmental impact. The hot outlet air from the receiver can directly be used to charge the rock bed TES, and therefore no additional heat exchanger is required. The combination of this receiver type and the thermal storage concept can provide an affordable and economical solution to produce and store high temperature thermal energy to either power a Rankine cycle, or be used for process heat applications.

An OVAR has to operate in extreme conditions of high incident flux and temperatures while being exposed to ambient air. These receivers also experience severe temperature cycling due to changes in weather conditions during operation, as well as diurnal cycling. This gives rise to several challenges to be solved, such as absorber material and durability, receiver efficiency and specific cost (Avila-Marin, 2011). The poor heat transfer characteristics of ambient, unpressurised air are also an important consideration for this receiver technology.

The problem then addressed in this research is to find a cost-effective and simple OVAR concept that can provide the hot air requirements for charging the rock bed TES. The selection of a suitable absorber material as well as a simple receiver structure is of the essence for the design and is the main focus of this research. This project is the starting point towards developing a large receiver that can eventually be manufactured and installed at the rock bed TES test facility.

### 1.3. Research Objectives

The main goal of this research is to identify and develop a suitable absorber for an OVAR that can be used to charge a rock bed TES. The aim is towards a simple and cost effective design that satisfies local manufacturing capabilities and material availability. The absorber plays a significant role in the thermal performance of the receiver and is therefore the focus of this project. The work is subdivided into the following smaller objectives:

- Identify and develop a suitable absorber concept that is cost-effective, locally available and can ultimately provide hot outlet air at

550 °C to 600 °C. The concept should have a modular design which allows future scale-up capabilities. The material, structure and layout of the absorber module are the focus of the design.

- Conduct a heat transfer analysis and implement it through a numerical model that can calculate and predict the steady state thermal performance of the absorber under various conditions. The model should provide clear insight into the heat and radiation transfer inside the absorber and form the basis for more detailed numerical models.
- Design a small scale OVAR test tower that can be used to experimentally validate the absorber concept and find discrepancies between the predicted performance of the absorber and the actual test measurements. The tower will be installed on an available medium flux concentrator and should allow the testing of different absorber materials and configurations.

The absorber concept will be evaluated not only by its thermal performance, but also by its relevance to be locally manufactured and implemented in a large receiver. The goal of the experiments is to prove the absorber concept and to demonstrate its capabilities. It is therefore not yet focused on receiver characterization and optimization.

## 1.4. Methodology and Scope

The methodology through which the goal of the project is achieved starts with developing an absorber concept based on a thorough review from literature of the available technology as well as by clearly identifying the boundary conditions and requirements of the absorber. This is followed by the heat transfer analysis and numerical modeling of the concept to calculate its thermal performance. The concept is then manufactured and tested on an experimental setup to measure the thermal performance under different conditions and validate the results from the model. Each step has its own smaller objectives. These steps are briefly discussed with reference to the scope and limitations of the project.

### *Develop an absorber concept:*

In order to develop a suitable absorber concept, an extensive review is conducted on available OVAR technology. The aim is to obtain a broad and in-depth understanding of this type of receiver in order to be able to address the most important design considerations. The requirements of the concept are then clearly identified and a concept is synthesized based on these considerations. This concept is not intended towards a novel OVAR, but aims to expedite the

advantages and lessons learnt from previous projects and combine them to synthesize a tailored solution that satisfies the requirements of this project.

This project is the starting point for the development of a large receiver. The scope is therefore limited to finding a suitable absorber concept, and not the development of a large receiver. The concept's limitations are the charging requirements of the rock bed TES as well as the low-cost requirement. The optimization of the concept is outside the scope of the project.

*Conduct a heat transfer analysis through developing a numerical model:*

The basic mathematical model of the absorber considers the fundamental mathematical correlations that describe the heat and radiation transfer inside the porous absorber material. The model acts as a preliminary design and investigation tool to determine the thermal performance at steady state conditions of the absorber. A 1-D model is used for this initial design stage since it enables a simple and insightful comprehension of the heat and radiation transfer within the absorber. The equations are implemented and solved iteratively in Matlab. The Matlab model paves the way for a more advanced numerical model using CFD in the future.

*Design, manufacture and test the concept on an experimental setup:*

A prototype of the absorber concept was manufactured and tested on a medium flux concentrator located on the solar rooftop lab of the Stellenbosch University Engineering faculty. The tower and receiver of the concentrator was redesigned to allow for the testing of the concept developed in this project. The main objective of the experimental tests was to measure the thermal performance of the absorber under different operating conditions. This was achieved by placing thermocouples throughout the absorber, as well as the rest of the setup, and to measure the temperatures for various conditions. The absorber configuration and the air mass flow rates (AMF) through the absorber are the two controlled parameters. The performance of the absorber was then calculated from these measurements and compared to the numerical results.

The capabilities of the test setup and concentrator dictated the limitations of the experiments. The performance of the absorber concept therefore depended on the available incident flux and power on the absorber's aperture during testing. The setup is located outside and exposed to ambient conditions, which introduce a large number of uncontrollable variables. The setup does however provide a better representation of the actual performance of the absorber since it include all the environmental influences that are not accounted for in an in-house test setup.

## 1.5. Brief Chapter Overview

Chapter 1 provided an introduction to the research. It clearly stated the research problem with the objectives that need to be reached. The methodology of the work was discussed and the scope and limitations clearly identified.

Chapter 2 is a literature review on OVAR technology, which investigates its working principle and absorber design considerations. The reference projects for this work are discussed and the rock bed TES mentioned.

Chapter 3 describes the absorber concept developed based on the findings from the literature review as well the requirements of the receiver. The concept is thoroughly discussed and its geometrical properties calculated.

Chapter 4 discusses the numerical model that was used to calculate the steady state thermal performance of the absorber. The results are provided and discussed.

Chapter 5 provides details of the experimental apparatus used to test the absorber concept. The various measurements and instrumentation used are discussed as well as the experimental procedure. The chapter also includes an uncertainty analysis for the measurements made.

Chapter 6 contains the results of the experimental tests. The performance of the absorber material is investigated and compared to the numerical model. A comparison is also made between these results and other similar work performed.

Chapter 7 is the concluding chapter that synthesizes the research with a summary of the main results and overall conclusions, as well as an outlook on future work and recommendations.

# Chapter 2

## Literature Review

### 2.1. Introduction

The literature review aims to establish a broad and in-depth understanding of the open volumetric air receiver technology, as well as previous studies that had been done on the development thereof. The findings and conclusions of this review aim to provide a comprehensive foundation and understanding for the absorber concept to be developed from.

A typical OVAR CRS plant layout is described in Figure 2.1. The figure shows the thermal storage as well as power block subsystems, which are the boundary conditions of the receiver.

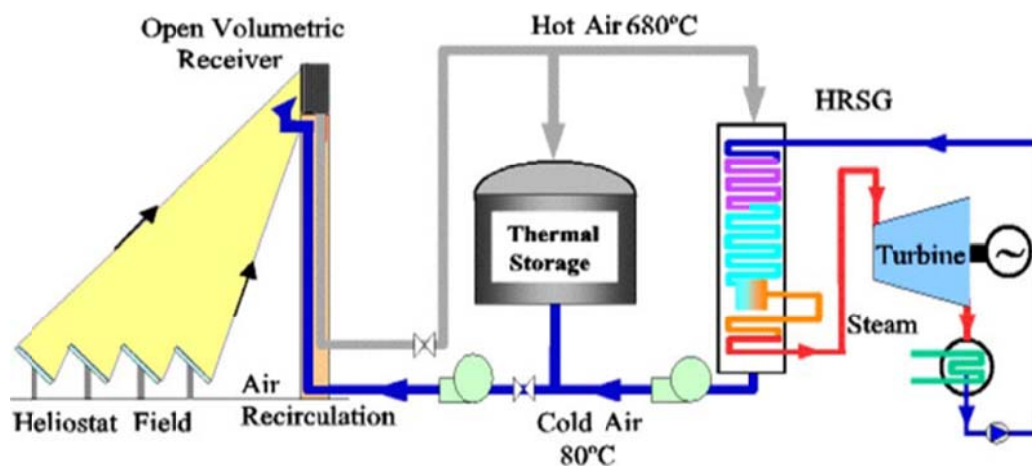


**Figure 2.1:** Flow diagram of a typical OVAR CRS plant with its different subsections (Avila-Marin, 2011)

The heliostat field provides the incident flux on the receiver which then produces hot air to charge the thermal storage and heat input to the power cycle. The return

air loop sends preheated air back to the receiver. The scope of this project does not include the power cycle and therefore only considers the receiver with the input from the heliostat field and the output to the thermal storage.

Volumetric receivers can be classified into four concepts based on their air pressure: ambient or pressurized, and absorber material: ceramic or metallic (Hoffschmidt *et al.*, 2003). Receivers that make use of ambient air are referred to as ‘open’ since they do not require a window and are open to the ambient. Since the objective of this project is to find a receiver concept that heat up ambient air, only open volumetric receivers are further investigated. The rest of this chapter focuses on the working principle, HTF, absorber material as well as important design considerations and challenges of OVARs. The reference OVAR projects for this work as well as the rock bed TES test facility are briefly discussed.

## 2.2. Open Volumetric Air Receiver Technology

The OVAR technology has made intense progress since the pioneering experiences of the late 1970s (Romero-Alvarez & Zarza, 2007) and is recently being considered an option again (Avila-Marin, 2011). These receivers have clear advantages over other receiver technologies and can resolve some of the limitations and challenges of CRS. They however also still have a wide margin for improvement (Capuano *et al.*, 2017).

### 2.2.1. Working Principle

In volumetric receivers, a highly porous structure absorbs the concentrated solar radiation and acts as a convective heat exchanger. The HTF (air) absorbs the solar radiation inside the structure volume when forced through it (Romero-Alvarez & Zarza, 2007). The high porosity of the absorber allows the solar radiation to penetrate into the depth of the absorber. The ideal volumetric receiver produce the so-called volumetric effect, where the irradiated side of the absorber is at a lower temperature than the volume inside (Behar *et al.*, 2013). This volumetric effect is the result of the cooling of the incoming air to the front of the absorber, which significantly reduces the thermal losses from the receiver and increases its efficiency. Figure 2.2 compares the heat transfer principle between a tubular and volumetric receiver, and illustrates the advantage of the volumetric receiver.



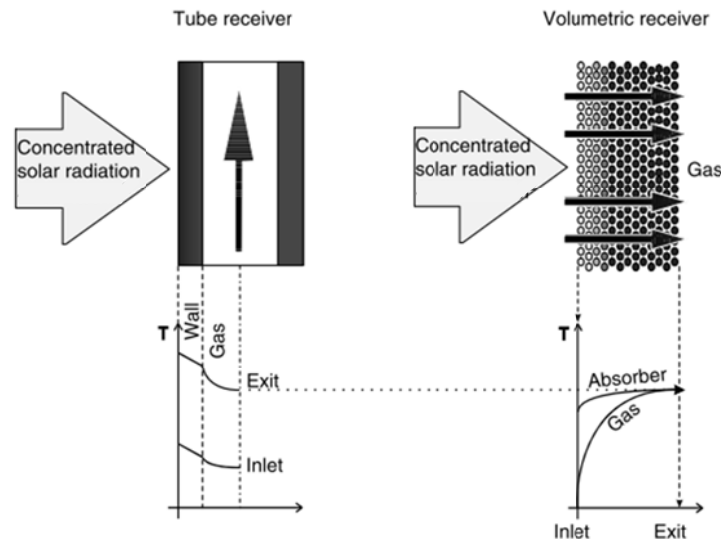


**Figure 2.2:** Heat transfer principle in tubular and volumetric receivers (Fend, 2012)

The volumetric absorber simplifies the heat transfer mechanism since both absorption and convection heat transfer take place on the same surface (Hoffschmidt *et al.*, 2003). The large absorption surface area combined with the cooling effect of the incoming air allows the receiver to operate in higher flux intensities, which reduces the required receiver size and lower its thermal losses.

The AMF through the absorber is determined by the pressure difference between the front and back of the absorber and is produced by a blower or fan. An OVAR operates in an open-loop where ambient, non-pressurized air is sucked in through the absorber. In a closed-loop or pressurized volumetric receiver, the absorber is sealed from ambient air by a transparent window to allow pressurized air to flow through the absorber.

An OVAR have a simple and reliable design and is applicable to the Rankine cycle where the hot air is passed through a steam generator (Avila-Marin, 2011). Closed volumetric receivers are able to achieve higher outlet temperatures due to the better heat transfer of pressurized air (higher density). These receivers are applicable in a Brayton gas cycle where pressurized air is required at high temperatures.

### 2.2.2. Air as Heat Transfer Fluid

The use of non-pressurized ambient air as the HTF for a volumetric receiver is based on its intrinsic advantages such as availability, high temperature capabilities as well as a less complicated receiver design requirement (Romero *et al.*, 2002).

However, the biggest drawback is its poor heat transfer characteristics that cause the efficiency of the receiver to be quite low. The large heat transfer surface inside the volumetric absorber aims to compensate for this drawback. Table 2.1 provides a summary of the merits and demerits of ambient air as HTF.

**Table 2.1:** Merits and demerits of non-pressurized air as HTF

Merits	Demerits
<ul style="list-style-type: none"> <li>• Freely and abundantly available</li> <li>• High operating temperatures possible</li> <li>• No phase change or freezing</li> <li>• Does not require water cooling</li> <li>• No environmental effect</li> <li>• Volumetric effect possible which increase receiver efficiency</li> </ul>	<ul style="list-style-type: none"> <li>• Poor thermal characteristics</li> <li>• High AMF and large heat transfer area required</li> <li>• Large area exposed to ambient increase thermal losses</li> <li>• Wind sensitive since open to ambient</li> </ul>

### 2.2.3. Absorber Material

Volumetric absorbers are exposed to demanding conditions such as concentrated solar radiation, high temperatures, frequent thermal cycling and have to operate in the presence of air. The range of available materials are therefore limited, and in order to maintain operation in the aforementioned conditions the material should have the following properties (Fend, 2012):

- High solar absorption (dark) in the solar spectrum band
- Low emittance in the infrared band
- High heat transfer to air
- High specific surface area to allow heat transfer
- Low thermal gradient and thermal stresses
- High temperature resistance to any degradation or scale formation which will lower heat transfer to the air

The maximum operating temperature of a volumetric absorber depends on the melting point of the material as well as its resistance to corrosion (for durability). The latter being caused by the oxidation process that takes place at high temperatures in the presence of oxygen (Gomez-Garcia *et al.*, 2016).

The choice of material is mainly dictated by the operating requirements of the receiver. The two most commonly used materials are ceramics and a metallic material in the form of stainless steel.

### 2.2.3.1. *Ceramic Absorber*

Ceramic materials are the most appropriate when air at temperatures above 800 °C are required. They allow for higher flux intensities and gradients over the absorber, which decrease the required aperture size, increase operation time and lower the system cost (Hoffschmidt, 2001). Ceramic absorbers can withstand average flux intensities of more than 500 kW/m<sup>2</sup> (Avila-Marin, 2011). This material is currently used in the High Temperature Receiver (HiTRec) (Hoffschmidt *et al.*, 2003) installed at Jülich (Hennecke *et al.*, 2007).

Various geometries are possible with the use of ceramic materials since several manufacturing processes can be used. The honeycomb structure is shown in Figure 2.3 (a) and ceramic foam in Figure 2.3 (b). The honeycomb allows better penetration of the incident radiation, while the foam has a higher cell density and therefore a higher specific surface area to allow heat transfer. The shape of these absorber modules can vary according to the requirements of the larger receiver.

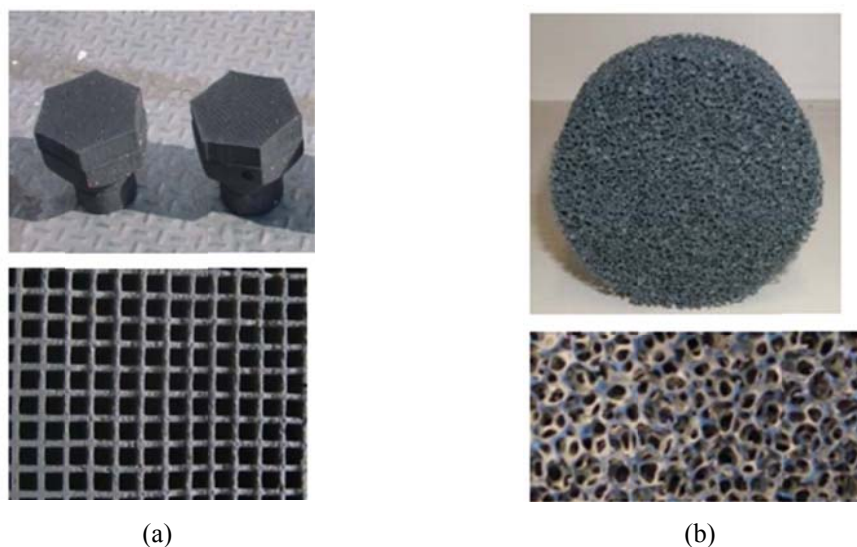


**Figure 2.3:** Ceramic (SiSiC) absorber module and close-up thereof, from (Fend, 2012): (a) monolithic honeycomb, (b) ceramic foam

### 2.2.3.2. *Metallic Absorber*

Metallic absorbers are considered for operating temperatures below 800 °C. These materials can withstand average flux values of around 250 kW/m<sup>2</sup> (Avila-Marín *et al.*, 2013). They allow better heat transfer between the air and the absorber and also have a quicker response to load changes and conditions. Stainless steel materials such as AISI 316 or 310 and Cr-Ni alloys such as Inconel are usually used, since these materials can withstand the high operating temperatures.

The wire pack concept was one of the first metallic absorbers to be tested and consisted of several screens of stainless steel wire mesh (Fricker *et al.*, 1988). Avila-Marín *et al.* (2013) tested this concept in lab-scale conditions with the aim to investigate the effect of changing geometrical properties through the depth of the absorber. The wire screens are shown in Figure 2.4 (a). Achenbach *et al.* (2013) also tested a wire mesh absorber. Another typical wire pack absorber is stainless steel knit wire, shown in Figure 2.4 (b). This absorber type was tested by Hoffschmidt (1996) as well as by Hellmuth and Matthews (1997) and is used in the Phoebus-TSA receiver, which is discussed later in this review. Flow instabilities are however a problem for the wire mesh absorber due to its high porosity (Avila-Marín, 2011).



**Figure 2.4:** Metallic absorbers (a) wire mesh screens (Avila-Marín *et al.*, 2013), (b) knit wire absorber from the Phoebus-TSA receiver (courtesy of F Dinter at PSA, 2016)

More recently developed metallic absorbers are illustrated in Figure 2.5 and include a corrugated metal sheet absorber (Pabst *et al.* 2017) and a state-of-the-art absorber that has an optimized geometry that aims to increase the overall thermal efficiency (Capuano *et al.* 2017). This second concept showed the presence of the volumetric effect during experimental testing. In order to manufacture the detailed geometry an advanced technique called electron beam selective melting (EBSM) is used to create the optimized pin-like geometry from titanium-aluminum alloy.

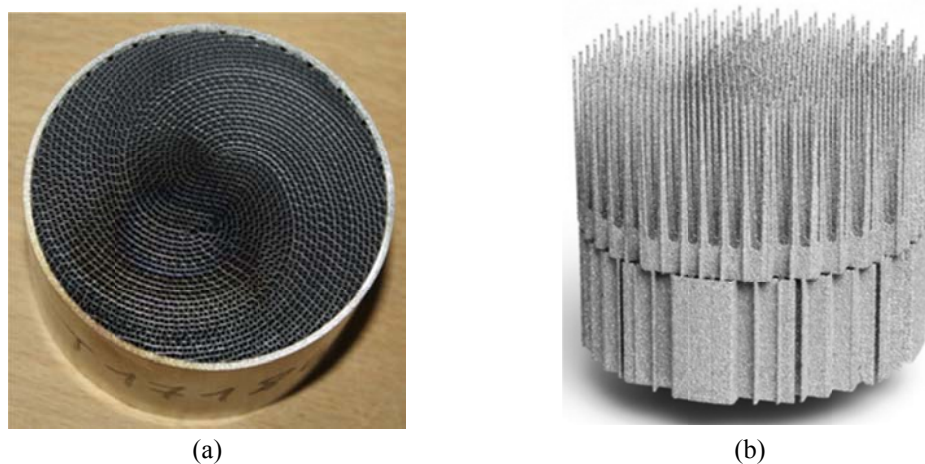


**Figure 2.5:** Optimized metallic absorbers (a) MetRec-technology with corrugated metal sheets (Pabst *et al.* 2017), (b) optimized absorber concept (Capuano *et al.*, 2017)

#### 2.2.4. Design Considerations and Challenges

Although an OVAR has a simple design and layout, there are several important design considerations that should be carefully addressed in order to obtain a receiver with a competitive performance output. Typical challenges of the OVAR were identified by Hoffschmidt (1996) and are discussed below.

##### 2.2.4.1. *Flow instabilities*

Non-homogeneous radiation on the front of the receiver creates areas where flow instabilities can occur due to changes in temperature dependent air properties (viscosity and density) due to the non-uniform heating (Ho & Iverson, 2014). This self-reinforcing effect may lead to local over heating or ‘hot-spots’ and can cause failure of the absorber material. One way to mitigate the unstable flow rate distribution throughout the absorber, an adequate pressure drop should be maintained over all parts of the receiver at all times. The mass flow distribution needs to be adapted to the incident concentrated flux profile over the surface to ensure sufficient airflow through the whole of the absorber. This is achieved by inserting perforated plates or orifices corresponding to the local flux intensities behind the absorber material (Romero & Steinfeld, 2012).

##### 2.2.4.2. *Low thermal efficiencies*

The low thermal efficiency is typically due to the poor heat transfer characteristics of air and since the OVAR is exposed to ambient conditions where convective,

conductive and radiation losses can possibly be significantly high. These overall thermal losses can be reduced through decreasing the absorber area, insulating the receiver and increasing the absorber absorptivity. The efficiency of the absorber is also significantly increased when the convective heat transfer coefficient is improved (Kribus *et al.*, 2014). This causes enhanced cooling of the front, which lowers the thermal losses, and increases the outlet temperature due to the better convective transport. The implementation of a hot return air loop can also increase the efficiency of the receiver by recycling the energy in the outlet air, as well as protect the inner structure of the receiver from overheating.

#### 2.2.4.3. *Effect of Absorber Properties*

It is important to understand the effect of different properties of the material with respect to the absorber's performance to find an efficient yet simple design. Two significant properties of a volumetric absorber are its porosity and thermal conductivity.

High values of porosity facilitate better penetration of the radiation into the porous absorber which lower both reflection losses and lead to a lower surface temperature causing lower thermal losses. However, flow instabilities inside highly porous absorber materials lead to local overheating and failure of the absorber. By lowering the absorber porosity the thermal efficiency is decreased but the durability against thermal shock and high temperature gradients is significantly increased (Hoffschmidt, 2001).

A high thermal conductivity is essential to conduct the heat from the front into the structure. However, absorber materials with very high convective heat transfer coefficients at the aperture require a low thermal conductivity that can create a temperature gradient along the cross-section of the absorber to maintain the maximum temperature inside the structure (Gomez-Garcia *et al.*, 2016).

### 2.3. Reference Open Volumetric Receiver Projects

In a review Avila-Marin (2011) thoroughly discusses the complete development of volumetric receivers. In this section a brief overview of the projects and receivers that are used as reference for this project are discussed.

### 2.3.1. Phoebus-TSA

The Phoebus-TSA project is considered as the reference development for OVARs with metallic absorbers (Avila-Marin, 2011). The project made use of a 2.5 MW<sub>th</sub> volumetric receiver with coiled knit wire packs placed in hexagonal cups to serve as the absorber, shown in Figure 2.6. The cups were 280 mm in diameter and 50 mm deep, as illustrated in Figure 2.4 (b).



**Figure 2.6:** Hexagonal cups filled with knit wire in the Phoebus-TSA receiver (from (Avila-Marin, 2011))

The receiver was tested in 1993 at PSA and achieved an absorber efficiency of 85 % at 700 °C outlet air temperatures with average flux values of 300 kW/m<sup>2</sup> on the receiver. The receiver implemented an air return ratio of 60 %. The tests concluded that the receiver was able to maintain constant outlet temperatures through the system control, as well as match the air flow rate through the absorber with the incident flux distribution.

### 2.3.2. HiTRec

Kribus *et al.* (1996) concluded that airflow instability inside the porous absorber when operating under high-flux intensities can cause low thermal efficiencies and the destruction of the absorber material. This resulted in further research and development of the receiver whilst the absorber material was considered separately (Hoffschmidt *et al.*, 2003). The concept for the HiTRec was developed with this in mind and is illustrated in Figure 2.7. This receiver system is therefore not linked to a specific absorber material, as long as it can be installed in the absorber module.



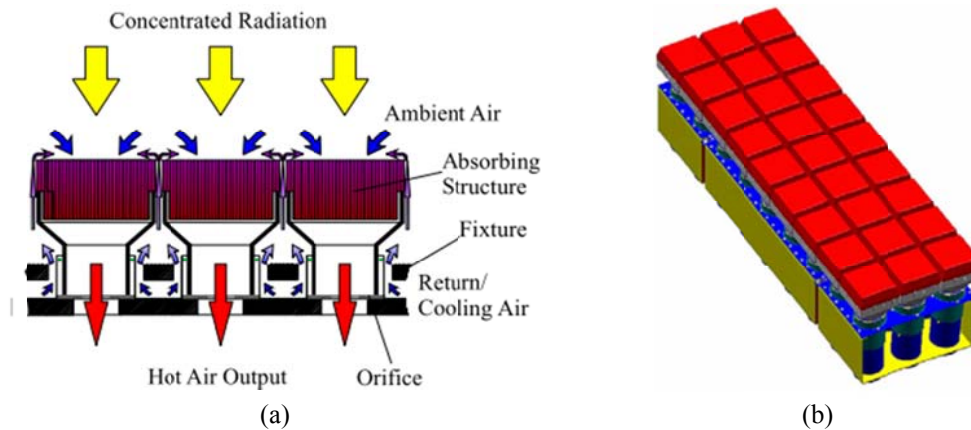


**Figure 2.7:** HiTRec concept: (a) cross-section and air flow diagram, (b) receiver subassembly with the mounted absorber modules from (Hoffschmidt *et al.*, 2003)

The shape of the absorber modules are quadratic instead of hexagonal based on the clear advantage of the scaling of this receiver. Each absorber module is separated with a gap that allows movement between the modules due to thermal expansion. It also allows the implementation of a return air loop that helps cool down the steel back structure and recover waste heat. The HiTRec concept can be used to test any new or advanced absorber material (Hoffschmidt *et al.*, 2003).

## 2.4. Rock Bed Thermal Energy Storage System

This section provides a brief overview on the rock bed TES that are to be retrofitted with an OVAR. The charging conditions of the storage provide the boundary conditions of the receiver, and are discussed in more detail in Chapter 3. The storage consists of a conical shaped rock bed which is charged by blowing hot air at 550 °C to 600 °C into the bottom of the pile and then storing the sensible heat in the rocks. The concept is shown in Figure 2.8.



**Figure 2.8:** Rock bed TES test facility (courtesy of HF Laubscher)



In Figure 2.8 the gas burner is located in the square box after the blue fan and operates on LPG gas as an alternative heating source to charge the storage at the moment. The burner will be retrofitted with an OVAR to prove and motivate the feasibility of using CSP with an OVAR in combination with a rock bed TES to provide a simple and cost effective solution to produce and store high temperature thermal energy.

A qualitative temperature distribution through the rock bed is shown in Figure 2.9 and illustrates the idea behind this TES concept.

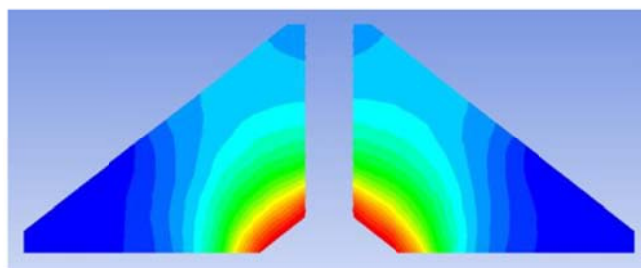


**Figure 2.9:** Qualitative temperature distribution in the rock bed TES when it is charged produced with ANSYS Fluent (Laubscher *et al.*, 2017)

## 2.5. Conclusion

The literature review provided a thorough understanding of OVARs and the main aspects of its design and operation. Using air as HTF has several advantages such as its availability and high temperature capabilities, however, its drawback is the poor heat transfer characteristics at ambient pressure. The absorber material should be able to handle the high temperatures and flux intensities and are either ceramic or metallic materials, with metallic materials being suitable for operating temperatures below 800 °C, and ceramics for higher temperatures. The possibility of flow instabilities as well as low thermal efficiencies is some of the important design considerations of an OVAR. The Phoebus-TSA and HiTRec projects provide a clear reference for this project and the overview of the rock bed TES facility state the requirements for the receiver. The review provided a good foundation upon which a concept could be developed that satisfies the requirements of this project. The absorber concept is discussed in the next chapter.

# Chapter 3

## Absorber Concept

### 3.1. Introduction

The aim of this chapter is to motivate and explain the concept that was developed for an OVAR that will satisfy the objectives of the project. This idea is not to design a novel concept, but rather to expedite the advantages and results from other projects and combine these to synthesize a tailored solution for an OVAR. To simplify the scope of this project, the focus was on the absorber and finding a cost-effective and simple concept which can be locally sourced and manufactured. First the operating requirements and boundary conditions for the receiver are recognized in order to clearly identify the design objectives. Possible solutions were then investigated and synthesized to finally provide a concept for further development.

### 3.2. Receiver Requirements

The receiver will eventually be used to charge the rock bed TES. Atmospheric air is therefore the non-negotiable HTF. The charging requirements of the rock bed provide the boundary conditions of the air leaving the receiver. These operating conditions are summarized in Table 3.1.

One of the objectives of the project is to experimentally test and prove the absorber concept with the use of a previously built medium flux concentrator. The concentrating capabilities of the experimental test setup will therefore be used as the input flux boundary conditions. A detailed description of the experimental setup and the calculated values in Table 3.2 can be found in Chapter 5.

**Table 3.1:** Rock bed TES charging conditions (Laubscher *et al.*, 2017)

Parameter	Unit	Condition
HTF	-	Air
Inlet pressure	kPa	101.3 (atmospheric)
Heating capacity	kW <sub>th</sub>	400
Max charging temperature	°C	550 to 600
Max outlet temperature	°C	40 to 50
Charging AMF	kg/s	± 0.6

**Table 3.2:** Concentrating capabilities of the medium flux concentrator

Parameter	Unit	Condition
Total collector area	m <sup>2</sup>	1.39
Focal spot area	m <sup>2</sup>	0.0156 (0.125 m x 0.125 m)
Average concentration ratio	-	71.2
Peak incident flux	kW/m <sup>2</sup>	110*
Average incident flux	kW/m <sup>2</sup>	67.8*

\* When the DNI = 950 W/m<sup>2</sup>

### 3.3. Design Objectives

The detailed design objectives are in line with the overall project objectives, but are more focused and based on the requirements and boundary conditions identified in Table 3.1 and Table 3.2. The absorber concept should conform to the requirements of the TES as well as the capabilities and size limitations of the concentrator. The following objectives were identified for the concept design:

1. Use locally available materials and manufacturing processes to ensure a low-cost and simple concept.
2. The absorber materials used should be able to withstand high temperatures and flux intensities and be able to produce the desired outlet temperatures.
3. The concept should be modular and allow for future scale-up possibilities.

The design challenges and considerations identified in the literature review should also be considered and incorporated in the concept development.

### 3.4. Synthesis of Solutions

The main consideration in developing a suitable concept is the absorber material. A metallic absorber is appropriate for this use since the outlet temperature requirements of the receiver are within its operating capabilities. Although ceramic materials can handle higher temperatures and therefore flux intensities, a trade-off should be made between a high performing and cost effective, locally available solution. There is also no supplier in South Africa for typical ceramic materials used for volumetric absorbers. The wire pack absorber can be locally sourced and does not require any further manufacturing for its use as an absorber material. A wide variety of geometrical properties are also available for this material, which can be altered and combined to optimize the absorber. Furthermore, various grades of stainless steel wires, such as AISI 316 and 310, are available that can withstand the extreme operating conditions. This type of material forms a stable, well-adhered oxide layer on the wire surface at elevated temperatures in the presence of air, which darkens the color of the bright material.

The literature review in Chapter 2 found that the wire pack absorber can be divided into two groups: wire mesh screens and knit wire. The wire mesh screens have a plain weave and structured wire configuration, as shown in Figure 3.1 (a). In knit wire on the other hand, the wires are knitted together and are more unstructured, as shown in Figure 3.1 (b).

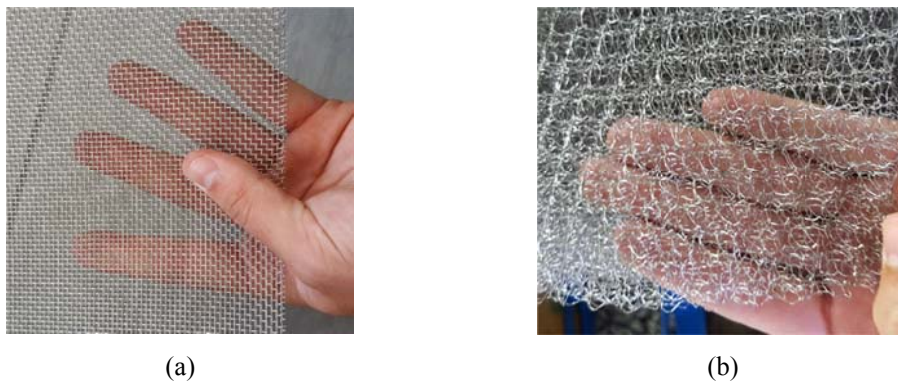


**Figure 3.1:** Example of a wire mesh screen in (a) and knit wire in (b)

The wire mesh screens is favored above the knit wire, since Kribus *et al.* (2014) concluded that geometric optimization with parameters such as porosity and pore size is not sufficient to achieve the desired high efficiencies of volumetric absorbers. To improve the performance it is advised that absorber properties are changed through the depth of the material. This can effortlessly be implemented

with the use of different wire mesh screens through the depth of the absorber. The increase of the volumetric heat transfer coefficient is another important consideration which can significantly enhance the absorber efficiency (Kribus *et al.*, 2014). This can be achieved by having a higher specific surface area for the heat transfer to take place on, as well as through increasing the Reynolds number by placing the screens in a staggered arrangement.

The wire mesh screen absorber with a gradual decreasing porosity have been experimentally tested by Avila-Marin *et al.* (2013) at the CIEMAT-PSA test facility. Three different wire mesh screens were used, each with a different porosity and in different combinations to create the gradual porosity. The screens were made from AISI 310 wires and had the characteristics provided in Table 3.3:

**Table 3.3:** Wire mesh screen properties tested at PSA by Avila-Marin *et al.* (2013)

Property	Unit	Different screens		
Wire diameter	mm	0.63	0.50	0.70
Aperture size	mm	1.00	1.40	2.50
Open area ratio	-	0.38	0.54	0.61

Three different absorber configurations were tested: 61-54, 61-38 and 54-38, with the numbers referring to the porosity from the front to the back of the absorber. The absorbers typically consisted of 7 to 10 screens in total. The results show that with the 61-38 absorber outlet temperatures of 320 °C to 580 °C were reached with efficiencies of 88 % to 72 %. The tests were performed under average flux intensities of 220 kW/m<sup>2</sup> to 260 kW/m<sup>2</sup>. The results demonstrate the capabilities of the wire mesh screen absorber and that it also satisfies the other requirements for this concept, since it is a simple concept and can be locally sourced.

Another important consideration is how the absorber material will be installed in the receiver. The modular-cup layout of the HiTRec receiver allows easy experimental testing of a single cup as well as excellent scalability towards a larger receiver by simply adding more of these cups in a matrix. The square cup can be easily manufactured with stainless steel sheet metal and through simple bending and welding processes. Different absorber materials can be inserted and tested in this cup.

### 3.5. Gradual Porosity Wire Mesh Absorber

The wire mesh screens with a gradual decreasing porosity were identified as a suitable concept that satisfies the requirements of this application when installed in a modular absorber cup. In the rest of this document 'wire mesh' refers to the use of wire mesh screens, and not knit wire.

#### 3.5.1. Concept Layout

This wire mesh absorber is placed inside a modular absorber cup, based on the HiTRec design. A similar concept has been tested by Achenbach *et al.* (2013). The cup is mounted inside a receiver housing, which is insulation on the outside and represent the environment of a large receiver for the cup on the inside. An annotated cross section is shown in Figure 3.2 to explain the concept layout. The overall size and dimensions are based on the available test setup capabilities. The absorber has an aperture of 110 mm x 110 mm and the receiver housing is 145 mm deep to accommodate the cup. Further details are provided in the discussions of the absorber and cup that follows.

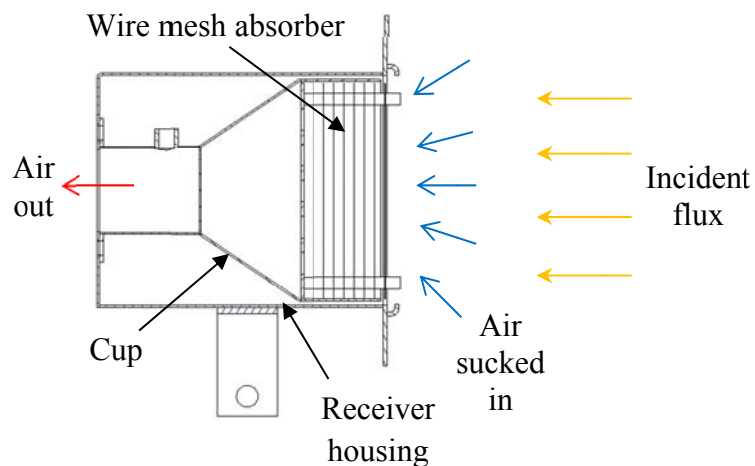


**Figure 3.2:** Annotated cross-sectional view showing the layout and air flow of the absorber concept

#### 3.5.2. Wire Mesh Screen Absorber

The absorber consists of three different mesh screens, with a certain amount of each screen used in a configuration. The screens used are M6, M12 and M24, where the names indicate the mesh number (holes per inch). These screens were

identified based on the findings of Avila-Marín *et al.* (2013), as well as the availability from a local supplier. The screens are plain weave and made from stainless steel AISI 316 wires. The screens are cut in 110 mm square blocks. The final absorber configuration goes from a high porosity screen in the front to a low porosity at the back, as illustrated in Figure 3.3.

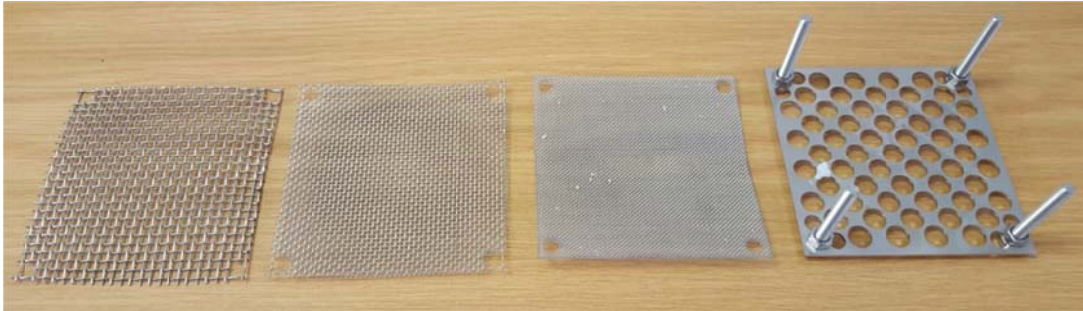


**Figure 3.3:** Single sheet of each different wire mesh screen used (M6, M12 and M24) as well as the perforated back plate on which the stack is mounted with its bolts

The main objective of the gradual porosity is to have a low front surface area that allows good penetration of the incident flux and lowers the radiation and reflection losses from the aperture. A coarse mesh with a large open area ratio is therefore used in the front, with an in-line wire arrangement. The finer mesh deeper into the cup provides a higher specific surface area that enhances the convective heat transfer. These meshes are in a staggered arrangement resulting in an improved volumetric heat transfer coefficient, since the Reynolds numbers are larger (Avila-Marín *et al.*, 2017). Since these meshes have a lower porosity, more radiation is absorbed by the mesh in this part and therefore an increase in mesh temperature as result, which promotes the volumetric effect by increasing the temperature of the absorber on the inside.

A number of different screen combinations were tested, with each absorber configuration identified by the number of screens of each mesh type used. This is presented in the following way (no. of M6 screens/ no. of M12 screens/ no. of M24 screens), for e.g. (6/4/2) or (5/5/5). The final absorber then consists of this configuration of mesh screens kept in place on a perforated back plate by four bolts, as shown in Figure 3.4. This back plate maintains the square shape of the screens under the thermal loads and the bolts keep the screens together. The size of the holes in this back plate can be altered to adjust the pressure drop or flow rate through absorber. The compression of the mesh stack can be altered with the bolts to enhance or reduce screen contact and radial mixing of the air behind the screens, depending on which effect is more desired.





**Figure 3.4:** Mesh configuration mounted on perforated back plate as absorber

The conduction in the wire mesh absorber can be divided into in-plane conduction in each mesh screen, and effective absorber conduction through the depth of the absorber and all the screens. The screens typically have poor in-plane conduction since the wires make little contact with each other. A low effective thermal conduction on the other hand helps to maintain the highest temperatures inside the absorber, however it also prevents the heat from being conducted into the absorber from the front. These parameters can be influenced or controlled through using specific screens with the desired properties, and by altering the compression of the absorber configuration with the four bolts.

Initially the mesh has a very high reflectivity due to the bright color of new stainless steel wires. The oxidation that occurs on the wire's surface when the mesh experiences high temperatures causes it to obtain a darker, more desirable color. Therefore the absorber does not require any coating to further enhance its absorptivity.

### 3.5.3. Modular Absorber Cup

The absorber configuration is placed inside a modular stainless steel cup, shown in Figure 3.5. The front of the cup is 110 mm x 110 mm and 40 mm deep and taper down with a loft into a 44 mm diameter pipe. The aperture is slightly smaller than the focus area of the concentrator to ensure a more uniform incident flux distribution over the aperture. The cup is deep enough to ensure adequate space to test different absorbers. A flange at the end of the pipe section is used to mount the cup inside the receiver housing with bolts.



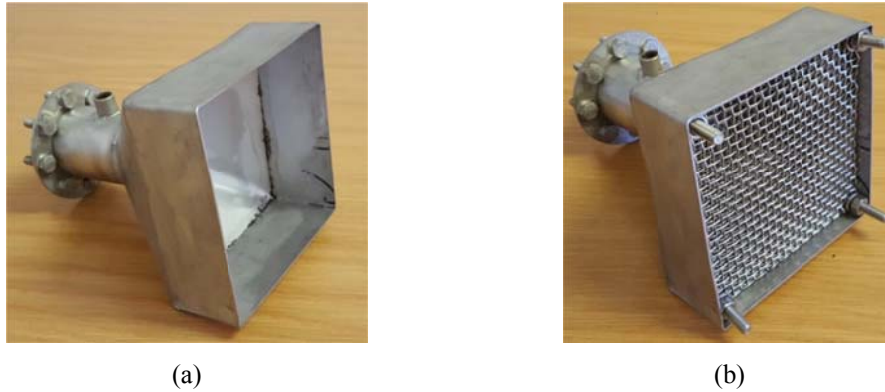


**Figure 3.5:** Modular cup design without (a) and with (b) the wire mesh absorber installed

The material used to manufacture the cup is 1.5 mm thick stainless steel AISI 316 sheet metal. This material can withstand the high temperatures experienced during operation as well as the thermal cycling. This material was chosen as it is less expensive and more available than AISI 310. The cup is manufactured through simple bending and welding processes. The square shape of the cup allows easy scalability towards a larger receiver by simply adding more of the cups in a matrix formation. The cup design allows the absorber to be easily installed from the front. In a full scale receiver this also allows easy access to broken cups or absorbers which simplifies maintenance on the receiver. The square shape is also chosen above the hexagonal shape for simpler manufacturing purposes. The nipple on top of the outlet pipe is for installing a fitting in which a thermocouple can be mounted to measure the outlet air temperature of the absorber.

### 3.6. Wire Mesh Geometrical Properties

The absorber's characteristics are dictated by the geometrical properties of the wire mesh screens used. The wire diameter,  $d$ , and the screen's aperture size,  $H_{ap}$ , is provided by the supplier. With this information the other geometrical properties are calculated, as done in Zhao *et al.* (2013).

The mesh numbers used in the names of the three different screens (M6, M12 and M24) indicate the number of holes per inch of screen. This mesh number is recalculated and defined as the number of holes per millimeter of screen:

$$M = \frac{1}{d + H_{ap}} \quad (3.1)$$

The open area ratio is:

$$oar = \frac{H_{ap}^2}{(H_{ap} + d)^2} \quad (3.2)$$

The volumetric porosity is defined as the ratio of void volume to the total volume:

$$\varphi = 1 - \frac{\pi M d C}{4 c f} \quad (3.3)$$

The compactness factor,  $cf$ , describes how compressed the screens are against each other and is generally not bigger than one. If the screens are not compressed and in-line arranged,  $cf$  is equal to one; for staggered arrangement,  $cf$  is smaller than one (Zhao *et al.*, 2013).

The multiplication factor is used to calculate the porosity and specific surface are:

$$C = \left( \frac{Md}{2} + \frac{1}{2Md} \right) \arcsin \left( \frac{1}{\frac{Md}{2} + \frac{1}{2Md}} \right) \quad (3.4)$$

The specific surface area is calculated with:

$$\alpha_{sf} = \frac{\pi M C}{c f} \quad (3.5)$$

The pore hydraulic diameter is used to calculate the Reynolds number:

$$d_h = \frac{4\varphi}{\alpha_{sf}} \quad (3.6)$$

The calculated depth of a complete absorber configuration depends on the amount of each screen type ( $M_x$ ) used,  $no_{\cdot M_x}$ , the wire diameter of that screen,  $d_{M_x}$ , and its compactness factor  $cf_{M_x}$ . The total depth of the absorber is then:

$$Z = \sum cf_{M_x} (no_{\cdot M_x} 2d_{M_x}) \quad (3.7)$$

The wire diameter is doubled since the screen is woven and the thickest part is where the two wires cross over one another. Table 3.4 provides the calculated geometrical properties of the three different screens used.

**Table 3.4:** Wire mesh geometrical properties for the absorber concept developed

Property	Symbol	Unit	M6	M12	M24
Wire diameter	$d$	mm	0.9	0.55	0.37
Aperture size	$H_{ap}$	mm	3.33	1.57	0.69
Mesh number	$M$	mm <sup>-1</sup>	0.24	0.47	0.94
Open area ratio	$oar$	-	0.62	0.55	0.42
Porosity	$\varphi$	%	82.3	78.7	70.4
Specific surface area	$\alpha_{sf}$	m <sup>-1</sup>	765	1548	3199
Pore hydraulic diameter	$d_h$	mm	4.33	2.03	0.88

The following absorber configurations were used: (6/10/10), (5/5/5), (6/10/0), (10/0/0), (6/4/2). All of them started with the highest porosity in the front and then decreasing gradually. The M6 screens were positioned as good as possible in an in-line arrangement, while the M12 and M24 screens were assumed staggered since the positioning of the finer screens could not be maintained that accurate inside the absorber. Through visual inspection this assumption was confirmed. The thicknesses of the different configurations ranged from 11 mm to 25 mm.

### 3.7. Conclusion

The wire mesh absorber with a porosity decreasing through its depth was identified as a suitable concept to absorb the concentrated solar radiation and to produce the required hot outlet air. This concept satisfies the requirements and is a cost-effective and locally available solution. The modular absorber cup provides a suitable and scalable design. The details of the wire mesh screens used in this concept were discussed and the different absorber configurations identified. The next chapter investigates the numerical model of the heat and radiation transfer inside the porous material to obtain a calculated theoretical performance at steady state conditions.

# Chapter 4

## Numerical Heat Transfer Model

### 4.1. Introduction

The numerical model of the absorber considers the fundamental mathematical correlations that describe the heat and radiation transfer inside the porous absorber material. A simplified 1-D numerical approach is used as a preliminary design and investigation tool to determine the thermal performance of the absorber at steady state conditions and to investigate the effect of certain parameters on its performance. The 1-D approach is suitable since it can produce realistic performance results and be computationally convenient as well (Capuano *et al.*, 2015).

This chapter starts with a brief review on previous modeling of open volumetric receivers. The governing equations with their assumptions used in this work are then discussed, followed by the numerical procedure to solve these equations. The results of the calculated performance at four different steady state conditions are provided and discussed.

### 4.2. Literature Review

Several numerical models have been developed to solve the heat and radiation transfer inside the porous material of a volumetric absorber (Kribus *et al.*, 2014) (Wang *et al.*, 2016). Most of these models are based on volume averaging to represent the absorber with a homogeneous equivalent model (HEM) with effective properties (Kribus *et al.*, 2014). This approach is macroscopic and averages the transport equations over a representative volume that is larger than the pore scale but smaller than the absorber. This is a common approach and accepted in literature for the simulation of porous media (Wu *et al.*, 2011). The key differences between the models are the assumption of either local thermal

equilibrium (LTE) or local thermal non-equilibrium (LTNE) between the solid and the fluid temperatures, as well as how the radiative transport is modeled through the porous media.

A model that implements LTE assumes that the fluid and solid temperatures are equal at each location. This requires an infinite convective heat transfer coefficient. Models like these predict much higher absorber efficiencies than those achieved in actual tests (Kribus *et al.*, 2014). The LTNE assumption therefore provides a more detailed and representative analysis of the heat transport inside the volumetric absorber, but is still simple enough for fast computation and for the use in a parametric study (Kribus *et al.*, 2013).

The radiative transport through the porous material has a direct effect on the temperature distribution through the absorber. To solve the radiative transport equation (RTE) through the depth of a porous material is no trivial matter and usually approximations such as the Rosseland-, P1- and Two-flux approximation are implemented (Modest, 2013; Vafai, 2005). Another alternative is to assume the radiation transport through the absorber as a volumetric heat source, as done by Roldán *et al.* (2014) and Achenbach *et al.* (2013). This approach is more conservative than the other, but is simpler to implement and especially for the case where the absorber has changing properties through its depth, such as this wire mesh screen concept.

Avila-Marin *et al.* (2017) developed a numerical model for a wire mesh screen absorber in order to determine a Nusselt number correlation for the convective heat transfer coefficient. A HEM with LTNE was used to calculate the temperature distribution and heat transfer coefficient for both staggered and inline mesh arrangements. The RTE made use of the P1 approximation, and the incident radiation was assumed collimated. The model was implemented and solved using CFD.

There are several phenomena that occur due to a non-homogenous flux and mass flow distributions over the absorber. These effects are not represented by the 1-D model, and need a more complex modeling approach. More detailed models solve the equations at the pore level. These models require more computational power and time and are usually implemented in CFD codes. The advantage of the 1-D model is that it has the ability to simulate complex structures such as changing properties through the depth. The specific effect of different geometrical properties for volumetric absorbers have been studied previously (Wu *et al.*, 2011b).

Figure 4.1 was adapted from Roldán *et al.* (2014) and Fend *et al.* (2004) to illustrate and explain the typical operating conditions and performance of the wire mesh absorber. The concentrated incident flux,  $I$ , is assumed to have a non-homogenous distribution (left of Figure 4.1), while the heat source through the absorber,  $E$ , attenuates depending on the geometrical properties (bottom). The solid (mesh) and fluid (air) temperature distributions (top) have a sharp increase where the finer mesh type start. The fluid exiting the absorber has the highest temperature in the middle, but the lowest flow rate due to the difference in permeability between the hot middle and cooler edges (right).

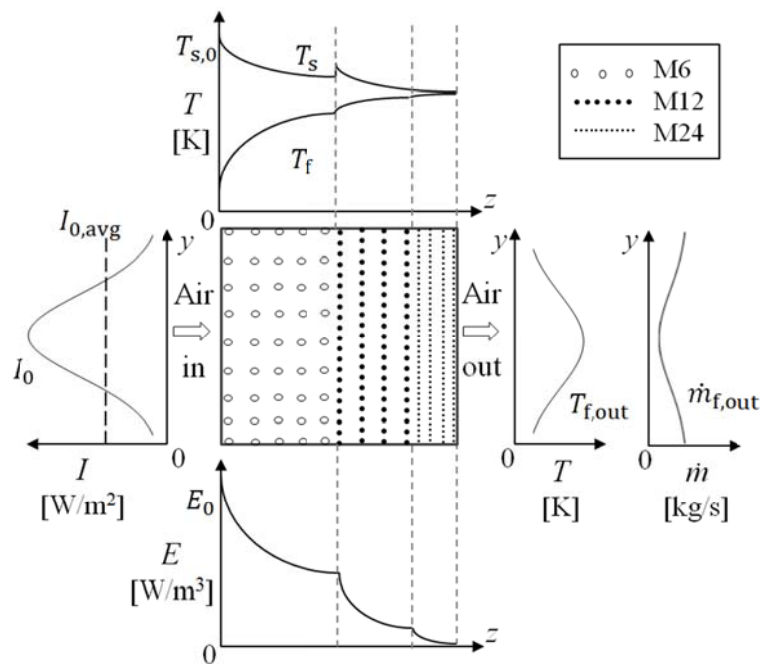


**Figure 4.1:** Schematic diagram of the absorber illustrating the incident flux, heat source, temperature and mass flow distributions on and through the absorber (adapted from (Roldán *et al.*, 2014) and (Fend *et al.*, 2004))

The results of the numerical model depend significantly on how detailed the calculations are performed, as well as how reliable the properties of the material are compared to the actual properties (Fend *et al.*, 2004). For this project as initial proof of concept, correlations obtained by previous work for parameters such as the volumetric heat transfer and extinction coefficient are used. In order to improve the model some of the important parameters should however be experimentally measured and determined. The numerical model was developed and set-up to simulate the experimental conditions.

### 4.3. Thermal Model

The 1-D approximation is used in the z-direction perpendicular to the absorber aperture, since both the flow and radiation transport occur in this direction. The absorber is divided into layers of representative volumes, with each layer containing both fluid and solid that exchange heat. The heat and radiation transfer equations are implemented and solved iteratively in Matlab R2017a.

#### 4.3.1. Governing Equations

The HEM calculates the heat transfer inside the absorber by taking into account LTNE. The thermal energy equation is solved for both the solid and the fluid separately, ignoring kinetic energy and compressibility/gas dynamics of a non-reacting flow. The complete balance equations as described by Aichmayer (2009) are for the solid:

$$k_{se} \frac{d^2 T_s}{dz^2} - h_v (T_s(z) - T_f(z)) - E_s = \rho_s c_{p,s} (1 - \varphi) \frac{dT_s}{dt} \quad (4.1)$$

And for the fluid:

$$k_{fe} \frac{d^2 T_f}{dz^2} + h_v (T_s(z) - T_f(z)) - E_f = \rho_f c_{p,f} u_f \frac{dT_f}{dz} + \rho_f c_{p,f} \varphi \frac{dT_f}{dt} \quad (4.2)$$

Where  $k_{se}$  and  $k_{fe}$  are the effective thermal conductivity of the solid and the fluid respectively,  $T_s$  and  $T_f$  are the solid and fluid temperatures respectively,  $z$  is the distance into the solid and flow direction,  $h_v$  is the volumetric heat transfer coefficient,  $E_s$  and  $E_f$  are the heat source in the solid and fluid per unit volume respectively,  $\varphi$  the porosity,  $\rho_s$  and  $\rho_f$  the density of the solid and the fluid respectively,  $c_{p,s}$  and  $c_{p,f}$  the specific heat capacity of the solid and fluid respectively,  $u_f$  the superficial fluid velocity and  $t$  the time.

The model assumes steady state conditions and air is considered as a non-participating medium in the radiation transfer through the absorber (Vafai, 2005), and has negligible thermal conductivity compared to its convection. According to Kribus *et al.* (2014) the simplified balance equations for the solid are then:

$$k_{se} \frac{d^2 T_s}{dz^2} = h_v [T_s(z) - T_f(z)] + E \quad (4.3)$$

And for the fluid:

$$\dot{M}c_p \frac{dT_f}{dz} = h_v[T_s(z) - T_f(z)] \quad (4.4)$$

The mass flux,  $\dot{M}$ , is the AMF divided by the area of the aperture and is constant through each layer due to the 1-D assumption.

The thermal conductivity through the wire mesh screens is not a simple correlation since it depends on effects such as contact between wires and screens. An effective thermal conductivity is used as proposed in Vafai (2005):

$$k_{se} = \frac{1}{3} (1 - \varphi)k_s \quad (4.5)$$

#### 4.3.2. Volumetric Heat Transfer Coefficient

The volumetric heat transfer coefficient,  $h_v$ , couples Equation (4.3) and Equation (4.4) and is a key parameter in the modeling of volumetric absorbers. This coefficient is dependent on the local wire mesh screen geometrical properties and Nusselt number as defined in Avila-Marín *et al.* (2017):

$$h_v = \frac{Nu_v k_{fe}}{d_h^2} \quad (4.6)$$

The volumetric Nusselt number correlation was obtained for a wire mesh similar to the mesh used in this project, and is used to approximate  $h_v$ . The correlation is provided for both the inline and staggered wire arrangements:

$$\text{Inline arrangement: } Nu_v = 151.9Re^{0.632}Pr^{10.49} \quad (4.7)$$

$$\text{Staggered arrangement: } Nu_v = 110.9Re^{0.494}Pr^{9.19} \quad (4.8)$$

The Reynolds number is calculated with the following:

$$Re = \frac{\rho u_f d_h}{\mu} \quad (4.9)$$

The superficial fluid velocity is calculated with:

$$u_f = \frac{\dot{m}}{\rho A_{abs} oar} \quad (4.10)$$



The inline and staggered correlations are valid for Reynolds numbers in the range of  $5 < Re < 200$  and  $10 < Re < 460$  respectively (Avila-Marín *et al.*, 2017). The effective thermal conductivity of the air,  $k_{fe}$ , is calculated by multiplying the porosity with the temperature dependent conductivity of air:

$$k_{fe} = \phi k_f \quad (4.11)$$

### 4.3.3. Property Models

Due to the large temperature variation of the air inside the absorber, temperature dependent thermal properties are used from tables in Eckert and Drake (1972). All the properties are evaluated at ambient pressure. The tables are implemented in the numerical model through the use of an air property function that uses the average air temperature between the current and the next layer in the discretized model to provide the desired property. The following properties were used:

- Specific heat capacity:  $c_p$ , J/(kg · K)
- Density:  $\rho$ , kg/m<sup>3</sup>
- Thermal conductivity:  $k$ , W/(m · K)
- Dynamic viscosity:  $\mu$ , kg/(m · s)
- Prandtl number:  $Pr$

The mentioned properties are plotted in Appendix A over the operating temperature range of 20 °C to 600 °C. These plots illustrate the effect that the temperature have on the different properties, and aid in understanding the heat transfer through the volumetric absorber. The thermal properties of the wire mesh screens are assumed to be temperature independent and constant.

## 4.4. Radiative Model

The attenuation of the solar radiation intensity is described by a volumetric heat source that attenuates exponentially based on the extinction coefficient of the absorber. This approach has been previously used and motivated by Aichmayer (2009) to approximate the radiation through a volumetric absorber material. Achenbach *et al.* (2013) used it for modeling a wire mesh absorber, and Roldán *et al.* (2014) used it in a thermal analysis of a volumetric solar absorber with a changing porosity through its depth. Although this is a conservative model, it is assumed acceptable for an initial approach to investigate the performance of the absorber.

#### 4.4.1. Governing Equation

The following equation describes the volumetric heat source, as applied by Roldán *et al.* (2014):

$$E(z) = E_0 e^{-Kz} \quad (4.12)$$

The intensity of the heat source,  $E(z)$ , at a depth  $z$  through the absorber depends on the intensity on the aperture,  $E_0$ , and the optical extinction coefficient of the absorber,  $K$ . The heat source attenuation is illustrated in Figure 4.1 for a typical absorber with a change in extinction coefficient through its depth.

The heat source intensity is correlated with the concentrated incident solar flux,  $I_0$ , by assuming all the incoming solar radiation energy is found in the heat source (Achenbach *et al.*, 2013):

$$I_0 = \int_0^{\infty} E(z) dz \quad (4.13)$$

When Equation. (4.12) is substituted in Equation. (4.13) and solved, the initial heat source intensity at the aperture is found:

$$E_0 = I_0 K \quad (4.14)$$

#### 4.4.2. Incident Flux

The incident flux level represents the effective energy available to transfer to the air. The numerical model is adapted to represent the actual experimental setup. A Gaussian-type flux distribution is therefore assumed, which is used to represent the incident flux and to calculate the power on the aperture. This is a common way to represent the incident flux distribution on a solar absorber and the same correlation is used for the PSA solar furnace and by Roldán *et al.* (2014):

$$I_0(x, y) = I_{0,\text{peak}} e^{\left(\frac{-(x^2+y^2)}{2\sigma^2}\right)} \quad (4.15)$$

The  $x$  and  $y$  coordinates discretize the aperture. In order for the function to correlate with the actual flux from the experimental setup, the peak flux,  $I_{0,\text{peak}}$ , and the variance,  $\sigma$ , of the distribution were required. The peak flux was calculated through multiplying the *DNI* with the peak concentration ratio,  $c_{\text{peak}}$ , on the center of the absorber from the concentrator:

$$I_{0,\text{peak}} = DNI c_{\text{peak}} \quad (4.16)$$

The variance was obtained through correlation with the temperature distribution over the absorber, captured by a thermal camera during the experimental testing. The complete explanation and calculation procedure for the incident flux, concentration ratio and the variance can be found in Appendix B.

The power on the absorber aperture,  $PoA$ , is calculated through integrating the Gaussian distributed flux over the aperture area:

$$PoA = \int_{-y}^y \int_{-x}^x I_0(x, y) dx dy \quad (4.17)$$

Since a 1-D model is used for the numerical simulation, an average homogenous flux is required on the front of the absorber that is representative of the total power input to the absorber. This is calculated by dividing the total incident power with the area of the aperture:

$$I_{0,\text{avg}} = \frac{PoA}{A_{\text{abs}}} \quad (4.18)$$

This calculated incident flux is treated as collimated, constant and uniform. The average concentration ratio of the medium flux concentrator can then be described by dividing the average incident flux with the  $DNI$ :

$$c_{\text{avg}} = \frac{I_{0,\text{avg}}}{DNI} \quad (4.19)$$

#### 4.4.3. Radiative Properties

The wire mesh absorber is considered a grey medium with radiative properties calculated the same as in Avila-Marín *et al.* (2017). The screen absorptivity and emissivity is for oxidized stainless steel wire mesh that was measured by Skocypec *et al.* (1989):

$$\alpha = \varepsilon = 0.85 \quad (4.20)$$

The absorption coefficient is calculated with:

$$a = \alpha \frac{4(1 - \varphi)}{\pi d} \quad (4.21)$$

The scattering coefficient:

$$\sigma_s = (1 - \alpha) \frac{4(1 - \varphi)}{\pi d} \quad (4.22)$$

The extinction coefficient is the sum of the absorption and scattering coefficients:

$$K = a + \sigma_s = \frac{8(1 - \varphi)}{\pi d} \quad (4.23)$$

## 4.5. Boundary Conditions

Kribus *et al.* (2014) noted that it is important to accurately account for the front boundary condition of the absorber, since this region has a profound influence on the performance the absorber. The sides of the absorber are considered well insulated and adiabatic.

### 4.5.1. Front Boundary

The front boundary condition is the aperture of the absorber ( $z = 0$ ) and is the balance between incident radiation, conduction to the inside of the absorber and convection to the entering fluid (Kribus *et al.*, 2014). The fraction of the frontal area of the solid that interacts with the radiation and the fluid is  $(1 - oar)$ , and is denoted by  $\varepsilon_a$ . Ambient air is sucked into the absorber. The front boundary is not optically thick although the rest of the absorber is (Kribus *et al.*, 2014). The boundary condition for the solid is then from (Kribus *et al.*, 2013):

$$\varepsilon_a a I_{0,avg} = \varepsilon_a a \sigma T_s^4(0) - k_{se} \frac{dT_s}{dz} + \varepsilon_a h_a \left( T_s(0) - \frac{T_f(0) + T_{amb}}{2} \right) \quad (4.24)$$

Wu *et al.* (2011b) found that the surface convection coefficient of the front aperture,  $h_a$ , is higher than the volumetric heat transfer coefficient inside the absorber. This is due to the large acceleration of the air into the porous absorber. A general factor of 1.6 times the inside volumetric coefficient is used for  $h_a$ , as applied by Kribus *et al.* (2014) and Natividade (2015). The corresponding boundary condition for the fluid from Kribus *et al.* (2013) is then:

$$\dot{M} c_p (T_f(0) - T_{in}) = \varepsilon_a h_a \left( T_s(0) - \frac{T_f(0) + T_{amb}}{2} \right) \quad (4.25)$$

#### 4.5.2. Back Boundary

The back of the absorber is assumed to be perfectly insulated and a perfect diffuse reflector (Kribus *et al.*, 2013), therefore there are no losses from the back of the absorber and no temperature gradient for both the solid and the fluid at this surface.

### 4.6. Absorber Performance

The performance of the absorber is evaluated with its outlet air temperature and corresponding thermal efficiency at a certain incident flux level and AMF. The thermal efficiency of the absorber is the ratio of the enthalpy rise of the fluid,  $\dot{Q}_{out}$ , to the total incident power on the absorber aperture:

$$\eta_{th} = \frac{\dot{Q}_{out}}{PoA} = \frac{\dot{m} \int_{T_{f,in}}^{T_{f,out}} c_p(T) dT}{I_{0,avg} A_{abs}} \quad (4.26)$$

The efficiency is calculated for steady state conditions with constant parameters such as AMF and DNI.

### 4.7. Numerical Procedure

In order to solve the differential equations the absorber is discretized and the derivatives are replaced with finite difference approximations. The absorber is divided into a finite number of layers as illustrated in Figure 4.2, for which each of the equations is solved. An explicit scheme is used since steady state conditions are considered and therefore no flow instabilities expected. This is also an easier scheme to implement in Matlab with less computational power required. It is assumed that the fluid does not change in direction through the absorber, and therefore the directional scheme can be used. This however does not allow taking thermal dispersion of the air behind the mesh layers into account. In this approach each single screen was considered a step,  $\Delta z$ , and hence the equations solved for it.

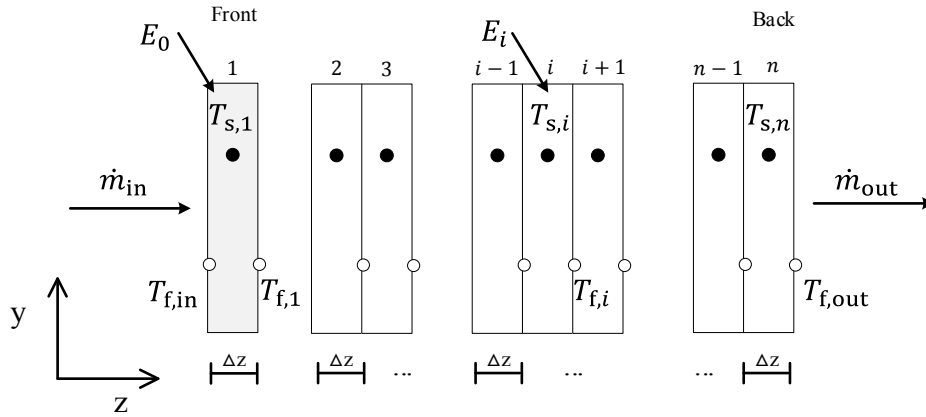


**Figure 4.2:** Discretized absorber model with annotations

For the solid phase a central differencing scheme is used, thus the temperature of each layer is influenced by the two adjacent layers. The second order central differencing scheme is given by:

$$\frac{d^2 T_s}{dz^2} = \frac{T_{s,i-1} - 2T_{s,i} + T_{s,i+1}}{\Delta z^2} \quad (4.27)$$

The first order central differencing scheme is:

$$\frac{dT_s}{dz} = \frac{T_{s,i+1} - T_{s,i-1}}{2\Delta z} \quad (4.28)$$

For the fluid, a first order upwind differencing scheme is used and therefore the temperature at each layer being only dependent on the upstream temperature:

$$\frac{dT_f}{dz} = \frac{T_{f,i} - T_{f,i-1}}{\Delta z} \quad (4.29)$$

The same schemes was applied by Natividade (2015). Through substituting these finite difference approximations, the following discretized equations can be written for each layer,  $i$ . For the front boundary layer of the solid:

$$(2\Delta z \varepsilon_a a \sigma) T_{s,1}^4 + (2\Delta z \varepsilon_a h_a) T_{s,1} - (k_{se}) T_{s,2} - (\Delta z \varepsilon_a h_a) T_{f,1} - (\Delta z \varepsilon_a h_a) T_{amb} - (2\Delta z \varepsilon_a a) E_0 = 0 \quad (4.30)$$

The equation for the fluid's front boundary layer is:

$$\left( \dot{M} c_p + \frac{1}{2} \varepsilon_a h_a \right) T_{f,1} - \left( \dot{M} c_p - \frac{1}{2} \varepsilon_a h_a \right) T_{amb} - (\varepsilon_a h_a) T_{s,1} = 0 \quad (4.31)$$

For a solid central layer:

$$(k_{se})T_{s,i-1} - (2k_{se} + \Delta z^2 h_v)T_{s,i} + (k_{se})T_{s,i+1} + (\Delta z^2 h_v)T_{f,i} - \Delta z^2 E_i = 0 \quad (4.32)$$

The equation for a fluid central layer is:

$$(\dot{M}c_p)T_{f,i-1} - (\dot{M}c_p + \Delta zh_v)T_{f,i} + (\Delta zh_v)T_{s,i} = 0 \quad (4.33)$$

The geometrical properties of the absorber at each position,  $i$ , depend on the predefined configuration, and are calculated for each step through the absorber. The solid and fluid temperatures at each layer are obtained through iteratively solving both equations simultaneously in Matlab, taking into account temperature dependent air properties. The flowchart shown in Figure 4.3 illustrates the procedure for the calculations in the model. The convergence condition is reached when the relative variation in temperature of the grid points between consecutive iterations is smaller than  $10^{-4}$ .

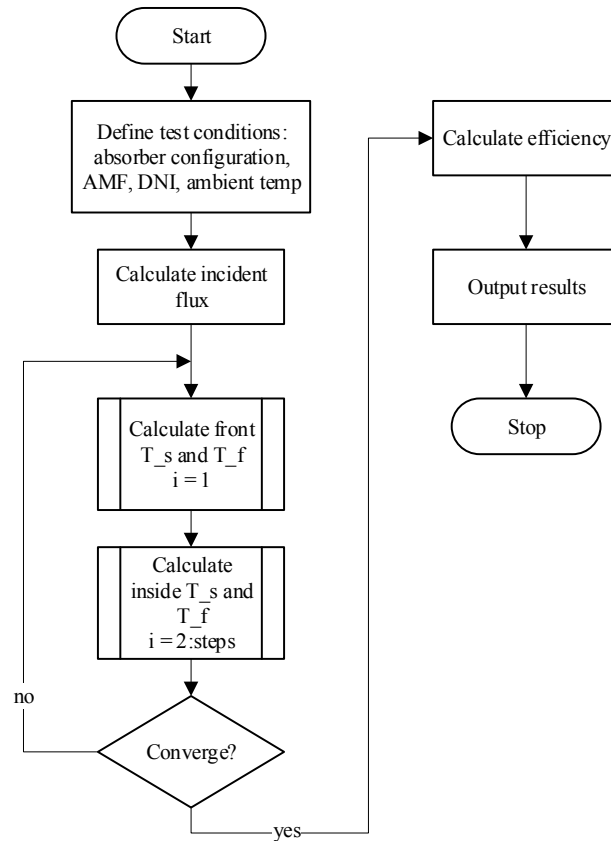


**Figure 4.3:** Flowchart for the calculation procedure of the numerical model

## 4.8. Modeling Results and Discussion

An (5/5/5) absorber configuration is used to present and discuss the results calculated with the numerical model. The reference parameters for the simulations are provided in Table 4.1. The absorber has a gradual porosity going from 82.3 % to 70.4 % and is 18.2 mm thick. The other geometrical details of the screens used were provided in Chapter 3.

**Table 4.1:** Reference parameters for simulation

Parameter	Symbol	Unit	Value
Ambient air temperature	$T_{amb}$	°C	22
DNI	$DNI$	W/m <sup>2</sup>	800
Solid thermal conductivity	$k_s$	W/(m·K)	13*
Absorptance	$\alpha$	-	0.85
Aperture area of absorber	$A_{abs}$	m <sup>2</sup>	0.0121

\* Stainless steel 316

### 4.8.1. Incident Flux Distribution

The Gaussian flux distribution over the aperture of the absorber is shown in Figure 4.4 (a). The distribution is at a DNI value of 800 W/m<sup>2</sup>, which produces a peak flux of 92.4 kW/m<sup>2</sup> and an average flux of 56.9 kW/m<sup>2</sup> on the absorber aperture, as shown in Figure 4.4 (b). The total incident power is 689 W.

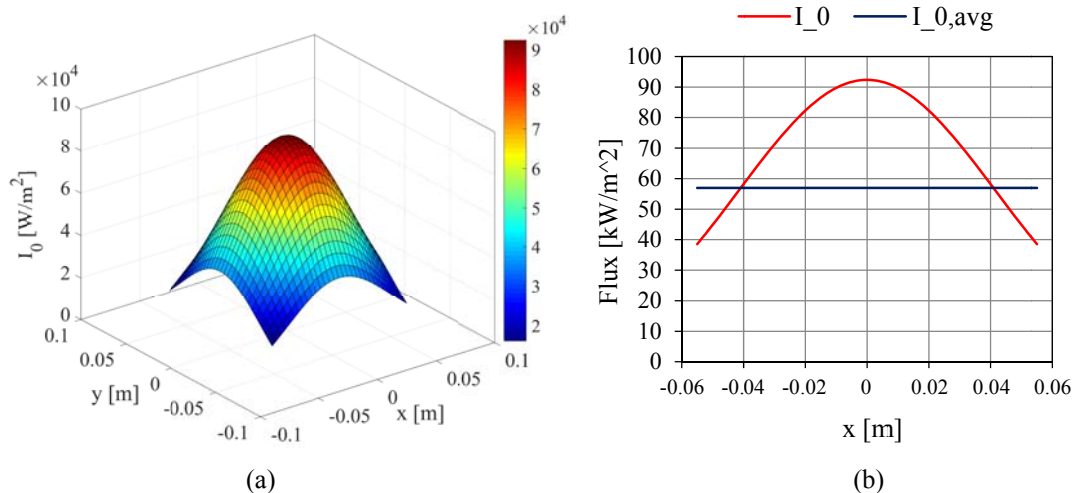


**Figure 4.4:** Flux distribution over the absorber aperture with DNI = 800 W/m<sup>2</sup>: (a) 3-D Gaussian flux distribution for, (b) 2-D Gaussian flux distribution with average flux value



#### 4.8.2. Steady State Performance

The steady state performance at four different AMFs was considered. These specific four flow rates were used since they correspond to the ones used during the experimental testing. The AMF, corresponding mass flux and Reynolds numbers from the front to the back of the absorber are provided in Table 4.2.

**Table 4.2:** Different AMFs, mass fluxes and calculated Reynolds numbers for the simulation

No.	AMF kg/s	Mass flux kg/(m <sup>2</sup> ·s)	Reynolds number (front to back of abs)
1.	0.0015	0.124	45 to 8
2.	0.0013	0.107	39 to 7
3.	0.0010	0.083	30 to 5
4.	0.0008	0.066	24 to 4

The temperature profiles through the absorber for the solid and the fluid at the highest and lowest flow rates (AMF 1 and 4 respectively) are shown in Figure 4.5.

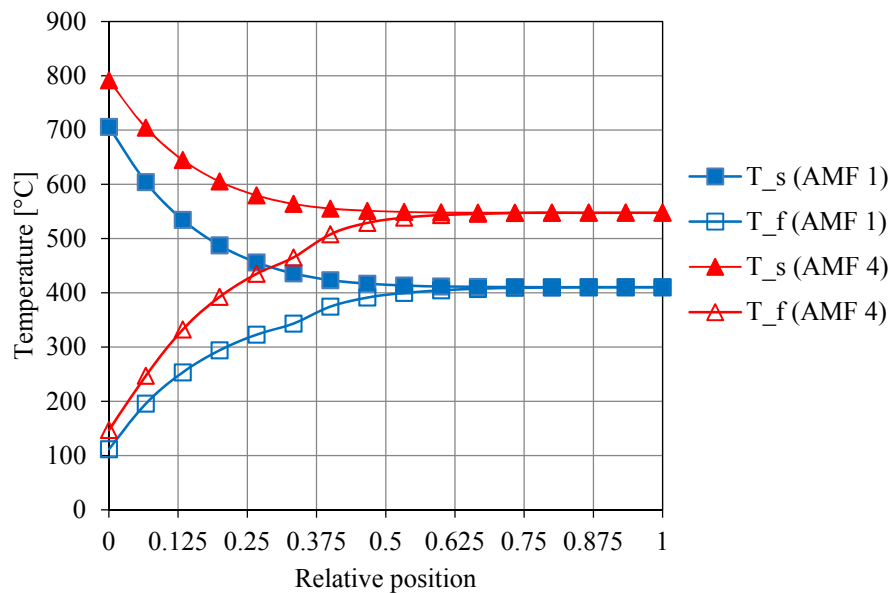


**Figure 4.5:** Temperature distribution of the solid and the fluid through the absorber at two different flow rates

It is clear from Figure 4.5 that a decrease in flow rate increases the outlet temperature. The outlet temperature increases from 406 °C at AMF 1, to 544 °C at AMF 4. At a lower flow rate there is less cooling effect from the air and the solid obtain a higher temperature, which in turn increases the air outlet temperature. The figure also shows that the highest temperature occurs at the front, and therefore the aspired volumetric effect is not reached.

The lower effective thermal conductivity of the M6 screens causes a steeper temperature profile in the front region. This causes a higher front temperature since heat removal through conduction to the inside is reduced. The M12 screen start at relative position 0.375, where a slight increase can be observed in the slope of the fluid temperature profile. This demonstrates that the higher specific surface area increases the heat transfer to the fluid. The temperature difference between the solid and fluid is too low to clearly see the effect of the M24 screens.

The thermal performance of the (5/5/5) absorber is plotted in Figure 4.6. The efficiency and outlet air temperature is plotted over the ratio of the power on the aperture divided by the air mass flow rate ( $PoA/AMF$ ). This is a common way to illustrate the performance of a volumetric receiver, since different receivers operating under different conditions can be compared. For this plot the DNI, and therefore  $PoA$ , was kept constant while the AMF was changed.

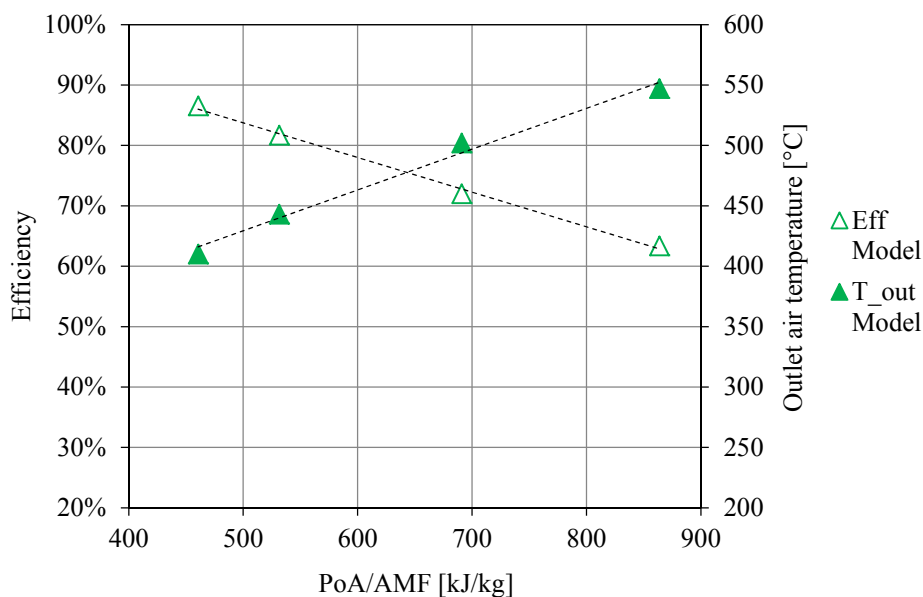


**Figure 4.6:** Model performance plot for the (5/5/5) absorber at four different AMFs and average flux of 56.9 kW/m<sup>2</sup>

At a higher AMF the air has more capacity to absorb the thermal energy through convection and therefore a higher efficiency is achieved. The Reynolds number is also higher, which results in a better heat transfer coefficient. The lower front temperature at the higher AMF reduces the thermal losses. At the lower AMF the higher front temperature increases the thermal losses and therefore decreases the efficiency. In Figure 4.7 the radiation, convection and reflection losses with the efficiency are plotted over outlet air temperature. The radiation losses from the front significantly increase as the outlet air temperature increase, due to the accompanying higher front temperature.

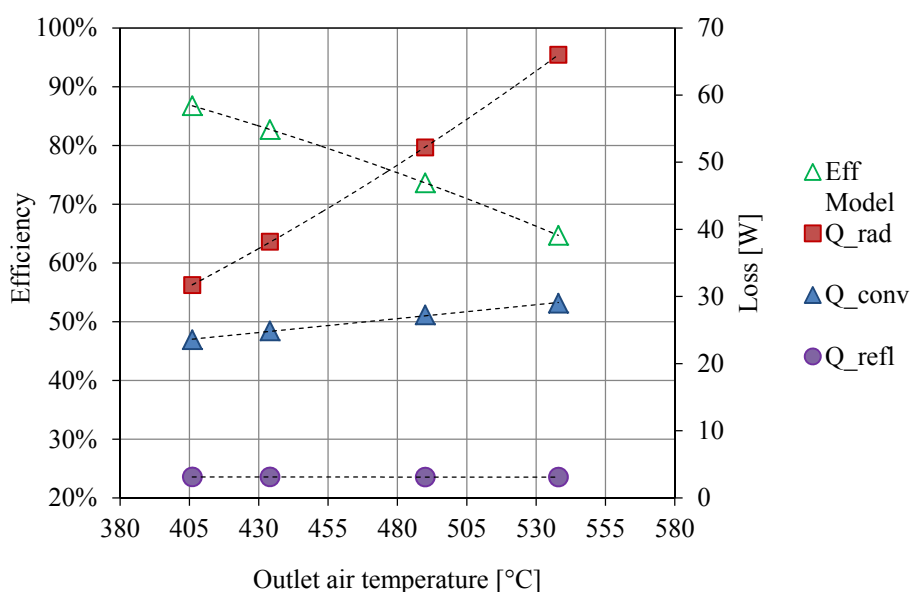


**Figure 4.7:** Efficiency and thermal losses from the front of the absorber plotted against the outlet air temperature from the numerical model

A higher incident flux value produces a higher solid front temperature, which results in a higher outlet air temperature. The higher front temperature however increases the thermal losses as well as discussed, and therefore a higher AMF is required to enhance the heat removal from the front. The absorber is clearly more efficient at the higher flow rates, however due to the low concentration ratio possible from the concentrator as well as the flow rate capabilities of the setup, the low AMFs were required to reach a higher outlet air temperature.

## 4.9. Conclusion

In this chapter the numerical model of the heat and radiation transfer inside the absorber material was discussed. With a 1-D approach a HEM with LTNE was used to calculate the temperature distribution of the solid and the fluid through the depth of the absorber. The radiative flux was simulated with a volumetric heat source that has a Gaussian distribution on the aperture of the absorber. The thermal performance of the (5/5/5) absorber configuration was used as sample results. The effect of the AMF was investigated, and showed that a lower AMF increase the outlet air temperature, but also lower the thermal efficiency. The model therefore provides a good insight into the expected performance of the experimental setup, and established what measurements are required on the experimental setup.

# Chapter 5

## Experimental Apparatus and Procedure

### 5.1. Introduction

A small scale central receiver test setup was used to empirically validate the wire mesh absorber concept under different operating conditions. The setup is located on the solar rooftop lab and makes use of the DNI as input. The setup had been previously built and used by Kretzschmar (2014). For this work the tower and its components were redesigned to install the absorber concept and to overcome previous limitations of the test setup. The objectives of the tests are the following:

1. Measure the thermal performance of the wire mesh screen absorber under different AMFs and incident flux values.
2. Compare the performance of different absorber configurations.
3. Collect data to validate the numerical model.
4. Investigate the performance and durability of the absorber material at high temperatures and flux concentrations.
5. Investigate the influence of uncontrolled ambient conditions on the performance of the absorber, such as DNI and wind.

The pressure drop over the absorber was assumed insignificant for this work since it is very low through the screens and only a single absorber module was tested. A quick validation measurement on the setup supported this assumption.

The chapter starts with a clear description of the tower that has been designed and the concentrator setup that is used. The thermal evaluation with the different measurements taken during testing is discussed, where after the experimental procedure is explained. Both the equipment calibration and uncertainty analysis are important considerations and are discussed before a conclusion is made.

## 5.2. Test Setup

The test setup consists of a small scale tower and a medium flux concentrator, both of which are discussed below.

### 5.2.1. Small Scale Test Tower

The tower and its components were redesigned from the previous setup to allow for the testing of the absorber concept developed in this project. The final design and assembly drawing can be found in Appendix C. The tower is 1 meter high and the receiver look down at the field at an angle of  $39^\circ$  with the global vertical axis, based on the simulation and design of Kretzschmar (2014) of the solar field. The manufactured components of the tower can be seen in Figure 5.1 (a), and in (b) the installed tower on the concentrator setup are shown while in operation.

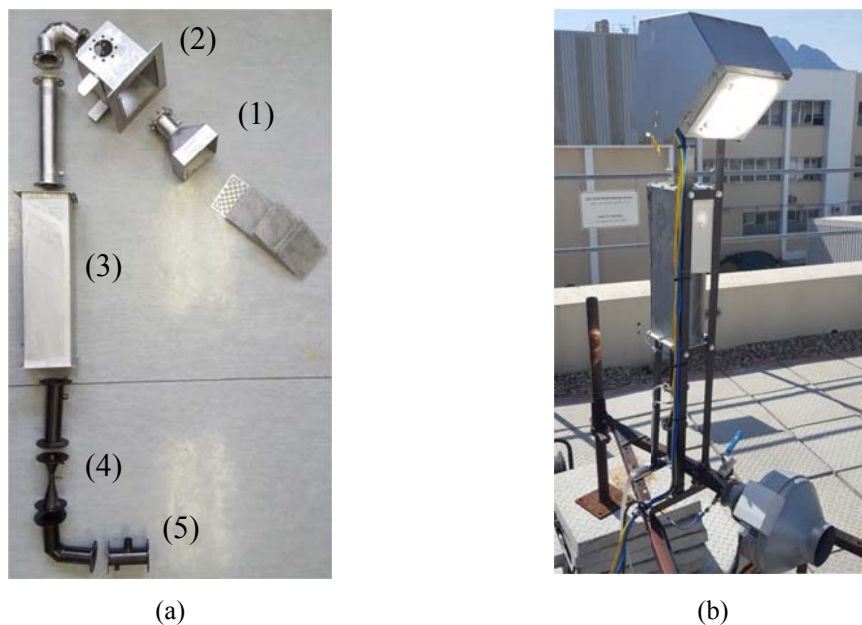


**Figure 5.1:** Small scale test tower: (a) exploded view of the components of the tower, (b) tower installed on the concentrator with the focus on the receiver

Figure 5.1 (a) illustrates the absorber cup (1) that is mounted inside the receiver housing (2), followed by a small rock bed heat exchanger (3). A venturi flow meter (4) is used to measure the AMF and a variable speed axial fan connected at (5) provides the required airflow through the setup. The annotated components in Figure 5.1 (a) are briefly discussed:

**(1) Absorber and cup:** These parts were thoroughly discussed in Chapter 3.

**(2) Receiver housing:** The absorber cup is placed inside a square housing which aims to represent the structure and environment for the cup as if it is operating in a large receiver. The housing is made from 1.2 mm thick stainless steel AISI 316 sheet metal, and is well insulated on the outside with a double layer of ceramic fiber boards to prevent heat loss to the environment. The faceplate protects the insulation and thermocouples from spillage from the concentrator. The housing also allows the future installation of an air return loop (hole in side shown in Figure 5.2 (a)). There is a gap of  $\pm 3$  mm between the sides of the cup and the housing where the return air can exit to the front. An additional steel hood was also placed over the receiver housing with insulation once all the thermocouples were installed and the absorber was placed into focus. This further insulated the receiver and helped prevent losses through the sides and back.



(a)



(b)

**Figure 5.2:** Receiver housing (a) manufactured housing, (b) insulated housing with absorber installed on tower

**(3) Rock bed heat exchanger:** One of the main design challenges with using an OVAR is the fact that the fan is located on the hot side of the receiver, since ambient air is sucked through the absorber and heated up. The fan has clear maximum inlet air temperature limitations and therefore the heat needs to be extracted from the air before it enters the fan. Although the performance of the rock bed is outside the scope of this project, it was a simple and effective way to lower the air temperature. It should be noted that this rock bed was used as heat exchanger, and not as a thermal storage. As such the rock bed was not insulated on the outside. The size of the heat exchanger is 100 mm x 100 mm x 400 mm, with an average particle size as shown in Figure 5.3. The rock bed sufficiently removed the heat from the absorber outlet air throughout the tests.





**Figure 5.3:** Sample of the rocks used in the rock bed heat exchanger

## 5.2.2. Medium Flux Concentrator

The concentrator provides the incident flux on the receiver, and is shown in Figure 5.4. The mirrors of the setup was cleaned and refocused before the tests were performed to enhance its concentrating capabilities.



**Figure 5.4.** Medium flux concentrator with the tower installed for testing

The medium flux concentrator makes use of 152 small mirrors in a heliostat field layout of 9 rows of 17 mirrors each. The mirrors are normal flat mirrors and each one is a 100 mm size square. The layout was selected by Kretzschmar (2014) based on the results and optimization of a ray-tracing analysis performed. The setup performs azimuth tracking by moving on a circular guide rail around a central pivoting point behind the tower. A screw mechanism on this pivot point implements the zenith tracking. However, the range of these two components limited the testing to 1.5 hours before and after solar noon every day. Tracking is



performed by pointing the center mirror of the back row to a target point just below the receiver. The offset between this mirror and the point indicates the required movement of the setup to keep the focus point of the rest of the field on the receiver. The setup could maintain accurate tracking and its position was adjusted every 2 minutes during testing.

### 5.3. Thermal Evaluation

The measurements that were made on the experimental setup aimed to allow the thermal performance of each absorber configuration to be evaluated and calculated. The efficiency was calculated using the same formula as was used for the numerical model and is provided in Equation (4.26). The required measurements were the incident flux, absorber and air temperatures, and AMF. The equipment used for each of these measurements is described in the following section. All the equipment was connected to a data logger, which collected and displayed the measurements on a laptop in 3 second intervals.

#### 5.3.1. Temperature

With the use of new type K and T thermocouples temperature measurements were made throughout the tower setup. The location of each thermocouple in and around the absorber cup is illustrated in Figure 5.5.

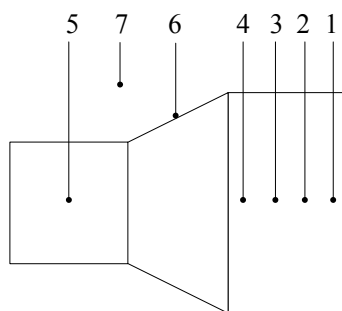


**Figure 5.5:** Thermocouple layout in and around the absorber and cup

Thermocouples 1 to 4 measured the temperature distribution through the wire mesh screens. These thermocouples were inserted through small holes drilled through the side of the cup and housing. The thermocouples could not be permanently fixed or welded to the screens since the setup had to allow testing of different absorbers and therefore the thermocouples had to be removed for the absorber to be taken out and replaced each time.

The thermocouples inside the absorber were positioned to take measurements at the center of the absorber at the highest flux and therefore temperature values, and were placed between the different mesh screen types. The front thermocouple was shielded from direct flux as it was placed behind the first two mesh screens. Good thermal contact was ensured by compressing the thermocouples in between the screens. The cup's material temperature as well as the air surrounding the cup inside the housing was also measured with thermocouples 6 and 7. The outlet air was measured in the throat of the cup where the air exiting the back of the absorber is mixed. Air temperature measurements through the absorber were not feasible.

A Fluke Ti400 thermal camera was used to capture infrared images of the aperture of the absorber while it was in the concentrated flux to investigate the temperature distribution. The images showed a clear non-homogenous temperature and therefore flux distribution over the absorber surface, with the peak values in the center of the absorber. The temperature readings from the images were used to characterize the Gaussian distribution function used for the incident flux. These readings were also compared to the front thermocouple measurements. However, since the emissivity of the wire mesh absorber can only be estimated, the images are mostly used for qualitative temperature distribution. The thermal camera is a handheld camera and was not connected to the data logger.

### 5.3.2. Air Mass Flow Rate

The AMF through the absorber was measured with a venturi flow meter placed after the rock bed heat exchanger and before the fan inlet. The venturi was designed and manufactured by Kretzschmar (2014) based on the standards provided in Figliola (2006). A pressure transducer constantly measured the pressure drop over the venturi and gave a voltage output to the data logger. The venturi was calibrated before the experimental tests and the calibration is discussed in Appendix D. The air temperature was measured before the venturi inlet to take into account the change in air density during testing as the temperature of the rock bed outlet increased. A ball-valve was also inserted in an in line T-piece before the fan. This allowed additional cold ambient air to be bleed in and further lower the air temperature entering the fan. The valve was used as an additional AMF controller as well.

### 5.3.3. Incident Flux

The peak incident flux was measured with two different flux sensors to validate the measurements. The two sensors (Hukseflux SBG01 and Vatell TG-1000) were installed in the place of the absorber prior to testing to measure the peak flux in the center of the focal spot. This measured peak flux values were used to further characterize the Gaussian distribution function to represent the incident flux. The detailed calculations of this can be found in Appendix B.

### 5.3.4. Weather

The weather data for each day of testing were obtained from the so-called Sonbesie Weather Station of the Engineering Faculty of Stellenbosch University. The minutely averaged data of DNI, air temperature, relative humidity, wind speed, barometric pressure as well as several other measurements were downloaded. A sample of this data are provided in Appendix E as part of the sample calculations. An additional thermocouple was used to measure ambient air temperature at the experimental setup and to confirm the measurement from the weather station.

## 5.4. Experimental Procedure

The experiments were conducted with the variables and procedure out-lined in this section.

### 5.4.1. Variables

It is important to distinguish between the controlled and uncontrolled variables in the tests. Since the experiments were conducted outside, the weather conditions were mainly the uncontrolled parameters, as stated in Table 5.1. Testing was therefore only performed on cloudless sunny days to ensure that the DNI and incident flux values were fairly constant over the test period.

**Table 5.1:** Controlled and uncontrolled variables of the experimental setup

<b>Controlled</b>	<b>Uncontrolled</b>
<ul style="list-style-type: none"> <li>• Absorber configuration</li> <li>• AMF</li> </ul>	<ul style="list-style-type: none"> <li>• Weather conditions such as DNI, ambient temperature and wind speed</li> </ul>

The tests included the following configurations, as mentioned before: (6/10/10), (5/5/5), (6/10/0), (10/0/0), (6/4/2). Each absorber configuration was typically tested at all or most of the different AMFs shown in Table 5.2. Flow rate 1 and 4 was at the maximum and minimum capabilities of the axial fan used. An AMF range is provided to account for the small difference between tests.

**Table 5.2:** Different AMFs used for experimentally testing the absorber at

No.	AMF range, kg/s
1.	0.0014 – 0.0015
2.	0.0011 – 0.0013
3.	0.0010 – 0.0010
4.	0.0008

The calculated peak and average flux values, as well as total power on the aperture is provided in Table 5.3 for different DNI values.

**Table 5.3:** Incident flux and power on the absorber at different DNI values

DNI, W/m <sup>2</sup>	Peak Flux, kW/m <sup>2</sup>	Average Flux, kW/m <sup>2</sup>	PoA, W
950	110	67.8	821
850	98.1	60.7	734
750	86.6	53.6	648

#### 5.4.2. Quasi-steady State

Since the test setup was located outside and experienced continuous fluctuations in DNI and wind conditions over a test period, perfect steady state conditions could not be reached. A conservative approach was therefore used by defining a quasi-steady state condition for each AMF (Télez, 2003). This condition was reached when the change in outlet air temperature was less than 1 % while the change in front temperature was less than 5 % over a period of 3 to 4 minutes. The temperature and flow rate measurements, as well as weather conditions were averaged over this period to calculate the thermal performance. Fend *et al.* (2004) performed similar experiments for volumetric absorbers and used 10 minute averages. This receiver was however located indoors and received the incident

flux from the heliostat field on the outside. The receiver was therefore more protected from the influence of ambient conditions, which allowed longer time averages to be used.

### 5.4.3. Operating Procedure

The experimental operating procedure for each absorber configuration was as follows:

1. Assemble the desired absorber configuration by stacking a certain number of each of the screen types in the absorber.
2. Place the absorber inside the cup and receiver housing and place the thermocouples at their positions.
3. Start taking measurements with the data logger to obtain initial zero readings.
4. Start the fan to create a flow rate through the absorber.
5. Move the setup into focus.
6. Adjust the tracking based on the position of the tracking mirror.
7. Monitor the temperature readings and if there are no significant changes for a certain amount of time, lower the AMF. Also take into account the fluctuations in ambient weather conditions.
8. Repeat steps 6 and 7 for each AMF to be tested at.
9. Move the setup out of focus and let the absorber cool down by keeping the AMF on.
10. Export the measured data to an Excel file for the post processing.

## 5.5. Calibration and Uncertainty

The uncertainty analysis aims to estimate the accuracy of the results obtained during the experimental tests. The energy transferred to the air as well as the incident power on the aperture of the absorber are the two main results considered in the analysis. In order to determine the uncertainty of the results, all the uncertainties for the different instruments used were combined using the root-sum-squares (RSS) method (Coleman, 2006). The formula applied to calculate the energy transferred to the air is repeated here to show it as a function of the measured property used to calculate it:

$$\dot{Q}_{\text{out}} = \dot{V}_{\text{venturi}}(\Delta p)\rho_{\text{air}}(T)c_p(T_{\text{avg}})[T_{\text{out}} - T_{\text{amb}}] \quad (5.1)$$

The AMF is the product between the volumetric flow rate,  $\dot{V}_{\text{venturi}}$ , and the density of the air,  $\rho_{\text{air}}$ . The volumetric flow rate is measured with a differential pressure transducer connected to the venturi flow meter. The pressure transducer itself has an accuracy of  $\pm 0.1\%$  of the set span (2500 Pa), hence  $\pm 2.5$  Pa (Endress+Hauser, 2000). The pressure transducer was calibrated against a Betz micro-manometer which has a reading accuracy of  $\pm 0.04\%$  of the full scale range of 5000 Pa, which is  $\pm 2$  Pa (ACIN, 2016). All testing and calibration were done within this limit. The pressure transducer produces a voltage output to the data logger (Keysight-34901A) that has a range error of  $\pm 0.0005\%$  and a reading error of  $\pm 0.0035\%$  in the measured range of 10 V. This results in a  $\pm 0.005$  V uncertainty and corresponds to  $\pm 1.6$  Pa pressure reading error. The data logger reading accuracy is dependent on the actual measurement and is a maximum of  $\pm 0.1$  Pa at the highest pressure drop measurement of 400 Pa. Therefore the combined uncertainty of the measured pressure drop is:

$$U_{\Delta p} = \sqrt{2.5^2 + 2^2 + 1.6^2 + 0.1^2} = \pm 3.58 \text{ Pa.}$$

The venturi flow meter calibration is thoroughly discussed in Appendix D. The discharge coefficient was determined for the venturi and there was a  $\pm 0.16\%$  deviation between the calculated and measured flow rate over the calibrated range, which correspond to  $U_{\dot{V}} = \pm 0.557 \times 10^{-6} \text{ m}^3/\text{s}$  at the lowest AMF.

The density as well as the specific heat capacity of the air was obtained by using temperature dependent property tables at ambient pressure from Eckert and Drake (1972). The uncertainty of these values was considered negligible compared to other influences.

The temperature measurement of the outlet air was made with a type K thermocouple, which have a systematic error of  $\pm 2.2$  °C or 0.75 % depending on whichever is the greatest (Figliola, 2006). The data logger has an accuracy of  $\pm 1$  °C for a type K thermocouple within the range of -100 °C to 1200 °C. The combined uncertainty of the maximum outlet temperature measurement at 500 °C is therefore  $U_{T_{\text{out}}} = \sqrt{3.75^2 + 1^2} = \pm 3.9$  °C

The ambient temperature measurement was made at the weather station with a CS215 temperature and relative humidity probe (Campbell Scientific, 2009). This temperature measurement has an accuracy  $U_{T_{\text{amb}}}$  of  $\pm 0.4$  °C between 5 °C to 40 °C.

The total uncertainty of the energy transferred to the air at each steady state was AMF and temperature dependent, and could be calculated with the following general uncertainty expression for this particular case (Coleman & Steele, 1999):

$$\left(\frac{U_{\dot{Q}_{out}}}{\dot{Q}_{out}}\right)^2 = \left(\frac{U_{\Delta p}}{\Delta p}\right)^2 + \left(\frac{U_{\dot{V}}}{\dot{V}_{venturi}}\right)^2 + \left(\frac{U_{T_{out}}}{T_{out}}\right)^2 + \left(\frac{U_{T_{amb}}}{T_{amb}}\right)^2 \quad (5.2)$$

The uncertainty at the condition of minimum flow rate and maximum outlet temperature would illustrate the worst case scenario and is used here as reference:

$$\begin{aligned} \left(\frac{U_{\dot{Q}_{out}}}{\dot{Q}_{out}}\right) &= \sqrt{\left(\frac{3.58 \text{ Pa}}{85 \text{ Pa}}\right)^2 + \left(\frac{0.557 \times 10^{-6} \text{ m}^3/\text{s}}{8.11 \times 10^{-4} \text{ m}^3/\text{s}}\right)^2 + \left(\frac{3.9 \text{ }^\circ\text{C}}{500 \text{ }^\circ\text{C}}\right)^2 + \left(\frac{0.4 \text{ }^\circ\text{C}}{25 \text{ }^\circ\text{C}}\right)^2} \\ &= 0.0457 \text{ or } 4.6 \% \end{aligned} \quad (5.3)$$

The steady state incident power on the absorber was calculated through integrating the Gaussian flux distribution function over the absorber aperture. The peak flux was measured with a flux sensor. The Vatell TG-1000 flux sensor has a calibrated accuracy of  $\pm 3\%$  at its full scale of  $50 \text{ kW/m}^2$ , which result in an uncertainty of  $\pm 1.5 \text{ kW/m}^2$ . A second flux sensor was used to validate the measurements of the first sensor. The Hukseflux SBG01 sensor has a calibrated uncertainty of  $\pm 6.3\%$  at its full range of  $10 \text{ kW/m}^2$ . The measured values of the two different sensors were within a range of  $2.2\%$  of each other, with the slight difference due to different ambient conditions between the measurements. The DNI measurement from the weather station is done with a Kipp and Zonen CHP1 pyrheliometer that has a  $2\%$  uncertainty (Kipp & Zonen, 2008).

In order to validate the calculated incident flux, the calculated average concentration ratio was compared to the concentration ratio determined in a previous project that used the same concentrator (Roos, 2016) and which used a water cooled calorimeter designed by Kretzschmar *et al.* (2014). This device was unfortunately no longer available at the time when this project was conducted. However, the combined use of the flux sensors, thermal camera and Gaussian distribution function produced a calculated average concentration ratio of 71.2, which was in excellent agreement to the one determined with the use of the calorimeter of 71.4.

Since the whole test setup was located outside, the changing ambient conditions induced quite a large uncertainty. This was accounted for through using the DNI and ambient air temperature at the exact time of each of the quasi-steady state conditions when calculating the absorber performance, as well as by repeating the same tests. The plot of the minutely averaged DNI and ambient air temperature measurements during a typical day of testing is shown in Figure 5.6. The average DNI over the time period shown is  $775 \pm 7.6 \text{ W/m}^2$ , with the average ambient temperature being  $22 \pm 0.4 \text{ }^\circ\text{C}$ .

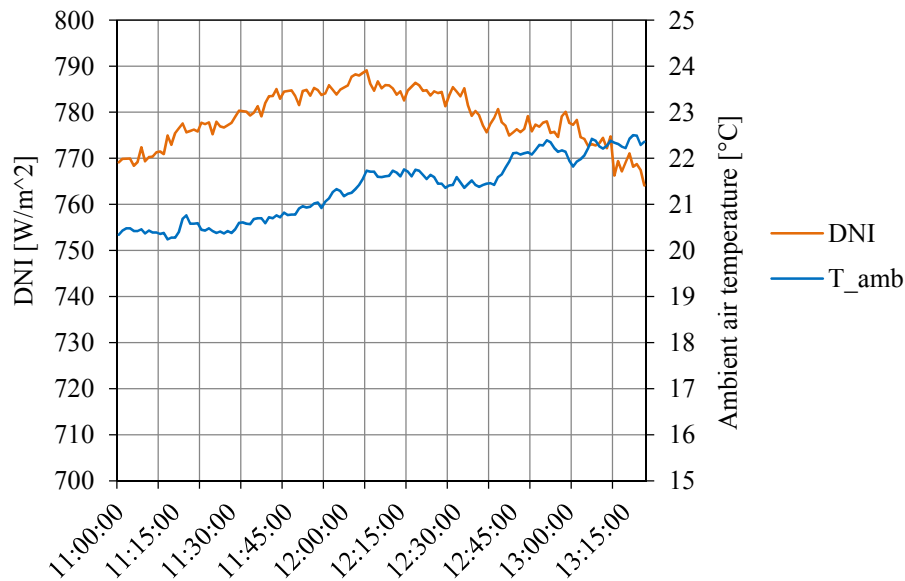


**Figure 5.6:** DNI and ambient air temperature variation over a test period for 06/06/2017

The fact that the complete experimental setup is outside allows a much more realistic and representative performance of the experiments, since this is how a large receiver will operate. The testing of the absorber was also completely dependent on the weather conditions and could only be conducted on clear sunny days with relatively low wind speeds. This limited the amount of testing that could be performed.

## 5.6. Conclusion

The experimental setup was used to empirically validate the absorber concept as well as the numerical results. The small scale tower was designed to allow the testing of different absorbers and configurations and to represent the operating conditions for the absorber of a large receiver. The thermal evaluation of the concept is aimed to answer the question of the actual performance of the absorber under different conditions. An uncertainty analysis conducted proved that there is a low uncertainty in the measured thermal power gained by the air, however the uncertainty of the incident power from the concentrator is dependent on the accuracy of the correlation used for the flux distribution. The results for the tests are provided in the next chapter with a discussion and other significant observations made during testing.



# Chapter 6

## Results and Discussion

### 6.1. Introduction

The experimental tests took place between 19 April 2017 and 6 June 2017, after which weather conditions such as insufficient DNI and strong winds prevented further testing. During this period, 13 tests were conducted with each test running on average 2.5 hours between 11:00 to 14:00, which are in total 32 hours of tests.

The chapter layout starts with the measured and calculated thermal performance for the different absorber configurations. The agreement and discrepancies between the experimental and modeling results are then investigated, followed by observations made during the testing. A discussion of the overall results and conclusion is added at the end.

### 6.2. Experimental Results

The highest efficiency was reached with the (6/4/2) absorber configuration, and therefore it is used to provide sample results to be discussed in detail. The results of the rest of the absorber configurations tested are then summarized in a table and figure at the end. A sample calculation is provided in Appendix E.

#### 6.2.1. Temperature and Flow Rate Measurements

The plot of the measured temperatures and five different AMFs of the (6/4/2) absorber are shown in Figure 6.1. The DNI during testing was  $775 \pm 8 \text{ W/m}^2$ , which produced a peak flux of  $89.5 \text{ kW/m}^2$  and an average flux of  $55.3 \text{ kW/m}^2$  on the aperture of the absorber. The total incident power was 669 W. The ambient temperature was  $22 \text{ }^\circ\text{C}$  and wind conditions fairly constant and low at 3.1 m/s.

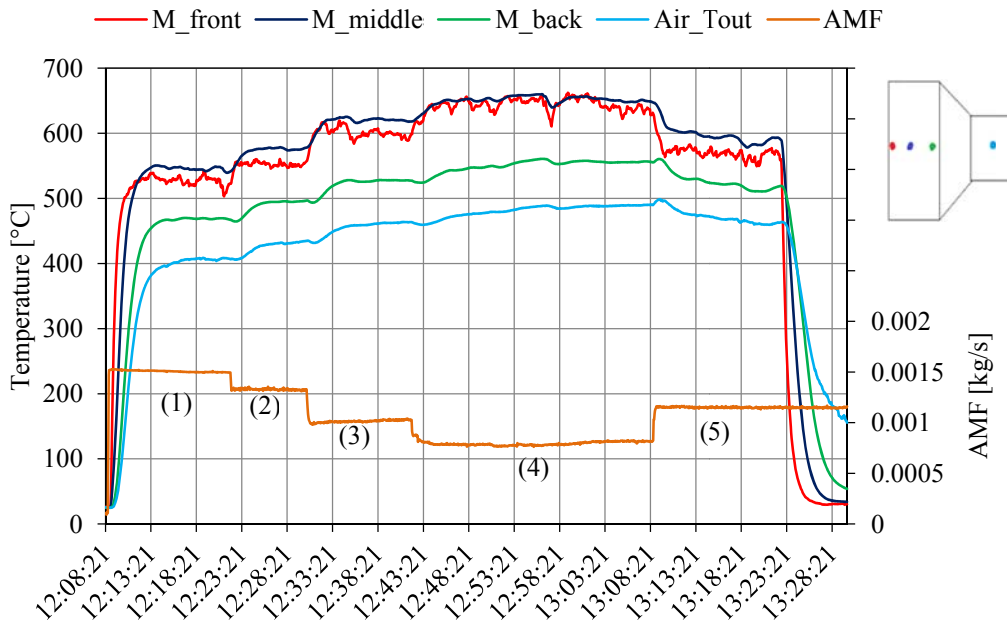


**Figure 6.1:** Temperature measurements for the (6/4/2) absorber at five different AMFs

The absorber experiences a large thermal shock at the start of the testing period going from ambient temperatures up to more than 500 °C within 7 minutes. The wire mesh absorber has the benefit of being able to handle this shock very well, since the wires are woven together and therefore allowed to slightly expand and move independently.

It is clear from Figure 6.1 that the temperatures of the screens and outlet air increase when the AMF decreases, and that the absorber has a very quick response time to this change. For AMF 1, 2, 3 and 5 the deeper part of the absorber (dark blue line) measure a higher temperature than the front (red line). This proves that there is good penetration into the depth of the absorber. The lower porosity of the M12 screen absorbs more radiation which raises the mesh temperature. This effect is desirable since it lowers the losses from the front and promotes the volumetric effect. The small fluctuations in the temperature reading of the front screen are due to the influence of wind conditions, as well as non-perfect thermal contact between the front thermocouple and the screen.

At the fourth AMF the difference between the middle and front screen temperature decreases. The extreme low flow rate results in a poor heat transfer coefficient due to the low Reynolds number. This illustrates that lowering the AMF to increase the outlet air temperature is only effective up to a certain point, since the heat transfer becomes too poor and the thermal losses from the front too

high. Thus, to further increase the outlet air temperature, the incident flux would have to be increased to allow higher AMFs and more energy available to transfer to the air. The maximum outlet temperatures were therefore restricted by the capabilities of the concentrator and not by the absorber material or design.

The temperature distributions through the absorber and the respective outlet air temperatures are shown in Figure 6.2 for the first four AMFs. The shape of the distribution stays the same when the flow rate is decreased and only the temperature increases. The poor effective conductivity of the front M6 screens help to maintain the high temperature deeper into the absorber, and the large open area ratio allow good flux penetration.

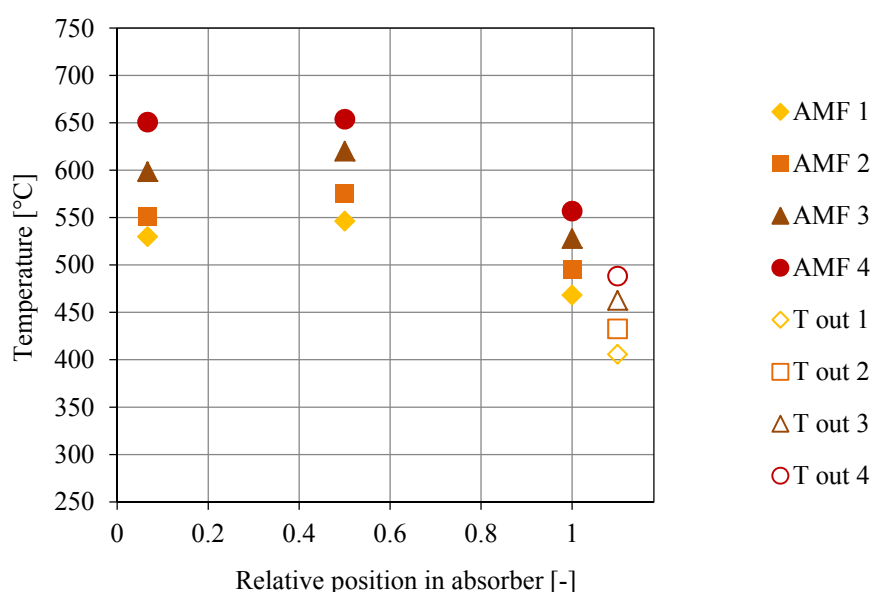


**Figure 6.2:** Temperature distribution through the (6/4/2) absorber and outlet air temperature at four different AMFs

It is clear that the mesh and the outlet air are not at the same temperature at the outlet of the absorber. This is explained by the location where the thermocouples measure the respective temperatures. The back absorber thermocouple measures the center of the absorber where the temperature is the highest, while the outlet air temperature is measured in the throat of the cup where the outlet air is mixed, and therefore cooler.

The temperature of the cup material during testing was always only a few degrees higher than the air inside the receiver housing surrounding the cup. The cup

material reached a temperature of 350 °C and the surrounding air 347 °C during the lowest AMF while the outlet air temperature were 488 °C.

## 6.2.2. Thermal Performance

The measured and calculated performance results of the (6/4/2) absorber at each quasi-steady state condition are provided in Table 6.1. The DNI, ambient temperature and wind conditions were fairly constant between the different AMFs tested, which allows for an accurate comparison between them.

**Table 6.1:** Measured and calculated results for the (6/4/2) absorber at the quasi-steady state condition of each AMF

	Unit	AMF 1	AMF 2	AMF 3	AMF 4
<b>Time</b>	hh:mm	12:19	12:30	12:41	13:01
<b>AMF</b>	kg/s	0.00150	0.00132	0.00102	0.00081
<b>DNI</b>	W/m <sup>2</sup>	786	785	780	778
<b>T out air</b>	°C	406	433	463	488
<b>T front screen</b>	°C	530	551	598	651
<b>PoA</b>	W	676.8	678.3	673.6	672.4
<b>Q out <sup>(1)</sup></b>	W	592.06	561.1	467.7	392.9
<b>Efficiency</b>	%	87.5	82.7	69.4	58.4
<b>PoA/AMF</b>	kJ/kg	450.9	513.1	657.8	828.7

(1) Uncertainty of  $\pm 4.6$  %

The thermal performance of the (6/4/2) absorber, at each of the quasi steady state conditions, is plotted in Figure 6.3. This graph plots the thermal efficiency and the outlet air temperature to the ratio of the power on the aperture divided by the air mass flow rate (PoA/AMF). The markers show the measured and calculated values. The linear trend lines are for illustration purposes only.

The radiation losses from the front increase significantly as the temperature increases, which causes the expected drop in efficiency at the lower AMFs. Additionally, at the low flow rates the small pressure drop over the absorber allows the convection and buoyancy-driven flow from the front to dominate the flow of hot air. In other words, the fan does not suck in the heat from the front strong enough and it is therefore lost to the environment.

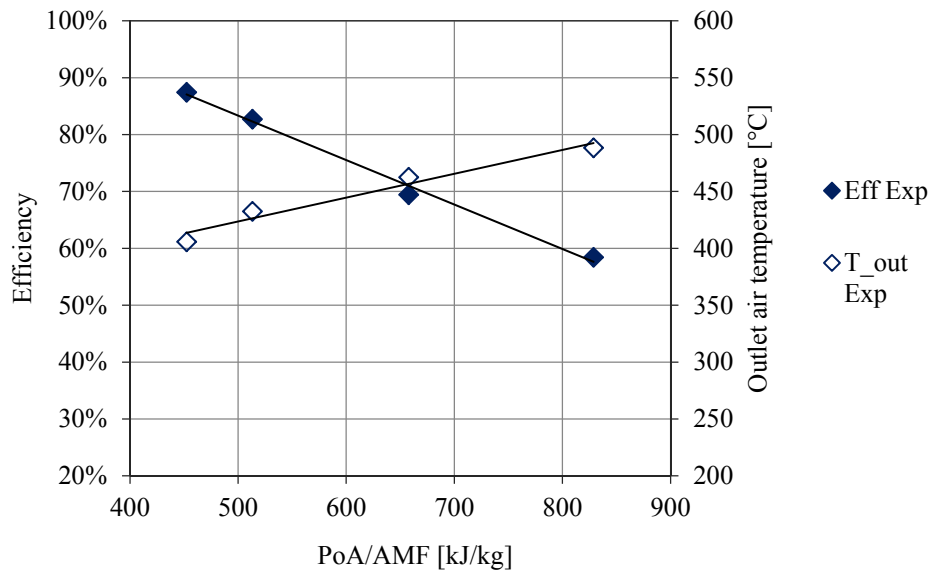


**Figure 6.3:** Experimental performance plot for the (6/4/2) absorber at four different AMFs and average incident flux level of  $55.3 \text{ kW/m}^2$  (trend lines added for illustration purposes)

The maximum outlet air temperature was lower than initially aimed for. This can be explained by the non-uniform incident flux, with its peak near the center of the absorber resulting in higher local absorber temperatures. The thermal image in Figure 6.4 (a) clearly illustrates this effect. This reduces the permeability of the central area due to the increase in viscosity with increasing temperature of the air. Therefore the AMF through this central region is lower compared to the cooler regions at the edges of the absorber (Pabst *et al.*, 2017). The cold air from the edges then lowers the average outlet temperature at the back of the absorber. Since the screens have a poor in-plane thermal conductivity, this temperature gradient is maintained and not diffused outwards.

In Figure 6.4 (a) the thermal image also displays that the front mesh has a slightly lower temperature since the wires of the mesh are visible on the image. This confirms the effect measured with the thermocouples and shown in Figure 6.1. The temperature distribution illustrated in Figure 6.4 (a) supports the use of the Gaussian flux distribution shown in (b).

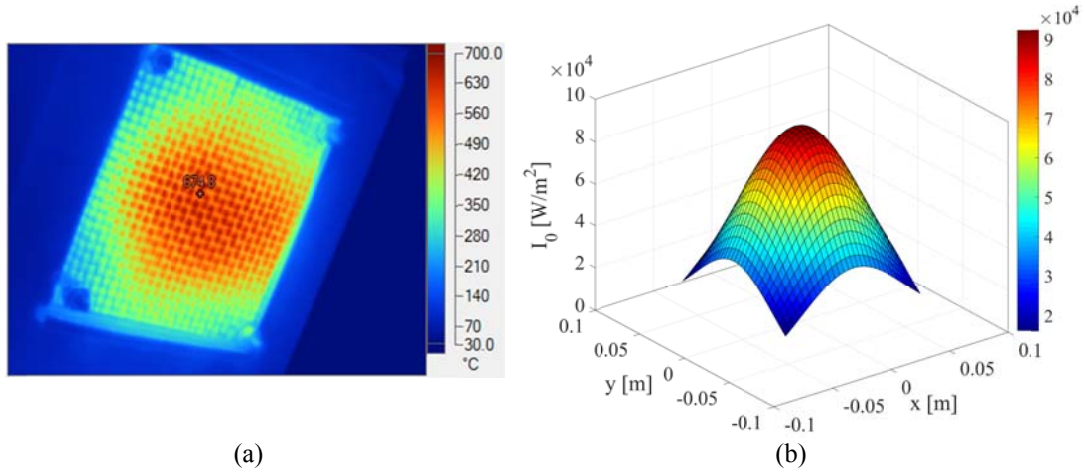


**Figure 6.4:** Thermal image of the absorber and Gaussian flux distribution: (a) image of the temperature distribution over the (6/4/2) absorber aperture, (b) Gaussian flux distribution on absorber aperture with DNI = 775 W/m<sup>2</sup>

### 6.2.3. Combined Results

The thermal performance of all the different absorber configurations tested is displayed on a combined plot in Figure 6.5. All of the configurations tested had the highest efficiency at the highest AMF and the maximum outlet air temperature at the lowest AMF.

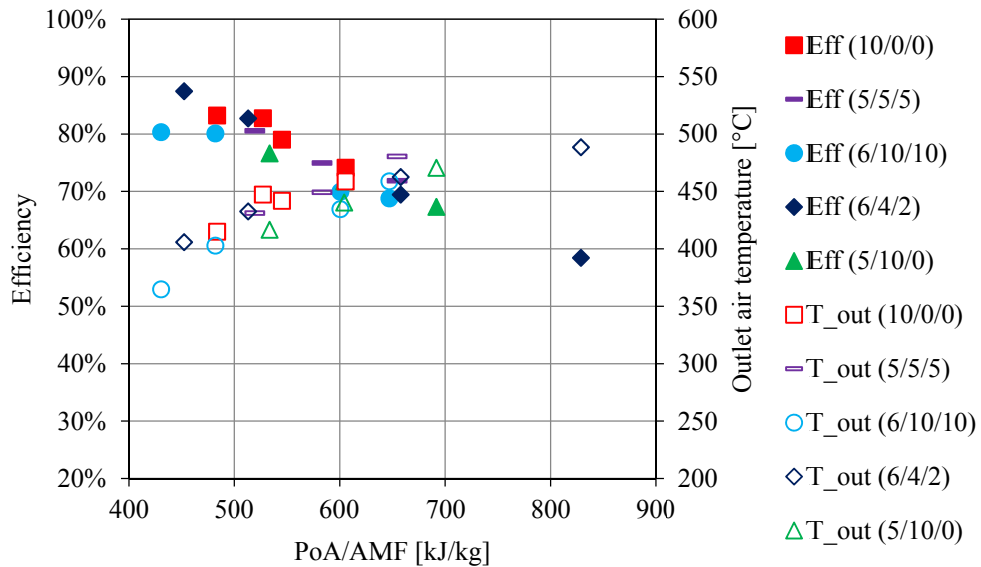


**Figure 6.5:** Combined experimental performance plot of different absorber configurations tested at different AMFs

The ambient conditions have a profound influence on the performance of the absorber and should therefore be considered when comparing the different configurations. These conditions are provided with the performance of each configuration in a summary in Table 6.2.

**Table 6.2:** Experimental performance summary and operating conditions of the different absorber configurations tested

<b>Config.</b>	<b>Avg DNI</b>	<b>T<sub>amb</sub></b>	<b>PoA/ AMF</b>	<b>T<sub>front</sub> screen</b>	<b>T<sub>out</sub> air</b>	<b>Eff</b>
	W/m <sup>2</sup>	°C	kJ/kg	°C	°C	%
(6/4/2)	775 ± 7	22	452 - 829	530 - 651	406 - 488	87.4 - 58.4
(6/4/2)*	775 ± 7	22	452 - 658	530 - 598	406 - 463	87.4 - 69.4
(10/0/0)	825 ± 6	25	484 - 606	539 - 598	415 - 459	83.2 - 74.1
(5/10/0)	909 ± 6	21	533 - 691	630 - 688	417 - 470	76.6 - 67.3
(5/5/5)	882 ± 9	27	519 - 645	597 - 639	431 - 480	80.5 - 71.9
(6/10/10)	731 ± 30	28	430 - 601	574 - 651	365 - 435	80.3 - 69.9

\* Only for the first three AMFs

It is difficult to confirm a trend between the numbers of each screen used and the thermal performance of the configurations, since the conditions in which they were tested varied so much. It is however clear that the (6/4/2) absorber performed the best even with the lowest incident flux.

The total number of screens installed for a configuration influenced the thermal inertia of the absorber, with a higher number resulting in a higher inertia and a lower number giving the absorber a quicker response. The number of screens also influenced the overall depth of the absorber. It is undesirable to have excess screens at the back that do not take part in the heat transfer, since then the air will essentially maintain the temperature through heating the screens.

The results of the experiments indicate that the number of screens installed of the very fine M24 type did not have an obvious effect on the performance of the absorber. This can be because the M6 and M12 screens in the front are too optically dense and therefore the radiation is completely absorbed before it reaches the M24 screens. For the (6/4/2) absorber two of the M24 screens were added at the back to ensure no radiation are scattered or reflected straight through the absorber. The M6 and M12 screens had the biggest effect on the performance and therefore more of them were used.

The efficiency versus outlet temperature is another common way to compare the performance of the different absorbers. This is shown in Figure 6.6 for the five different configurations tested.

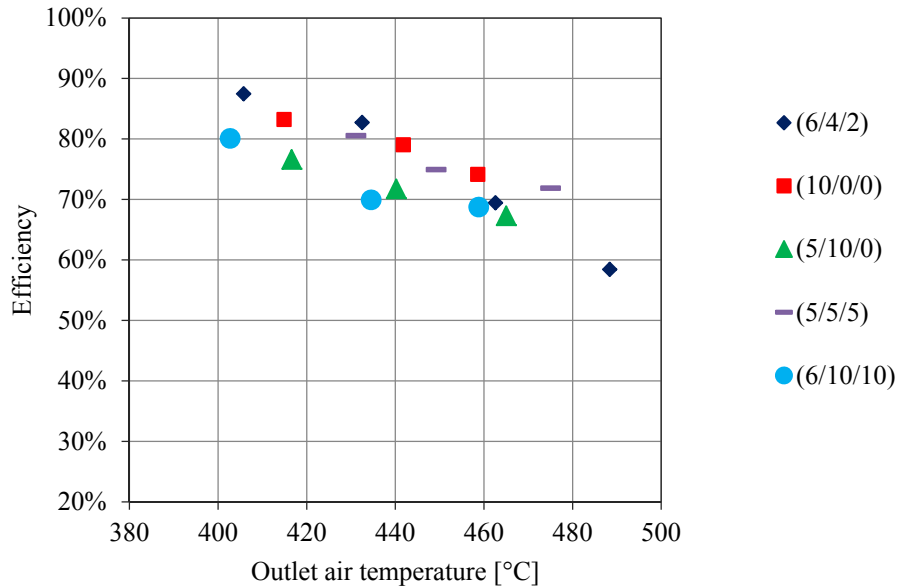


**Figure 6.6:** Experimental measured efficiency and outlet temperature at different AMFs for the different absorber configurations

It is clear that overall the (6/4/2) configuration has the best efficiency over the outlet temperature range. Overall all of the absorbers have comparable thermal performance results. The testing conditions between different absorber, but also between different AMFs for the same absorber should be kept in mind, as provided in Table 6.2.

An important consideration when interpreting the experimental data and measurements is how well the experimental tests represent the performance of a large receiver. The fact that a single cup is tested could be considered as the worst case scenario for several reasons. Firstly, a cup in a large receiver will be surrounded by other cups at high temperature and therefore have even lower losses through its sides. Secondly, the cup will suck in air that is already partially heated through the neighboring cups when the wind blows. It can therefore be concluded that the experimental setup represent the performance of an edge module rather than a central module. With this assumption it can be expected that it is the worst case scenario and that the thermal performance of a central module will be better.



### 6.3. Model Validation and Comparison

The experimental results are used to validate the results from the numerical model. The model was adjusted to simulate the experimental test conditions and a comparison between the two is shown in the performance plot for the (6/4/2) absorber in Figure 6.7. The linear trend lines are once again added for illustration purposes only.

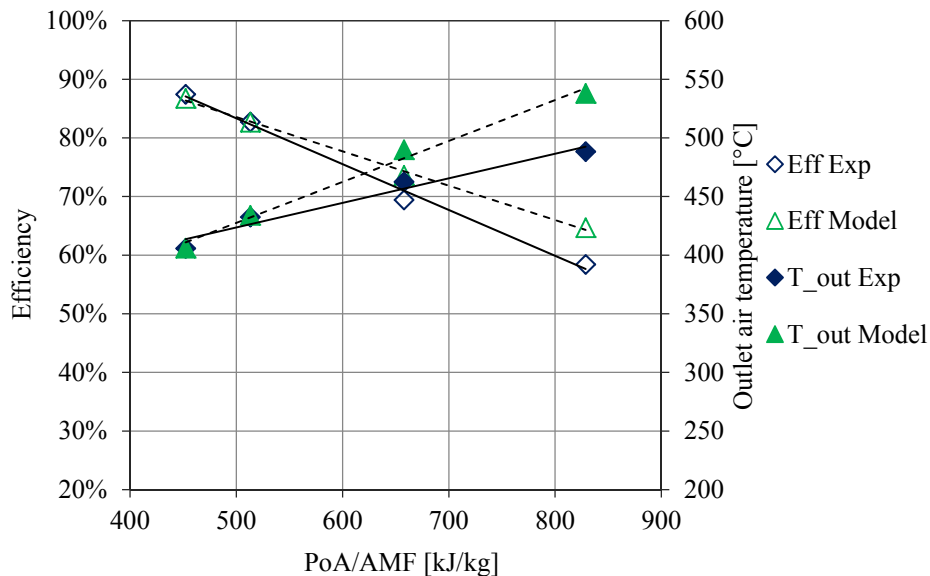


**Figure 6.7:** Comparison of the performance of the (6/4/2) absorber between the numerical model results and experimental measurements at an average incident flux level of  $55.3 \text{ kW/m}^2$

The trends between the numerical model and experimental results are consistent and the general agreement is good at the higher AMFs, but the model over predicts both the outlet air temperature and efficiency at the lower flow rates. For the first two AMFs the deviation from the experimental results is a less than 1 %. For the third and fourth flow rates the deviations are 6 % and 10 % respectively. These percentage deviations are applicable for both temperature and efficiency at each flow rate.

The most significant cause of deviation between the model and the experimental results is the fact that the model assumes a 1-D approximation with a homogenous calculated average flux distribution over the aperture of the absorber. This assumption does not take any in-plane changes into account, such as that the airflow is not always perpendicular to the screens and that the actual absorber allows some parallel flow behind the screens that lower the convective heat

transfer. The non-uniform flux distribution of the experimental setup also causes a difference in permeability over the absorber, as explained earlier, which influences the AMF through the absorber and therefore influences the outlet temperature and efficiency.

When comparing the temperature distribution in Figure 6.2 with the one plotted for the numerical model, it is clear that the assumption of a volumetric heat source for the radiation transfer clearly prevents the model from accurately predicting the temperature distributions through the absorber. The actual absorbers allow much better penetration of the flux into its depth than calculated by the model.

The Reynolds number at the lowest AMF is very close to the lower limit of the correlation of Avila-Marin *et al.* (2017), and therefore the uncertainty of the convective heat transfer coefficient is larger (Natividade, 2015). The Nusselt number correlations and the effective thermal conductivity correlation used for the absorber in the model are also only estimates and do not represent the absorber perfectly.

There are several geometrical discrepancies between the ideal modeled absorber, and the real wire mesh absorber tested in the experiments. These discrepancies include non-perfect inline or staggered arrangement, mesh dimensions deviating from specifications, a difference in surface absorption and roughness of the wires as well as several other factors. The model also assumed perfect and constant conditions and therefore could not adequately compensate for the environmental influences on the experimental setup, such as the continuous variation in wind conditions and DNI input. The model do not account for losses through the insulation of the receiver housing.

In order to further examine the validity of the numerical and experimental results, they are also compared to the previous study carried out by Avila-Marin *et al.* (2013), who tested a wire mesh absorber at PSA. This absorber had an open area ratio going from 61 % to 38 % and the performance plot is shown in Figure 6.8. This absorber consisted of 7 screens and was 9.5 mm thick. The results from the numerical model and experimental tests are plotted with these results on the figure to allow a comparison.

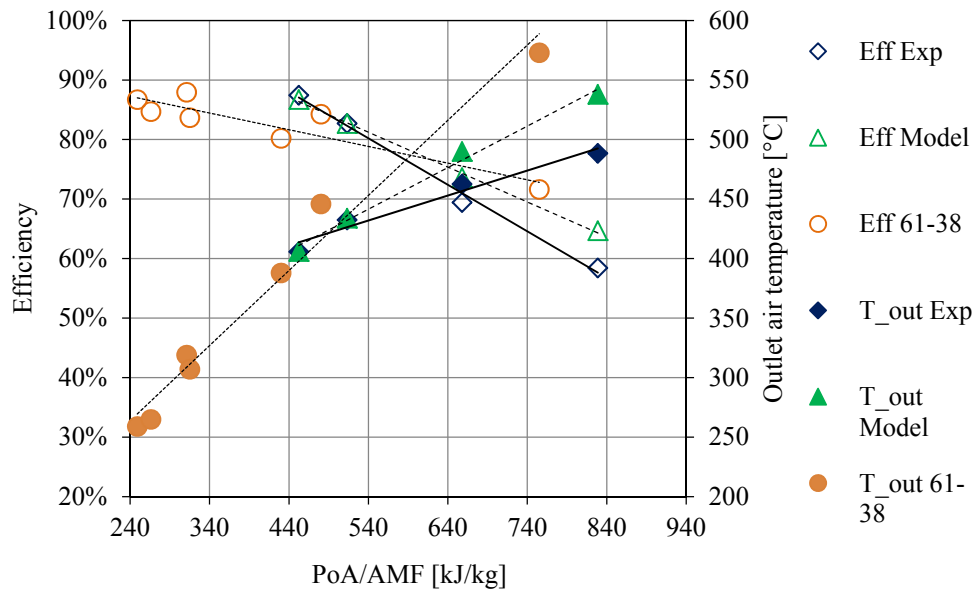


**Figure 6.8:** Performance of the experimental and model results with the wire mesh screen absorber tested at PSA (adapted from (Avila-Marín *et al.*, 2013))

These tests were performed at average flux values of  $220 \text{ kW/m}^2$  to  $260 \text{ kW/m}^2$ , which are significantly higher than the tests performed in this project at average flux values of  $55.3 \text{ kW/m}^2$ . This enabled Avila-Marín *et al.* (2013) to operate at much higher AMFs since the PoA/AMF ratios are comparable to the ratios tested in this project.

The experimental as well as model results have a very good level of agreement in both magnitude and trends with those of Avila *et al.* (2013) at the lower PoA/AMF ratios, but the efficiency as well as outlet air temperature was lower at the higher ratios. The same reasons provided before apply here. Another important consideration is that the tests at PSA were performed at an in-house test setup and were therefore not exposed to the changing ambient conditions.

## 6.4. Observations during Testing

The experimental tests of the absorber concept provided several important observations other than the temperature and performance measurements. These observations are important to evaluate the overall applicability of the wire mesh absorber for this project and concept.

### 6.4.1. Wire Screen Oxidization

The new bright stainless steel wire mesh screens oxidized within the first 1 to 2 hours of being exposed to the high flux intensities and after that stayed constant in color. This proved that AISI 316 wires can operate in these conditions as absorber material. The oxidized screens are shown in Figure 6.9. The measurements from the first tests while the screens were still bright were therefore not used in the performance evaluation of the absorber.

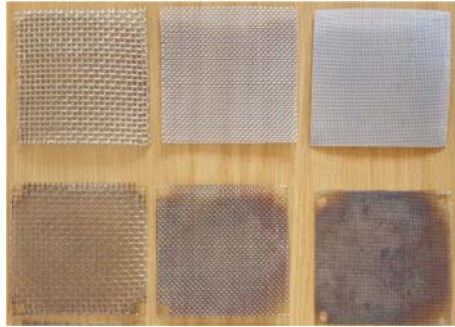


**Figure 6.9:** Samples of new screens compared to oxidized screens

### 6.4.2. Absorber Conductivity

The clear focal spot of the concentrator is evident from inspecting a new absorber after it was placed in focus for a short while, as shown in Figure 6.10 (a). The darker spot is also visible at the back of the absorber, shown in (b). This shows that the effective thermal conduction through the wire mesh screens is significant. It also confirms that the screens have a poor in-plane thermal conductivity, since only the center part have experienced high enough temperatures to become oxidized and the heat was not conducted to the sides of the absorber.

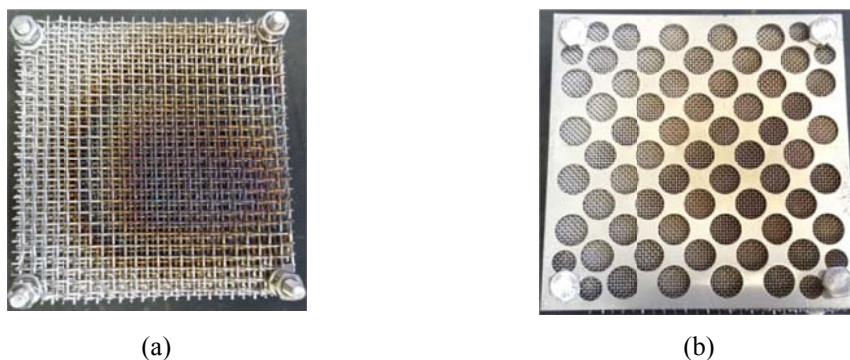


**Figure 6.10:** New absorber showing clear burn mark at focal spot at the front (a) and back (b)

### 6.4.3. Environmental Influences

The absorber has a quick response to changes in environmental conditions. A snapshot of the temperature measurements during a period where a dip in DNI was experienced due to a passing cloud is shown in Figure 6.11.

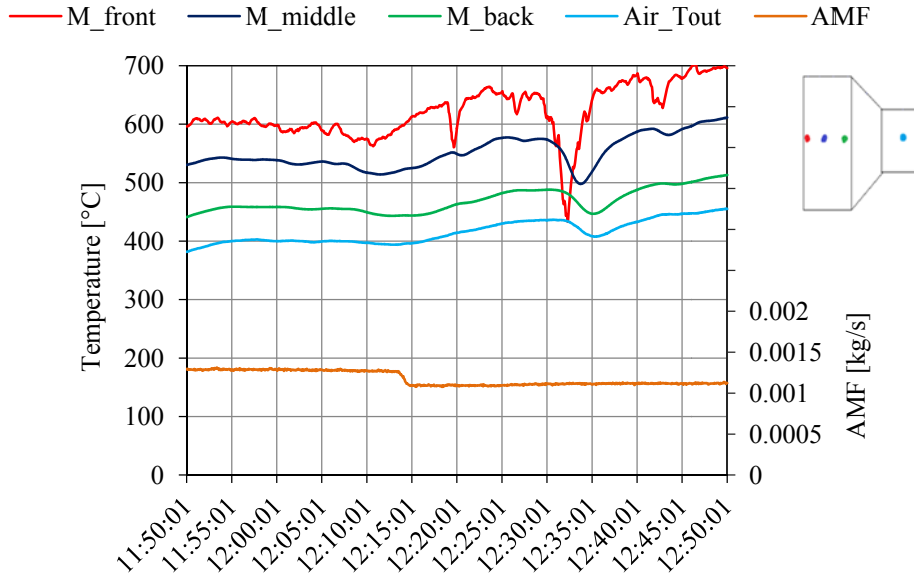


**Figure 6.11:** Experimental temperature plot of the (6/10/10) absorber showing the effect of a dip in DNI due to a small cloud passing over

Figure 6.11 illustrates that the absorber experienced a significant drop in DNI at  $\pm 12:30$ . The absorber had a quick response with a large drop in front temperature due to the sudden drop in incident flux. The thermal inertia of the absorber is clear since the dip in temperature through the depth of the absorber lags behind the dip of the front temperature. Such a variation in operating conditions made it difficult to reach a quasi-steady state condition where the thermal performance could be evaluated at.

The wind also had a major influence on the losses from the front of the absorber and made it difficult for the absorber to reach a steady state condition. A quartz glass window was therefore installed in front of the absorber purely for the purpose of mitigating this effect. The window was slightly larger than the aperture of the absorber and was placed 10 mm away from the front while still being open on the sides to allow ambient air in. This modification however did not adequately remove the influence of the wind and the additional reflection losses from the window further reduced the performance. The window was not included in further

tests. The best way to mitigate the effect of the wind is to operate at a higher AMF through the absorber since the higher inlet velocity will minimize the influence of the cross wind.

## 6.5. Conclusion

The experimental tests investigated different wire mesh absorber configurations under different AMFs. The highest outlet temperatures and lowest efficiencies were consistently reached at the lowest flow rates for all of the absorbers. The low thermal efficiency is due to the radiation losses at the high front temperatures, as well as the convection losses from the front due to the overwhelmingly buoyancy driven flow. The outlet temperature of the absorber is also lowered as a result of the non-homogenous incident flux distribution over the aperture, which causes a difference in permeability and therefore in flow rate between the hot center and cooler edges of the absorber. The effect that the number of screens has on the performance was found to be only significant for the M6 and M12 screens that receive the highest flux values and heat transfer to the air. The maximum outlet temperatures were restricted by the capabilities of the concentrator and not by the absorber. Higher flux intensities will produce more power incident on the absorber to heat up the air to higher temperatures. This will also allow higher flow rates, thereby increasing the heat transfer of the absorber and its efficiency.

The testing of a single cup is considered the worst case scenario for the performance of the absorber, since there was a large flux variation over the aperture and because although insulated, the sides of the absorber were colder than the cup itself. The thermal performance of a large receiver will be better than for the single absorber module measured in the experimental setup.

# Chapter 7

## Conclusion

### 7.1. Discussion of Results

For this project an OVAR was developed to heat up ambient air to charge a rock bed TES. The aim was to develop a simple and cost effective concept that makes use of local content and manufacturing processes. The concept was designed, numerically modeled and experimentally tested with a new small scale test tower and available medium flux concentrator. The main parameters investigated in this project were the effect of the absorber configuration and AMF on the thermal performance of the absorber.

#### *Concept:*

The wire mesh absorber with a gradual porosity was identified as a suitable solution. The absorber consisted of a certain configuration of wire mesh screens, stacked from high porosity screens in the front to lower porosity screens at the back. The screens were placed inside a modular absorber cup, based on the HiTRec concept. The low front surface area and inline wire arrangement followed by a lower porosity mesh with higher specific surface area deeper into the cup, aimed to enhance the performance of the absorber.

This absorber concept offers several advantages: it use a low cost, locally available material, it can be easily installed in any shape and size, a large number of variations in configurations can be tested, the wire material can be upgraded to a higher grade if desired, the wire mesh handles thermal shock very well, and the geometrical properties of the screens can be used to optimize the absorber.

#### *Numerical model:*

The 1-D numerical heat transfer model provided a sensible description and representation of the overall heat transfer process in the absorber. The model

made use of a HEM with LTNE to calculate the temperature profiles of both the solid and the fluid through the absorber. The use of a Gaussian incident flux distribution was characterized and validated with the thermal camera and flux sensors. The radiation was approximated as a volumetric heat source inside the absorber.

There is a good agreement between the model and experimental results at higher AMFs, with a deviation of less than 1 %. The model however overestimated the performance at lower flow rates due to assumptions simplifying the incident flux, mass flow rate distribution through the absorber and Nusselt number correlations which resulted in a deviation of 10 %. For the purpose of investigating the heat transfer and helping understand the influence of various parameters, the numerical model provided adequate insight into the performance of the absorber, and established a good foundation for more advanced numerical models in future work.

#### *Experimental tests:*

The experimental results indicate that at small scale this absorber concept shows promising performances and possibilities. The new test tower that was designed enabled easy testing of different absorber configurations and allows for future optimization. Within the limits of accuracy, the (6/4/2) absorber configuration provided outlet air at 405 °C to 488 °C with a thermal efficiency of 87 % to 58 % under average incident flux values of 55.3 kW/m<sup>2</sup>. In order to ultimately achieve 550 °C outlet air, the total incident power needs to increase which will also increase the efficiency of the absorber since the absorber can then operate under higher AMFs.

The thermal efficiencies were lower than expected due to the high thermal losses associated with the high front temperatures, as well as the low AMFs that the tests were performed at. A higher AMF increase the heat transfer coefficient, lower the front temperature and reduce the effect the wind and convection losses have. The AMF can only be used up to a point to increase the outlet temperature, after which the poor heat transfer results in the thermal losses to outweigh the increase in outlet air temperature.

The outlet temperature was not limited by the absorber concept, but by the low concentration ratio capabilities of the test setup. The outlet temperature can be increased either by testing on a day with higher DNI values or by adding more mirrors to the setup. The fact that the test setup is located outside and that the receiver is not protected from the influence of ambient conditions allowed for a better representation of the actual performance of the receiver. However this also



limited the amount of experimental tests that could be performed. The experimental results are sufficient for the use of a preliminary design analysis and as an initial step towards the development for a large receiver.

The tests demonstrated the simplicity of the absorber and receiver design and operation. Although visual inspection of the mesh showed no signs of melting or damage, long term aging tests are necessary to ensure that the AISI 316 material can sustain its integrity over long term exposure to the concentrated radiation.

## 7.2. Future Work and Recommendations

### *Concept:*

The choice of the wire mesh screens for this concept was based on the experimental findings of Avila-Marin *et al.* (2013). There is however a wide variety of other screens available for optimizing the configuration. The use of knit wire as the absorber material can also be further investigated. A possible optimized concept can include a stack of wire mesh screens with a large open area ratio in the front, followed by a coiled knit wire mesh at the back. This will combine the good penetration and durability of the screens in the front, with the increased heat transfer in the knit wire due to its unstructured arrangement and thin wires.

The perforated back plate should be modified to have smaller holes around the edges of the plate to increase the AMF through the hot center part of the absorber, and decrease the flow rate through the cooler edges.

### *Numerical model:*

It is clear from the results that the 1-D numerical model could provide a realistic insight into the overall heat transfer process, but that there is significant deviation at lower AMFs. The model could also not accurately predict the temperature distribution through the depth of the absorber, due to the assumption of the radiation as a volumetric heat source. Therefore a more detailed approach that makes use of CFD to solve the mass, momentum and energy equations through the absorber should be taken. The use of a 2-D model with the P1 radiation approximation should be investigated to better account for the effect of the flux distribution over the aperture and radiation attenuation.

### *Experimental tests:*

The mathematical model of the absorber can only be as accurate as the correlations used for the various characteristics of the mesh. The optical properties

such as screen transmittance, reflectance and overall extinction through different absorber configurations should be experimentally measured. The volumetric heat transfer coefficient can also be improved through doing a transient test. The pressure drop over the absorber was disregarded for this project, but should be included in future work towards a larger receiver.

The experimental tests provided performance results for a single cup in operation. The next step towards developing a large receiver would be to test a matrix of absorber modules and find the influence they have on each other and on the performance of the receiver. The air return loop has not yet been tested, since the return air from the rock bed TES is too low to significantly increase the receiver efficiency. The return air should be closer to the air temperature measured inside the receiver housing, which was 350 °C. Otherwise the conduction losses through the sides of the cup will be too high and reduce the outlet air temperature. In order to adequately test the effect of the return air on the test setup, electric heaters can be used to preheat the return air if necessary.

The uncertainty of the efficiency measured for the wire mesh absorber is high since the incident power could not be exactly measured. Although the use of the Gaussian distribution function and by correlating it with the thermal camera and flux sensors proved to be a very good representation of the actual setup, a more accurate flux measuring system should be used to validate the results.

### 7.3. Conclusion

Sunlight, air and rocks are all over available, sustainable and cheap. The combination of a rock bed TES system that is charged with an open volumetric air receiver provide a low-cost and simple solution that use CSP to produce and store high temperature, unpressurized air for power generation or process heat applications. The goal of the research was therefore reached through successful development of a suitable absorber concept that addresses the high costs and technology requirements associated with this technology. Each of the objectives set out for this project were reached:

- The first objective was reached through using a gradual porosity wire mesh screen absorber inside a modular stainless steel cup. The wire mesh screens are locally available and the modular cup can be manufactured through simple bending and welding processes. This concept is reliable, easily scalable and cost effective.

- The second objective was achieved through developing a numerical model that could realistically calculate the thermal performance at steady state conditions and represent the overall heat transfer through a volumetric absorber with changing geometrical properties through its depth.
- The last objective was completed through experimentally testing and validating the absorber concept and by measuring the thermal performance thereof. The new small scale tower that was designed allows easy testing of different absorber configurations and allows for future tests and optimization.

It is therefore concluded that the wire mesh screen in a modular cup is a suitable absorber concept for an open volumetric air receiver to ultimately produce the hot air to charge the rock bed thermal energy storage system.

# Appendices

# Appendix A

## Thermophysical Properties of Air

### A.1. Air Property Figures

The thermophysical properties of ambient air are plotted over the typical temperature range operated at, which was between 20 °C and 600 °C. The values of each property over the temperature range were obtained from property tables from Eckert and Drake (1972). The aim of the figures is to aid in the understanding of the influence of the temperature on the following four properties and the effect that they have on the thermal performance of the absorber.

- Specific heat capacity:  $c_p$ , J/(kg · K)
- Density:  $\rho$ , kg/m<sup>3</sup>
- Thermal conductivity:  $k$ , W/(m · K)
- Dynamic viscosity:  $\mu$ , kg/(m · s)

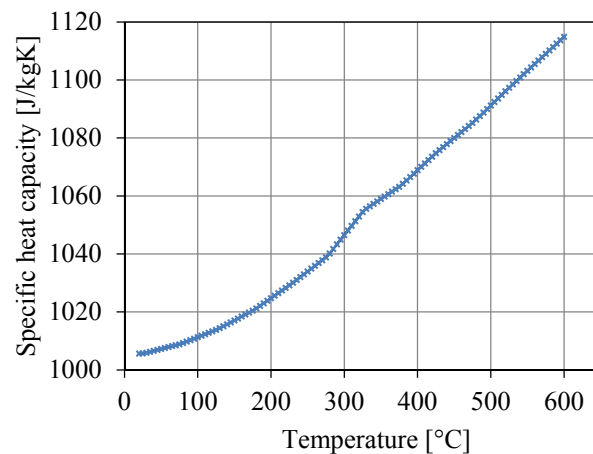


**Figure A.1:** Specific heat capacity of air over a temperature range

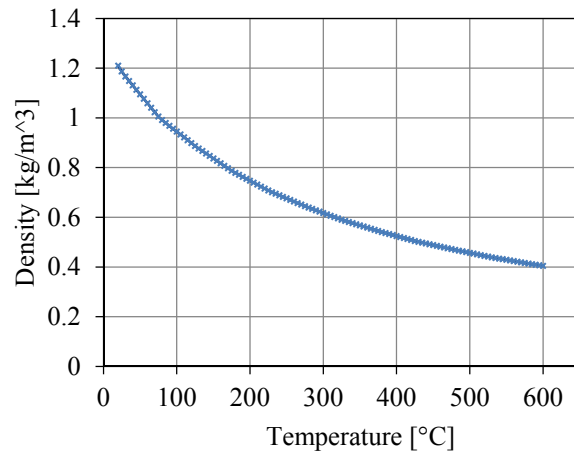


**Figure A.2:** Density of air over a temperature range

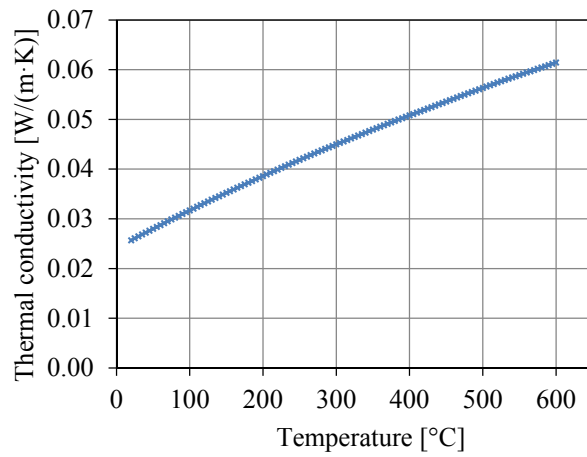


**Figure A.3:** Thermal conductivity of air over a temperature range

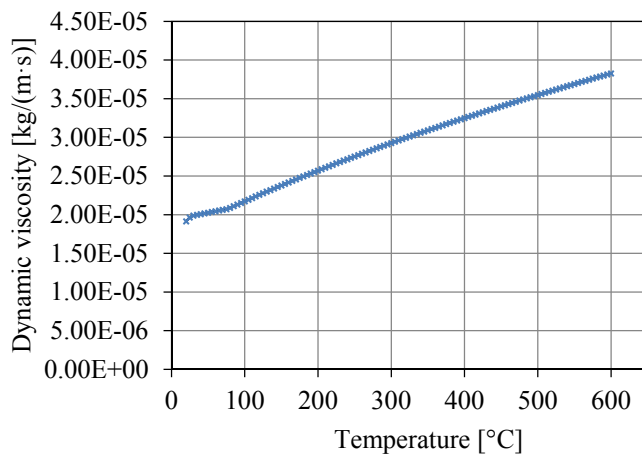


**Figure A.4:** Dynamic viscosity of air over a temperature range

# Appendix B

## Incident Flux Calculation

### B.1. Introduction

The incident flux is an important parameter in calculating the thermal efficiency of the absorber, since it represents the effective energy available to transfer to the air. To measure the incident flux levels over the absorber aperture usually involves advanced tools such as Lambertian targets coupled with a CCD camera. These devices are expensive and require extensive knowledge and experience to correctly install and calibrate. Since the optics from the solar field is outside the scope of this project, this was not considered for the flux measurement.

A detailed Soltrace simulation was performed by Kretzschmar (2014) who developed the concentrator. Kretzschmar also designed and manufactured a flat-plate water cooled calorimeter to experimentally validate and measure the incident power. This device was however not available when tests for this project were performed. The previous results thereof were used to validate the measurements and methodology used in this project. The methodology was already introduced and briefly discussed in Chapter 4.

### B.2. Methodology

As a first assumption, the incident flux levels were considered constant over the absorber aperture. The visual investigation of the new absorber after it was placed in the concentration however clearly showed that the flux was not constant over the absorber, and that a peak was experienced around the center. This is typical for a solar concentrator and therefore a Gaussian-type flux distribution from Roldán *et al.* (2014) was assumed over the aperture of the absorber. The distribution is given by:

$$I_0(x, y) = I_{0,\text{peak}} e^{\left(\frac{-(x^2+y^2)}{2\sigma^2}\right)} \quad (\text{B.1})$$

The  $x$  and  $y$  coordinates discretize the aperture. In order for the function to correlate with the actual flux from the experimental setup, the peak flux as well and the variance of the distribution is required. The variance,  $\sigma$ , provides the distribution of the function over the aperture. The peak flux,  $I_{0,\text{peak}}$  is calculated through multiplying the DNI at the time of testing with a calculated peak concentration ratio,  $c_{\text{peak}}$ , on the center of the absorber from the concentrator:

$$I_{0,\text{peak}} = \text{DNI}c_{\text{peak}} \quad (\text{B.2})$$

The peak concentration ratio and variance were then the two variables that needed to be determined. The methodology used to find and measure this was to install a heat flux sensor in the place of the absorber that measured the peak incident flux as a function of DNI and the number of mirrors reflecting on the absorber. The variance of the flux distribution was assumed to be represented by the temperature distribution over the aperture, and was correlated with the use of a thermal image from a thermal camera.

### B.3. Equipment

The following equipment was used to measure and evaluate the incident flux and temperature distribution over the absorber aperture.

#### B.3.1. Flux Sensors

The peak flux was measured separately with two water cooled heat flux sensors. The second sensor was used to validate the measurements of the first sensor. The details of the sensors can be found in Table B.1 and Table B.2. Both sensors were connected to the data logger to take and store the measurements at a 3 second interval. The DNI values were obtained from the Sonbesie weather station.

**Table B.1:** Specifications for the Vatel TG1000-0 with AMP-15 flux sensor

Parameter	Unit	Value or range
Sensor range	kW/m <sup>2</sup>	0 to 50
Sensor sensitivity	mV/W/cm <sup>2</sup>	220.264
Uncertainty at nominal range	%	3



**Table B.2:** Specifications for the Hukseflux SBG01-010 flux sensor

Parameter	Unit	Value or range
Sensor range	kW/m <sup>2</sup>	0 to 10
Sensor sensitivity	V/W/cm <sup>2</sup>	0.634 x 10 <sup>-6</sup>
Uncertainty at nominal range	%	6.3 %

### B.3.2. Thermal Camera

The most relevant specifications of the thermal camera are provided Table B.3.

**Table B.3:** Specifications for the Fluke Ti400 (Fluke Corporation, 2013)

Parameter	Unit	Value or range
Temperature range	°C	-20 to 1200
Accuracy	°C or %	± 2 °C or 2 % (whichever is greater)
Detector resolution	-	320 x 240
Infrared spectral band	µm	7.5 to 14 (long wave)

## B.4. Peak Concentration Ratio

The solar field consists of in total 152 mirrors that are arranged in 9 rows of 17 mirrors each. The left and right hand sides of the field, the aim mirror and the tower is illustrated in Figure B.1.

Left hand side (LHS)									Aim col.	Right hand side (RHS)								
9	8	7	6	5	4	3	2	1	2	3	4	5	6	7	8	9		
9	8	7	6	5	4	3	2	1	2	3	4	5	6	7	8	9		
9	8	7	6	5	4	3	2	1	2	3	4	5	6	7	8	9		
9	8	7	6	5	4	3	2	1	2	3	4	5	6	7	8	9		
9	8	7	6	5	4	3	2	1	2	3	4	5	6	7	8	9		
9	8	7	6	5	4	3	2	1	2	3	4	5	6	7	8	9		
9	8	7	6	5	4	3	2	1	2	3	4	5	6	7	8	9		
9	8	7	6	5	4	3	2	1	2	3	4	5	6	7	8	9		

**Figure B.1:** Solar field layout of the medium flux concentrator showing the two sides as well as aiming mirror and tower locations

Since the flux sensors had a limited maximum range, part of the field had to be covered in order to reduce the total concentration ratio while measurements were taken. The partly covered RHS of the field is shown in Figure B.2.

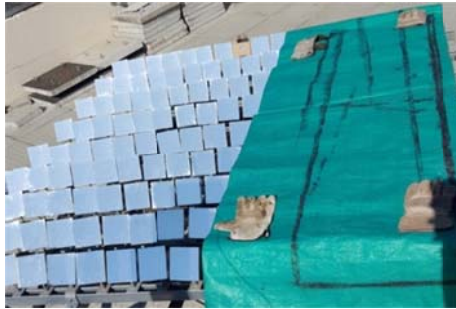


**Figure B.2:** Partly covered solar field during flux measurement of the LHS of the field

The flux sensor was installed in the center of the absorber where the peak concentration ratio or flux was experienced. At first the complete field and thus all the mirrors were covered, except for the aiming mirror. A single column of mirrors was then opened and the incident flux measured. More columns were then systematically opened and the increased flux recorded. When the sensor started to measure close to its maximum range, no further rows are opened in order to protect the equipment. A sample plot of the measured flux at each step is shown in Figure B.3.

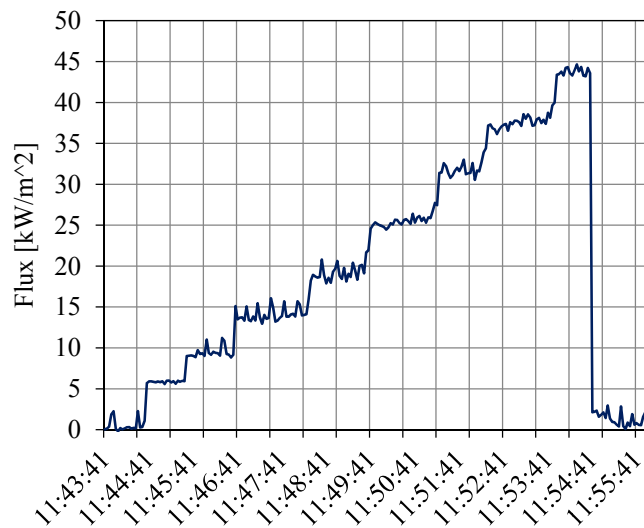


**Figure B.3:** Measured peak flux on the absorber as more columns of mirrors are opened

The peak concentration ratio is calculated by normalizing the measured incident flux with the DNI at that time (Romero & Steinfeld, 2012):

$$c_{\text{peak}} = \frac{\text{Flux}}{\text{DNI}} \quad (\text{B.3})$$

The measured flux, DNI and calculated peak concentration ratio is determined for each new column of mirrors added to the open part of the field. The total number of open mirrors takes the mirrors that are covered by the shadow of the tower into account. The results are presented in Table B.4.

**Table B.4:** Flux measurements and peak concentration ratios calculated for the RHS of the field

<b>Column added</b>	<b>Total no. of open mirrors</b>	<b>Measured flux kW/m<sup>2</sup></b>	<b>DNI W/m<sup>2</sup></b>	<b>Concentration ratio, c<sub>peak</sub></b>
Aim row	8	5.35	852	6.28
+ 1	14.5	9.51	853	11.14
+ 1	21	14.10	856	16.47
+ 1	30	19.14	855	22.38
+ 1	39	25.36	850	29.84
+ 1	48	31.67	853	37.14
+ 1	57	37.49	855	43.82
+ 1	66	43.81	855	51.27

This procedure is repeated for the both the RHS and LHS of the field. The peak concentration ratios are then plotted against the number of open mirrors for both sides. A linear function is fitted to the sets of data points. The plot for the RHS is illustrated in Figure B.4 and the LHS is plotted in Figure B.5.

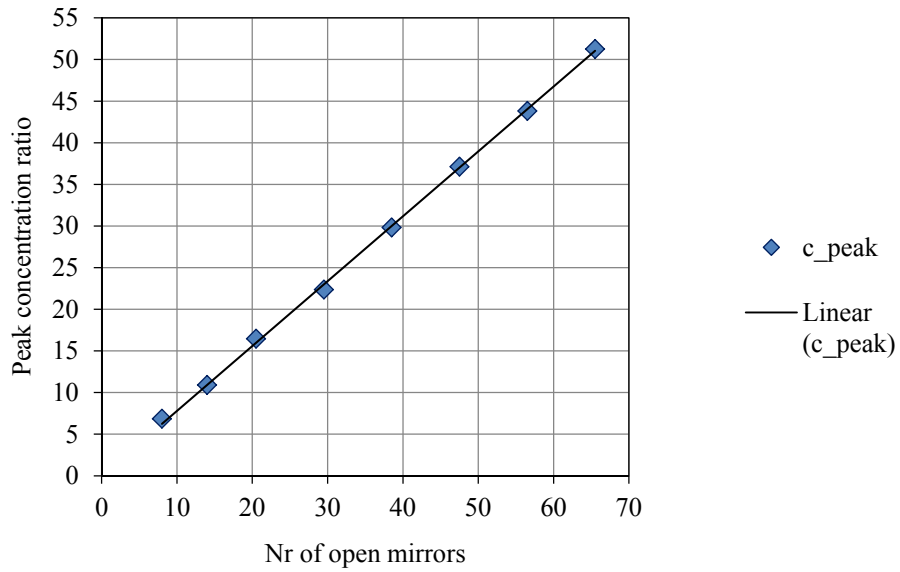


**Figure B.4:** Peak concentration ratio against the number of mirrors open on the RHS (linear function fitted through points)

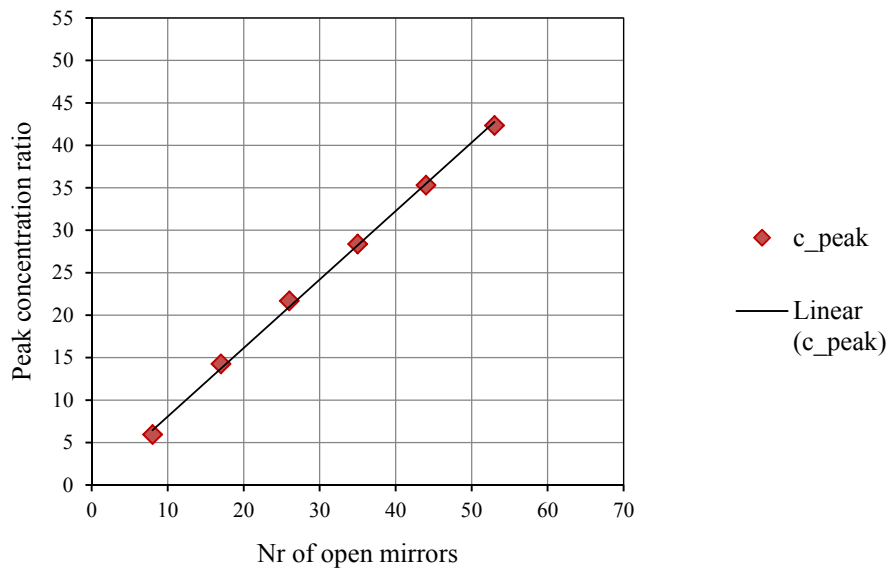


**Figure B.5:** Peak concentration ratio against the number of mirrors open on the LHS (linear function fitted through points)

Due to the tracking limitation of the setup, there was not enough time to open all the columns of the LHS during the same day. The linear trend line of the measurements is however clear. With the use of the linear function the peak concentration ratio can be expressed as a function of the number of open mirrors.

The slope of the lines correlates very well between the two sides and is for the RHS 0.778 and for the LHS 0.792. Both have  $R^2$  values of  $> 0.999$ . An average between the two of 0.785 is used to represent the whole field. The peak concentration ratio correlation is therefore:

$$c_{\text{peak}} = 0.785(Nr_{\text{mirs}}) \quad (\text{B.4})$$

When the complete solar field is open and the mirrors in the shadow of the tower as well as the aiming mirror are subtracted, the peak concentration ratio is:

$$c_{\text{peak}} = 0.785(152 - 4 - 1) = 115.4 \quad (\text{B.5})$$

## B.5. Variance

The variance of the Gaussian distribution is correlated with the temperature distribution captured with the thermal camera, illustrated in Figure B.6.

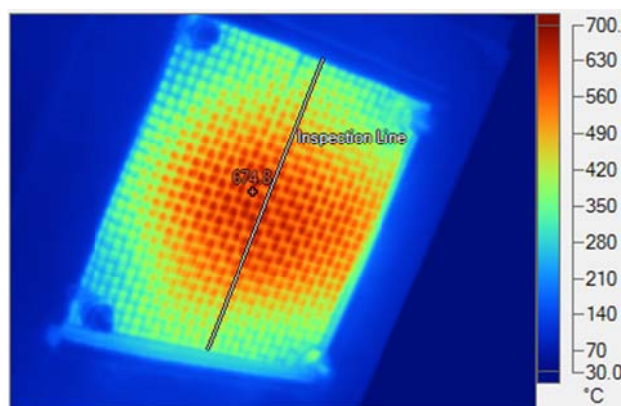


**Figure B.6:** Image from the thermal camera showing the temperature distribution over the absorber aperture, with an inspection line added

On the Fluke SmartView software an inspection line was drawn over the aperture of the absorber. The program exports the temperature readings of the image on the line, and these points were then plotted. The same Gaussian function provided in Equation (B.1) was then used to calculate and plot a temperature distribution. The average maximum temperature of the inspection line was used as the peak value and the variance was altered until the best fit was obtained between the measured and calculated values. The variance value that produced the best fit was  $\sigma = 0.0435 \text{ m}^{-1}$ . The points obtained from the image and the Gaussian function is compared in Figure B.7.

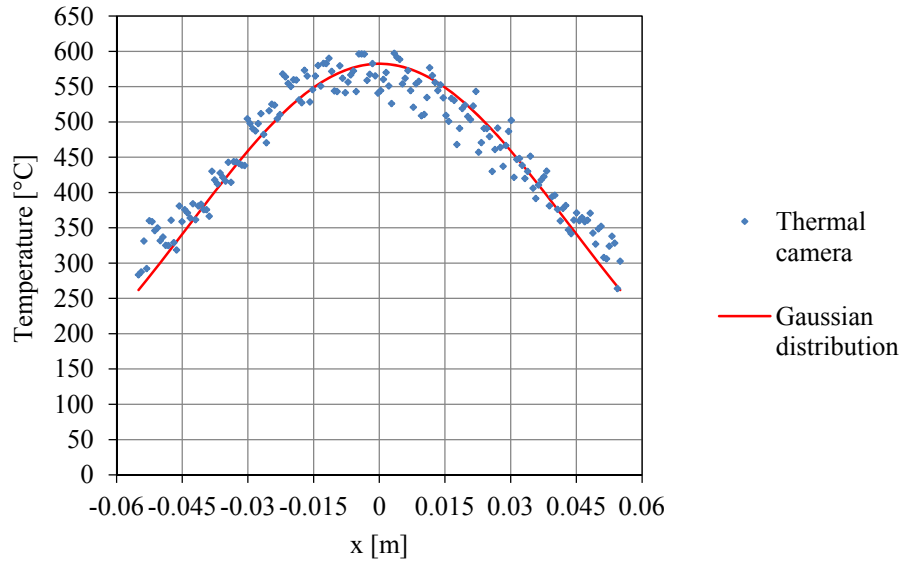


**Figure B.7:** Temperature distribution over the absorber aperture at the inspection line, and calculated Gaussian distribution function

## B.6. Overall Setup Performance

The total power incident on the absorber's aperture,  $P_{oA}$ , is calculated through integrating the flux distribution function over the aperture area:

$$P_{oA} = \int_{-y}^y \int_{-x}^x I_0(x, y) dx dy \quad (\text{B.6})$$

An average homogenous flux distribution is calculated for the front of the absorber that is representative of the total power input to the absorber. This is calculated by dividing the power on the aperture with the area of the aperture:

$$I_{0,avg} = \frac{P_{oA}}{A_{abs}} \quad (\text{B.7})$$

This average flux can then be used to calculate an overall average concentration ratio for the concentrator:

$$c_{avg} = \frac{I_{0,avg}}{DNI} \quad (\text{B.8})$$

## B.7. Validation

The use of the Gaussian distributed flux function can be validated by comparing the total power on the aperture calculated through the function with the power measured with the calorimeter by Roos (2016) on a day with  $\text{DNI} = 998.4 \text{ W/m}^2$ .

**Table B.5:** Comparison between the total incident power and average concentration ratio between the use of a Gaussian flux distribution function and the measurements made with the calorimeter

	<b>Gaussian distribution function</b>	<b>Calorimeter used by Roos (2016)</b>
<b>Total incident power</b>	939.8 W	941.5 W ( $\pm 40.9 \text{ W}$ or 4.3 % standard deviation)
<b>Average concentration ratio</b>	71.18	71.3

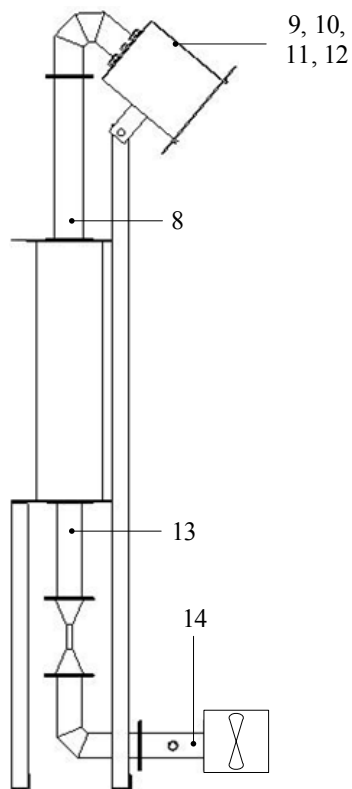
The two different methods are in very good agreement with one another and the Gaussian distribution function is therefore accepted as adequate to represent the incident flux from the concentrator.

# Appendix C

## Test Tower

### C.1. Thermocouple Layout

The complete thermocouple layout of the test tower is shown in Figure C.1.



TC no.	Measurement
1 to 4	Absorber
5	Outlet air
6	Cup material
7	Inside of housing
8	Rock bed inlet
9 to 12	Housing insulation
13	Rock bed outlet
14	Fan inlet

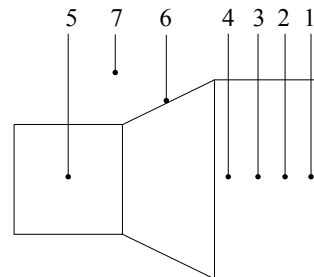
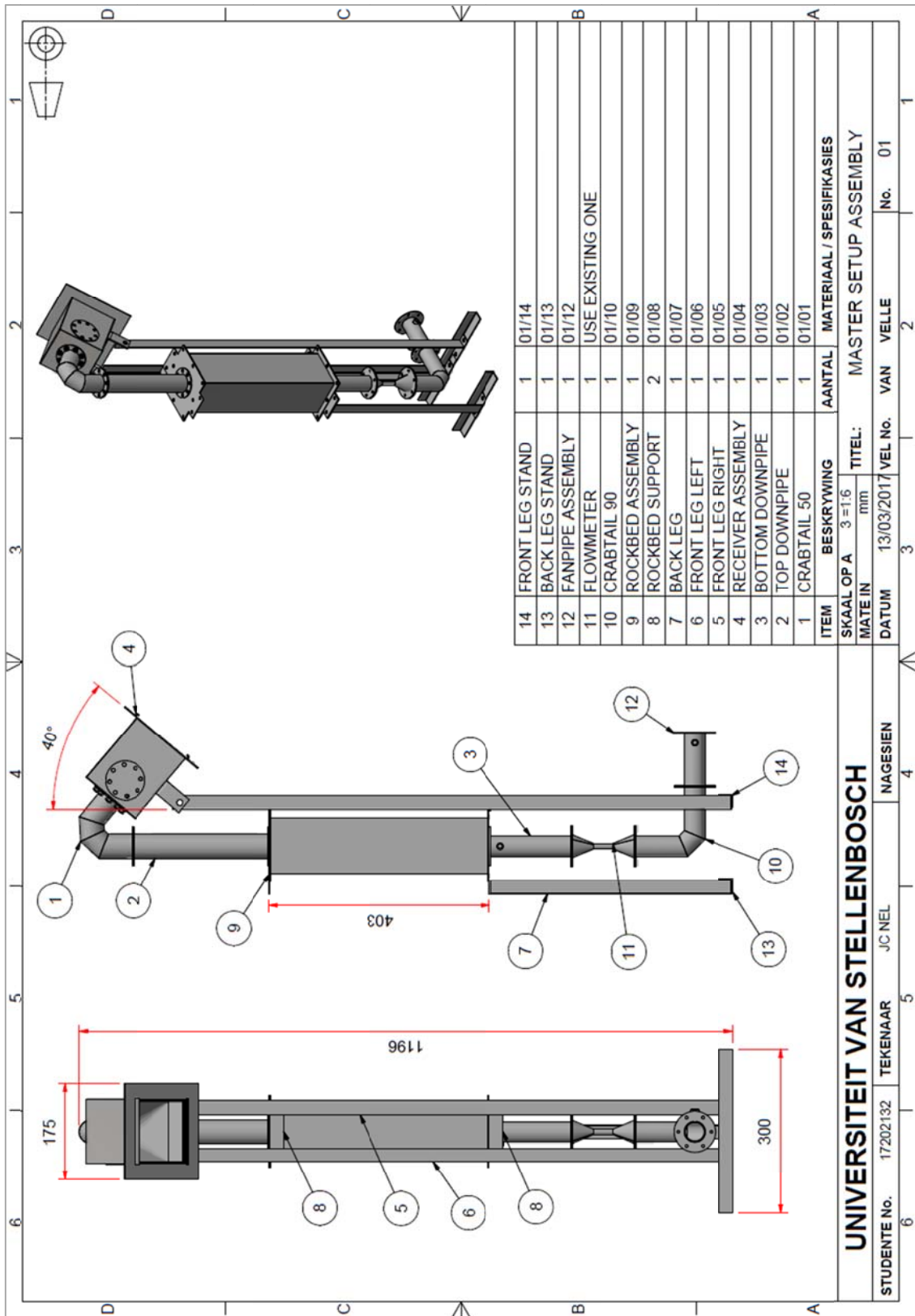


**Figure C.1:** Thermocouple locations throughout the test tower and absorber (not to scale)



## C.2. Tower Assembly Drawing



# Appendix D

## Flow Meter Calibration

### D.1. Introduction

The AMF through the absorber was measured with a venturi flow meter placed after the rock bed heat exchanger. A pressure transducer connected to the data logger constantly measured the pressure drop over the venturi. The temperature was also measured before the venturi inlet to account for the change in air density through the flow meter during testing.

### D.2. Equipment

#### D.2.1. Venturi Flow Meter

The venturi flow meter was designed and manufactured by Kretzschmar (2014) and have standard dimensions provided for pressure differential meters in Figliola and Beasley (2006). The dimensions are provided in Table D.1.

**Table D.1:** Dimensions of the venturi flow meter

Parameter	Symbol	Dimension	Value
Inlet diameter	$d_{in}$	mm	40
Throat diameter	$d_{thr}$	mm	8
Overall length	$L$	mm	115
$d_{in}/d_{thr}$	$\beta$	-	0.2
Divergence angle	-	°	15

## D.2.2. Pressure Transducer

The differential pressure transducer is an Endress+Hauser Deltabar PMD230 with 4 to 20 mA current output and HART communication protocol. The relevant specifications of the transducer is provided in Table D.2.

**Table D.2:** Specifications for the Endress+Hauser Deltabar PMD230 pressure transducer

Parameter	Unit	Value or range
Measuring range	kPa	-2.5 to 2.5
Set span	kPa	0 to 2.5
Accuracy	%	For a TD 10:1 : $\pm 0.1$ % of set span

The pressure transducer was connected to the data logger and produced a voltage output based on the differential pressure measured. The transducer was first calibrated against a Betz micromanometer (ACIN Instrumenten, 2017) available at the department to obtain a calibrated correlation between the measured pressure drop and the output voltage from the transducer, as illustrated in Figure D.1.

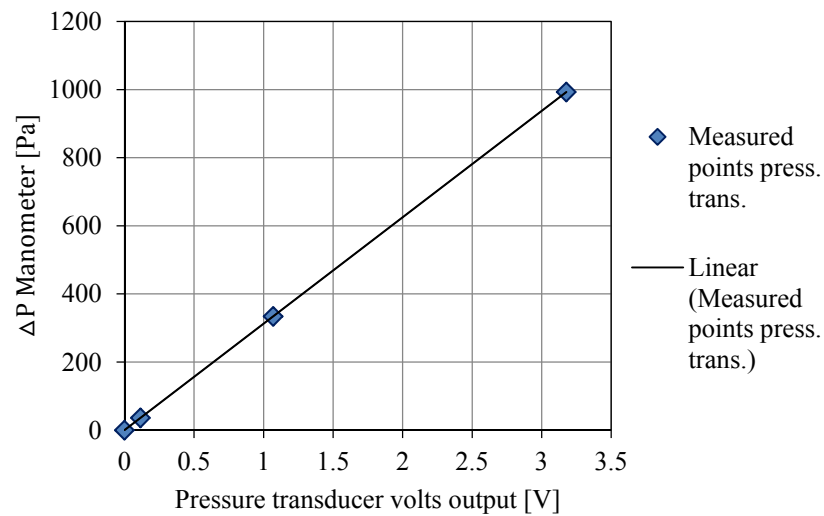


**Figure D.1:** Manometer pressure drop against the pressure transducer voltage output (linear trend line fitted to the points)

A linear trend line was fitted through the data points and the following correlation obtained between the pressure drop and the voltage output from the transducer. The  $R^2$  value for the trend line was 0.9999.

$$\Delta p = \left[ 312.5371 \left( \frac{\text{volts}}{\text{V}} \right) + 0.0221 \right] \text{ Pa} \quad (\text{D.1})$$

### D.3. Venturi Calibration

The venturi flow meter was installed in line with the DISA flow meter calibration unit that is also available at the department. The volumetric flow rate through the DISA flow meter could be accurately determined while the pressure drop over the venturi was measured with the pressure transducer. The ambient conditions in the lab at which calibration took place are provided in Table D.3.

**Table D.3:** Ambient conditions in which calibration took place

Property	Symbol	Unit	Value
Pressure	$P_{amb}$	kPa	101
Temperature	$T_{amb}$	°C	20
Air density	$\rho_{air}$	kg/m <sup>3</sup>	1.2
Kinematic viscosity	$\nu_{air}$	m <sup>2</sup> /s	16.21 x 10 <sup>-6</sup>

The inlet velocity to the venturi is obtained through the dividing the known volumetric flow rate with the area of the venturi inlet:

$$v_{in} = \frac{\dot{V}_{DISA}}{A_{in}} \quad (D.2)$$

The Reynolds number at the venturi inlet is:

$$Re_{in} = \frac{v_{in} d_{in}}{\nu_{air}} \quad (D.3)$$

The volumetric flow rate through the venturi is calculated with the following equation from (White, 1994):

$$\dot{V}_{venturi} = A_{thr} C_d \sqrt{\frac{2(\Delta p_{venturi})}{\rho_{air}(1 - \beta^4)}} \quad (D.4)$$

Since the venturi and the DISA flow meters are installed in series and it is assumed that there is no losses from leakages in the setup, the volumetric flow rate are equal through both flow meters. This then allows the discharge coefficient for the venturi to be calculated from Equation (D.1) for each of the flow rates tested at.

The measured and calculated results are provided in Table D.4 for the six different points tested at. The points were chosen to cover the complete range over which the venturi will operate in the experimental setup.

**Table D.4:** Measured and calculated data for the venturi calibration

Point	$\dot{V}_{\text{Disa}}$ m <sup>3</sup> /s	$\Delta p_{\text{venturi}}$ Pa	$v_{\text{in}}$ m/s	$Re_{\text{in}}$	$C_d$
1	0.00084	171.93	0.67033	1.65E+03	0.981
2	0.00105	273.13	0.83965	2.07E+03	0.975
3	0.00118	341.14	0.93545	2.31E+03	0.972
4	0.00131	423.99	1.03989	2.57E+03	0.969
5	0.00151	574.65	1.20521	2.97E+03	0.965
6	0.00163	669.75	1.29889	3.21E+03	0.963

The discharge coefficient is plotted in Figure D.2 against the inlet Reynolds number. The markers show the measured point and the trend line is added to illustrate the trend on the points.

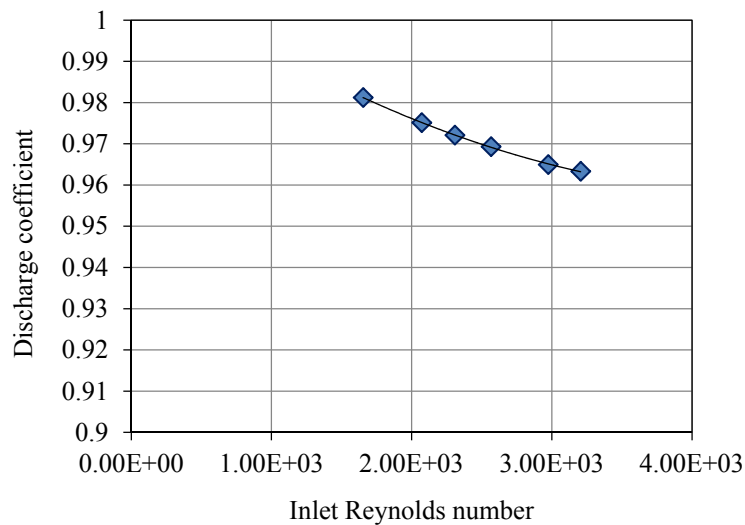


**Figure D.2:** Discharge coefficient for the venturi flow meter over the inlet Reynolds number

The average discharge coefficient then for the venturi flow meter is 0.971 in the range of  $1.65 \times 10^3 < Re_{\text{in}} < 3.21 \times 10^3$ . When the flow rate through the venturi is calculated with this coefficient and Equation (D.1), there is only a 0.16 % deviation from the flow rate measured with the DISA flow meter.

The AMF is calculated by multiplying the density of the air at the inlet temperature to the venturi with the volumetric flow rate through it:

$$\dot{m} = \rho_{\text{air}}(T)\dot{V}_{\text{venturi}}(\Delta p) \quad (\text{D.5})$$

# Appendix E

## Sample Calculations

### E.1. Sample Calculations

This appendix provides a sample calculation of how the thermal performance of the absorber configuration was calculated from the experimental measurements. The measurements and results of the (6/4/2) absorber at the first AMF are used as example as provided in Chapter 6 and repeated here in Table E.1. Each of the entries in the table will be discussed and calculated.

**Table E.1:** Measured and calculated results for the (6/4/2) absorber at the quasi-steady state condition of the first AMF

	<b>Unit</b>	<b>AMF 1</b>
<b>Time</b>	hh:mm	12:19
<b>AMF</b>	kg/s	0.00150
<b>DNI</b>	W/m <sup>2</sup>	786
<b>T out air</b>	°C	406
<b>T front screen</b>	°C	530
<b>PoA</b>	W	676.8
<b>Q out</b>	W	592.06
<b>Efficiency</b>	%	87.5
<b>PoA/AMF</b>	kJ/kg	450.9
<b>T amb</b>	°C	22

**Time:**

The time indicates when the quasi steady state condition was reached. This time is also used to obtain the exact weather conditions from the Sonbesie.

**Weather:**

A snippet of the weather data from the Sonbesie is provided in Table E.2 for the time during which the quasi-steady state condition was experienced for the first AMF. This test was performed on 06/06/2017.

**Table E.2:** Weather data for the first quasi-steady state condition of the (6/4/2) absorber

<b>Timestamp</b>	<b>DNI</b>	<b>T_amb</b>	<b>Relative Humidity</b>	<b>Wind speed</b>
hh:mm	W/m <sup>2</sup>	°C	%	m/s
12:19	786.37	21.75	44.53	2.862
12:20	785.85	21.73	44.75	3.575
12:21	784.63	21.64	45.06	3.737
<b>Averages:</b>	785.61	21.71	44.78	3.39

The relative humidity and wind speed were added to enable a better interpretation of the conditions. The lower than expected DNI for this clear sky day can be explained by the high relative humidity, which made the air hazy and increased the atmospheric scattering and lowering the DNI measured on the ground. The wind speeds is obviously not measured at the test setup and therefore only provide a relative idea of the wind conditions during that time of testing. The wind was fairly constant.

**AMF:**

The AMF is measured with the pressure drop over the Venturi flow meter. First the voltage output from the pressure transducer is converted to a pressure drop. The transducer had an average output of 1.2829 V, which is used in the calibration function to obtain the pressure drop:

$$\begin{aligned}\Delta P_{\text{venturi}} &= \left[ 312.5371 \left( \frac{1.2829 \text{ V}}{V} \right) + 0.0221 \right] \\ &= 400.98 \text{ Pa}\end{aligned}\tag{E.1}$$

The density of the air through the venturi was evaluated at the average outlet temperature from the rock bed heat exchanger. The average rock bed outlet temperature of the rock bed heat exchanger during the quasi-steady state



conditions and was 27.01 °C, which results in an air density of 1.1774 kg/m<sup>3</sup> obtained from the air property tables. The volumetric flow rate is calculated with:

$$\begin{aligned} \dot{V}_{\text{venturi}} &= A_{\text{thr}} C_d \sqrt{\frac{2(\Delta P_{\text{venturi}})}{\rho_{\text{air}}(1 - \beta^4)}} \\ &= \left(\frac{\pi}{4} 0.008^2\right) \cdot 0.971 \cdot \sqrt{\frac{2(400.98)}{1.1774(1 - 0.2^4)}} \\ &= 0.001275 \text{ m}^3/\text{s} \end{aligned} \quad (\text{E.2})$$

The AMF is finally calculated with:

$$\begin{aligned} \dot{m} &= \rho \dot{V}_{\text{venturi}} \\ &= 1.1774 \cdot 0.001275 \\ &= 0.00150 \text{ kg/s} \end{aligned} \quad (\text{E.3})$$

### Temperatures:

The average outlet air temperature from the absorber is 405.75 °C, while the average front screen temperature was 529.81 °C. Both are obtained directly from the thermocouple measurements.

### PoA:

The power on the aperture was calculated with the calculated average concentration ratio:

$$\begin{aligned} PoA &= I_{0,\text{avg}} A_{\text{abs}} \\ &= (DNI c_{\text{avg}}) A_{\text{abs}} \\ &= 785.61 \cdot 71.2 \cdot 0.11^2 \\ &= 676.82 \text{ W} \end{aligned} \quad (\text{E.4})$$

### Q out:

The ambient temperature is used for the inlet condition. The specific heat capacity is evaluated at the average temperature between the inlet and outlet conditions, and the air property tables is used to obtain the corresponding values for the specific heat capacity. The values are then substituted back into the simplified equation to calculate the energy in the air:

$$\begin{aligned}\dot{Q}_{\text{out}} &= \dot{m} \int_{T_{\text{f,in}}}^{T_{\text{f,out}}} c_p(T) dT \\ &= \dot{m} c_p(T_{\text{avg}}) (T_{\text{f,out}} - T_{\text{amb}}) \\ &= 0.00150 \cdot 1027.2 \cdot (405.75 - 21.71) \\ &= 592.06 \text{ W}\end{aligned}\tag{E.5}$$

**Efficiency:**

The efficiency is simply calculated by dividing the thermal power in the air divided by the total incident power on the absorber aperture:

$$\begin{aligned}\eta_{\text{th}} &= \frac{\dot{Q}_{\text{out}}}{PoA} \\ &= \frac{592.06}{676.82} \\ &= 0.875 \text{ or } 87.5 \%\end{aligned}\tag{E.6}$$

# List of References

- Achenbach, T., Bosch, T., Breitbach, G., Klein, T., Götsche, J. & Sauerborn, M. 2013. Theoretical and experimental investigations regarding open volumetric receivers of CRS. *Energy Procedia*. 49:1259–1268.
- ACIN. 2016. <http://www.acin.nl/wp-content/uploads/2016/06/Betz-manual-NL-EN-web.pdf> [2017, September 05].
- ACIN Instrumenten. 2017. *Betz micromanometer Manual*.
- Aichmayer, L. 2009. Solar Receiver Design and Verification for Small Scale Polygeneration Unit. MEng Thesis. Graz University of Technology.
- Avila-Marin, A.L. 2011. Volumetric receivers in Solar Thermal Power Plants with Central Receiver System technology: A review. *Solar Energy*. 85(5):891–910.
- Avila-Marin, A.L., Alvarez-Lara, M. & Fernandez-Reche, J. 2013. Experimental results of gradual porosity wire mesh absorber for volumetric receivers. *Energy Procedia*. 49:275–283.
- Avila-Marin, A.L., Fernandez-Reche, J., Casanova, M., Caliot, C. & Flamant, G. 2017. Numerical simulation of convective heat transfer for inline and stagger stacked plain-weave wire mesh screens and comparison with a local thermal non-equilibrium model. 30003:30003.
- Behar, O., Khellaf, A. & Mohammedi, K. 2013. A review of studies on central receiver solar thermal power plants. *Renewable and Sustainable Energy Reviews*. 23:12–39.
- Buck, R. 2016. *Solarthermal receivers -- research for highest requirements*. [http://www.dlr.de/sf/en/desktopdefault.aspx/tabid-10645/18495\\_read-43274/](http://www.dlr.de/sf/en/desktopdefault.aspx/tabid-10645/18495_read-43274/) [2017, September 06].
- Campbell Scientific. 2009. *CS215 Temperature and Relative Humidity Probe*. North Logan.
- Capuano, R., Fend, T., Hoffschmidt, B. & Pitz-paal, R. 2015. Innovative Volumetric Solar Receiver Micro-Design Based on Numerical Predictions.

- Proceedings of the ASME 2015 International Mechanical Engineering Congress and Exposition*. (November).
- Capuano, R., Fend, T., Stadler, H., Hoffschmidt, B. & Pitz-Paal, R. 2017. Optimized volumetric solar receiver: Thermal performance prediction and experimental validation. *Renewable Energy*. 114:556–566.
- Coleman, H.W. & Steele, W.G. 1999. *Experimentation and uncertainty analysis for engineers*. 2nd ed. New York: Wiley.
- CSP Today. 2016. *Quarterly Update*.
- Department of Energy. 2015. *State of Renewable Energy in South Africa*.
- Eckert, E. & Drake, R. 1972. *Analysis of Heat and Mass Transfer*. New York: McGraw-Hill.
- Endress+Hauser. 2000. *Differential Pressure Transmitter: deltabar S PMD 230/235*.
- Fend, T. 2012. *Characterization of Advanced Solar Air Receiver Materials*. <http://elib.dlr.de/77652/1/Materials.pdf>. [2017, September 06]
- Fend, T., Pitz-Paal, R., Reutter, O., Bauer, J. & Hoffschmidt, B. 2004. Two novel high-porosity materials as volumetric receivers for concentrated solar radiation. *Solar Energy Materials and Solar Cells*. 84(1–4):291–304.
- Figliola, R.S. & Beasley, D.E. 2006. *Theory and Design for Mechanical Measurements*. 4th ed. J. Hayton, J. Rosado, & T. Kulesa (eds.). Phoenix: John Wiley & Sons, Inc.
- Fluke Corporation. 2013. *Ti200, Ti300, Ti400, Ti450, Ti480 Thermal Imagers*. Fluke Corporation.
- Fricker, H., Silva, M., Winkler, C. & Chavez, J. 1988. Design and Test Result of Wire Receiver Experiment – Almeria. Report
- Gomez-Garcia, F., González-Aguilar, J., Olalde, G. & Romero, M. 2016. Thermal and hydrodynamic behavior of ceramic volumetric absorbers for central receiver solar power plants: A review. *Renewable and Sustainable Energy Reviews*. 57:648–658.
- Hellmuth, T. & Matthews, L. 1997. Experimental Characterization of a High-Temperature, High-Flux, Solar Volumetric Receiver. *Experimental Heat Transfer*. 10(2):141–163.
- Hennecke, K., Schwarzbözl, P. & Koll, G. 2007. The solar tower Julich- A solar thermal power plant for test and demonstration of air receiver technology. *Proceedings of ISES World Congress 2007: Solar Energy and Human Settlement*. 1749–1753.

- Ho, C.K. & Iverson, B.D. 2014. Review of high-temperature central receiver designs for concentrating solar power. *Renewable and Sustainable Energy Reviews*. 29:835–846.
- Hoffschmidt, B. 1996. Vergleichende Bewertung verschiedener Konzepte volumetrischer Strahlungsempfänger. University of Cologne.
- Hoffschmidt, B. 2001. Development of ceramic volumetric receiver technology. *Mitteilung - Deutsche Forschungsanstalt fuer Luft- und Raumfahrt*. (10):51–61.
- Hoffschmidt, B., Téllez, F.M., Valverde, A., Fernández, J. & Fernández, V. 2003. Performance Evaluation of the 200-kWth HiTRec-II Open Volumetric Air Receiver. *Journal of Solar Energy Engineering*. 125(1):87.
- Hoffschmidt, B., Dibowski, G. & Beuter, M. 2003. Test results of a 3 MW solar open volumetric receiver. *Proceedings of the ISES Solar World Congress*. 10:1–8.  
<http://scholar.google.com/scholar?hl=en&btnG=Search&q=intitle:TEST+RESULTS+OF+A+3+MW+SOLAR+OPEN+VOLUMETRIC+RECEIVER#0>.
- IEA. 2010. *Technology Roadmap Concentrating Solar Power*. Paris.
- IEA. 2017. Perspectives for the energy - Investment Needs for a Low-Carbon Energy System. <http://www.iea.org/newsroom/news/2017/march/deep-energy-transformation-needed-by-2050-to-limit-rise-in-global-temperature.html>.
- IRENA. 2016. *The Power To Change: Solar and Wind Cost Reduction Potential*.
- Kipp & Zonen. 2008. *CHP1 Pyrheliometer: Instruction Manual*.
- Kretzschmar, H. 2014. The Hybrid Pressurized Air Receiver (Hpar) for Combined Cycle Solar Thermal Power Plants. MEng Thesis. Department of Mechanical Engineering. Stellenbosch University. <http://hdl.handle.net/10019.1/86377>.
- Kretzschmar, H., Mouzouris, M. & Gauché, P. 2014. Development of a Flat-Plate Calorimeter for a Small-Scale Heliostat Field. *Proceedings of SASEC*. 1–10.
- Kribus, A., Grijnevich, M., Gray, Y. & Caliot, C. 2013. Parametric study of volumetric absorber performance. *Energy Procedia*. 49(January):408–417.
- Kribus, A., Gray, Y., Grijnevich, M., Mittelman, G., Mey-Cloutier, S. & Caliot, C. 2014. The promise and challenge of solar volumetric absorbers. *Solar Energy*. 110:463–481.
- Laubscher, H.F., von Backström, T.W. & Dinter, F. 2017. Developing a cost effective rock bed thermal energy storage system: Design and modelling. In Vol. 80015. American Institute of Physics *SolarPACES 2016*. 80015.

- Lubkoll, M. 2017. Performance Characteristics of the Spiky Central Receiver Air Pre-heater ( SCRAP ). PhD Dissertation. Department of Mechanical Engineering. Stellenbosch University.
- Modest, M.F. 2013. RADIATIVE HEAT TRANSFER. In 3rd ed. New York: Elsevier Inc. *Radiative Heat Transfer*. 1–30.
- Natividade, J. 2015. Parametric Study of High-Temperature Volumetric Solar Absorbers. Report. University of Lisbon.
- Pabst, C., Feckler, G., Schmitz, S., Smirnova, O., Capuano, R., Hirth, P. & Fend, T. 2017. Experimental performance of an advanced metal volumetric air receiver for Solar Towers. *Renewable Energy*. 106:91–98.
- Roldán, M.I., Smirnova, O., Fend, T., Casas, J.L. & Zarza, E. 2014. Thermal analysis and design of a volumetric solar absorber depending on the porosity. *Renewable Energy*. 62:116–128.
- Romero, M. & Steinfeld, A. 2012. Concentrating solar thermal power and thermochemical fuels. *Energy & Environmental Science*. 5(11):9234.
- Romero, M., Buck, R. & Pacheco, J.E. 2002. An Update on Solar Central Receiver Systems, Projects, and Technologies. *Journal of Solar Energy Engineering*. 124(2):98.
- Romero-Alvarez, M. & Zarza, E. 2007. Concentrating Solar Thermal Power. In Taylor & Francis Group *Handbook of Energy Efficiency and Renewable Energy*. 21.1-21.97.
- Roos, T. & Harms, T.M. 2016. Preliminary performance analysis of a transverse flow spectrally selective two-slab packed bed volumetric receiver. *AIP Conference Proceedings* 1734, 030032 (2016). <http://dx.doi.org/10.1063/1.4949084>
- Sager, M., Ellen, D., Ritchken, E. & Osborne, S. 2015. Concentrated Solar Power: A strategic industrial development opportunity for South Africa. 64. [http://awsassets.wwf.org.za/downloads/concentrated\\_solar\\_power\\_report\\_final.pdf](http://awsassets.wwf.org.za/downloads/concentrated_solar_power_report_final.pdf).
- Sawin, J.L., Seyboth, K. & Sverrisson, F. 2016. *Renewables 2016: Global Status Report*.
- Skocypec, R.D., Boehm, R.F. & Chavez, J.M. 1989. Heat Transfer Modeling of the IEA/SSPS Volumetric Receiver. *Journal of Solar Energy Engineering*. 111(2):138–144.
- Tobergte, D.R. & Curtis, S. 2014. Global Review of Solar Tower Technology. *Journal of Chemical Information and Modeling*. 53(9):1689–1699.
- Vafai, K. 2005. *Handbook of Porous Media*. Second ed. Boca Raton: CRC Press.

- Wang, P., Vafai, K. & Liu, D.Y. 2016. Analysis of the volumetric phenomenon in porous beds subject to irradiation. *Numerical Heat Transfer, Part A: Applications*. 70(6):567–580.
- White, F.M. 1994. *Fluid Mechanics*. Third ed. New York: McGraw-Hill.
- Wu, Z., Caliot, C., Flamant, G. & Wang, Z. 2011a. Coupled radiation and flow modeling in ceramic foam volumetric solar air receivers. *Solar Energy*. 85(9):2374–2385.
- Wu, Z., Caliot, C., Flamant, G. & Wang, Z. 2011b. Numerical simulation of convective heat transfer between air flow and ceramic foams to optimise volumetric solar air receiver performances. *International Journal of Heat and Mass Transfer*. 54(7–8):1527–1537.
- Zhang, H.L., Baeyens, J., Degève, J. & Cacères, G. 2013. Concentrated solar power plants: Review and design methodology. *Renewable and Sustainable Energy Reviews*. 22:466–481.
- Zhao, Z., Peles, Y. & Jensen, M.K. 2013. Properties of plain weave metallic wire mesh screens. *International Journal of Heat and Mass Transfer*. 57(2):690–697.